Technische Universität München

Physik Department E20

Molecular Nanoscience and Chemical Physics of Interfaces

Combined STM and X-ray spectroscopy study of surface-confined biologically relevant molecules

Dissertation

Sybille Fischer

TECHNISCHE UNIVERSITÄT MÜNCHEN

Lehrstuhl E20 -

Molekulare Nanowissenschaften & Chemische Physik von Grenzflächen

Combined STM and X-ray spectroscopy study of surface-confined biologically relevant molecules

Sybille Fischer

Vollstädiger Abdruck der von der Fakultät für Physik der Technischen Universität München zur Erlangung des akademischen Grades eines Doktors der Naturwissenschaften (Dr. rer. nat.) genehmigten Dissertation.

Vorsitzender:	Univ.-Prof. Dr. Björn Garbrecht
Prüfer der Dissertation:	1. Univ.-Prof. Dr. Johannes Barth
	2. Univ.-Prof. Dr. Ulrich K. Heiz

Die Promotion wurde am 29.04.2013 bei der Technischen Universität München eingereicht und durch die Fakultät für Physik am 06.06.2013 angenommen.

Abstract

Surfaces modified with biologically relevant molecules play an important role in the development of medical applications, biomaterials and pharmaceutical synthesis. Consequently, the fundamental building blocks of life, amino acids, DNA/RNA bases and their derivatives are particularly interesting as adsorbates, while metal single crystals provide well-defined and atomically flat substrates.

In this thesis, the self-assembly, adsorption geometry and the chemical state of small biomolecules, namely cysteine, uracil, orotic acid and the bioactive species bisphenol A (BPA), were investigated as a function of temperature and surface coverage on coinage metals. The investigations were carried out under ultra-high vacuum conditions by means of scanning tunneling microscopy, near-edge absorption fine-structure and X-ray photoelectron spectroscopy. They revealed that the silver surface has only little influence on most of the functional groups, leading to distinct nanostructures which are predominantly stabilized by intermolecular hydrogen bonding. Cysteine, however, was shown to chemisorb onto the silver surface and the similarly strong interactions of the Cu(111) surface with uracil, orotic acid and BPA allowed them to be robustly attached to the surface. The stable tethering of the molecules furthermore enables a gradual deprotonation of the functional groups upon thermal treatment, resulting in new surface molecular conformations and concomitantly distinct self-assembly scenarios.

Kurzzusammenfassung

Die Funktionalisierung von Oberflächen mit biologisch relevanten Molekülen spielt eine tragende Rolle bei der Entwicklung von medizinischen Anwendungen, Biomaterialien und in der pharmazeutischen Synthesechemie. Als Bausteine des Lebens und der Natur sind hier insbesondere Aminosäuren und DNA/RNA Nukleobasen von Interesse. Metalleinkristalle mit ihren atomar glatten Oberflächen stellen geeignete Substrate dar, um sie in einer wohldefinierten Umgebung zu untersuchen.

Im Rahmen dieser Arbeit wurde die Selbstorganisation, Adsorptionsgeometrie und der chemische Zustand von Cysteine, Uracil, Orotsäure und Bisphenol A in Abhängigkeit von Temperatur und Oberflächenbedeckung untersucht. Die Studien dazu wurden unter Ultrahochvakuumbedingungen durchgeführ. Als Messmethoden kamen Rastertunnelmikroskopie, Röntgenphotoelektronenspektroskopie und Röntgen-Nahkanten-Absorptions-Spektroskopie zum Einsatz. Es konnte gezeigt werden, dass die Silberoberfläche lediglich geringen Einfluss auf die funktionellen Gruppen der Moleküle hat, die beobachteten individuellen Nanostrukturen sind folglich vor allem auf die Ausbildung zwischenmolekularer Wasserstoffbrückenbindungen zurückzuführen. Im Gegensatz dazu chemisorbiert Cysteine auf der Silberoberfläche. Die ähnlich starken Wechselwirkungen der Cu(111)-Oberfläche mit Uracil, Orotsäure und Bisphenol A ermöglichen eine solide Verankerung der Moleküle auf der Oberfläche und diese feste Anbindung der Moleküle an die Oberfläche ermöglicht die schrittweise Deprotonierung der funktionellen Gruppen durch Wärmebehandlung ermöglicht was zu der Ausbildung von neuen Oberflächenkonformationen und damit verbundenen individuellen Oberflächenstrukturen führt.

Contents

List of Figures

List of Tables

1 Introduction

"Imagination is more important than knowledge" - A. Einstein

In human history, the discovery of new materials, the enhancement of material properties as well as their processing were always closely linked to new technologies and evolution of society. Entire ages are named after certain materials, such as the stone-, bronze- and iron age. A very well known example, namely the invention of bronze, dates back to these times. Copper was used for jewelery and tools since at least 9000 BC [1], but as it is a rather soft metallic material, tools and weapons made from copper were easily deformable. The discovery of bronze, an alloy of copper and tin, introduced a much harder material suitable for these applications. Concomitantly, the necessity of organizing the production and trade lines for bronze resulted in significant changes in the society, allowing the creation of great prosperity for the first time in history [2]. Along with the enhancement of known materials came the modification of their surfaces, for example to prevent degradation by rust. The use of copper sheets for roofs and their copper oxide patina inhibiting further corrosion of the bulk is an early example for such altered surface properties, though presumably not deliberately generated. Nowadays, tailored interfaces strongly influence our lives and our society. The coating of metal surfaces with layers that change their properties is omnipresent. Some examples being the anticorrosive coatings of ships, car bodies and steel girders in construction works as well as non sticking coatings of frying pans. Recent computer technology would not be possible without integrated circuits consisting of silicon wafers precisely modified with several layers of insulating, semiconducting and conducting material. In most of these cases, the upper 10 to 100 atomic layers are modified [3], but in the past decades also the modification of surfaces and substrates on the molecular level is more frequently employed for daily use products. Well known to the public are self-cleaning surfaces based on the so-called "lotus effect", a phenomenon which is caused by the combination of a nanostructured surface with the hydrophobic properties of the waxes applied on the lotus leaf's surface. The example of the lotus leaf properties and their imitation for applications on synthetic materials is exemplary for the emerging field of biomimetics. Nature has been very successful in material engineering: biological systems exhibit reaction efficiencies and physical properties which are unequaled by materials developed by humans [4]. The application of biological properties to synthetic materials, especially surfaces, has contributed in recent years to the invention of several new materials and technologies, especially in the field of pharmacology. Surfaces, modified with smaller and larger biological molecules including amino acids, DNA bases, polypeptides, proteins, biomembranes, DNA strands or even DNA sequences offer an important interface between artificial materials and living beings [5]. The biofunctionalization of medical implant surfaces such as dental implants is a standard procedure nowadays [6, 7], it increases acceptance of synthetic materials by the human immune system and reduces the risk of inflammation. Apart from biocompatible materials and surfaces, further applications of biofunctionalized surfaces comprise biosensors and biochips for early disease detection [8–10], molecular electronics [11, 12], enantioselective catalysts [13] or DNA recognition protocols for anchoring and immobilization of macromolecules and nanoparticles onto surfaces [14, 15]. A main issue that all possible applications have in common is the question about the precise way of modifying the substrate's surface, i.e. the molecular arrangement, the conformation of the adsorbed molecule and their chemical state. A single broken bond, a different molecular conformation or a small substituent may cause the difference between a gene switched on or off, a protein being intact or denatured or general: a biologically active species that is working, or not.

In this thesis, the self-assembly and chemical state of small biologically relevant molecules adsorbed on coinage metal surfaces was investigated. Small molecules such as amino acids, nucleobases and their derivatives are the important building blocks of proteins and DNA. As such, the precise understanding of their adsorption properties is crucial when proceeding to more complex systems. Similar to scenarios in nature, where structures such as membranes and cells are formed by self-assembly protocols, organic molecules self-assemble on many surfaces, forming strong covalent and non-covalent bonds to the surface and between neighboring molecules. Especially hydrogen bonding enables the formation of large and stable organized layers of molecules on the surface which are often almost free of defects.

Among several other techniques, scanning probe microscopy techniques became standard tools for the investigation of surfaces modified with biological adsorbates [16, 17]. Invented in the early 1980's by Gerd Binnig and Heinrich Rohrer and rewarded with the Nobel price in 1986, the scanning tunneling microscope (STM) allowed to obtain an image of a surface on the atomic level [18–20]. STM is based on the quantum mechanical tunneling effect, that is, the probability of electrons to tunnel through a small nonconductive gap between two conducting materials. The tunneling current, which depends exponentially on the distance (in the range of nm) between the two conductors usually ranges between 50 pA to some nA. Keeping this current constant, one can scan a sample's surface line-by-line and by recording the movement of the tip obtain atomic insight into the surface. At the time of the invention of STM, common techniques employed in surface science were predominantly based on the principle of diffraction, i.e. the description of the surface was based on information in the reciprocal space. In contrast, STM enables the illustration of the surface topography in real space [21], which makes it a perfectly suitable method for the local investigation of adsorbed biomolecules on surfaces and it is not limited in the study of systems with long range order. The high resolution of STM (one of the breakthrough data obtained by an STM was an atomically resolved image of the Si(7$\times$7) reconstruction [18]) allows to image single small molecules or even submolecular features. By monitoring with STM the same area as a function of time, molecular dynamics can be investigated and even movies of molecular movements have been made (e.g. [22, 23]). But even though STM allows a precise study of a surface's topography, the molecular arrangement and may even give hints towards the orientation of molecules on the surface, it does not readily provide chemically specific information about the adsorbates and the interface. This information can be readily obtained by X-ray photoelectron spectroscopy (XPS). In an XPS experiment, a photon knocks out an electron from the core or valence state of an atom (the so-called photoelectron). The energy of the level of origin can be calculated from the photoelectron's kinetic energy and is unique for each element and its specific chemical state. As the intensity of detected photoelectrons is dependent on the element count, it even allows the determination of the elemental composition of a surface adsorbate [24]. Another X-ray spectroscopy technique, which is additionally sensitive to the symmetry of the molecule's final state orbital with respect to the orientation of the incoming photon beam is the so-called near-edge X-ray absorption fine-structure (NEXAFS) spectroscopy. Due to its sensitivity to the photon incidence angle, angle-resolved measurements are a very suitable tool to obtain information on the conformation of a adsorbed molecule and its orientation with respect to the surface. Even though XPS and NEXAFS spectroscopy are, in contrast to STM, space averaging techniques, they provide detailed insight into the chemical state and conformation of adsorbed biomolecules on surfaces and support the interpretation of STM data as well as the understanding of the investigated systems significantly.

The present thesis focuses on the investigation of the two-dimensional self-assembly of four different biologically relevant molecules and their chemical behavior as a function of temperature and surface coverage. Specifically, the adsorption of the amino acid cysteine (figure 1.1a) in both enantiomeric forms was investigated on the Ag(111) surface, the RNA base uracil, its derivative orotic acid and the biologically relevant bisphenol A (figure 1.1b-c) molecule were studied on both Ag(111) and Cu(111). Metal single crystal surfaces were chosen for these investigations as their well-defined conducting surfaces

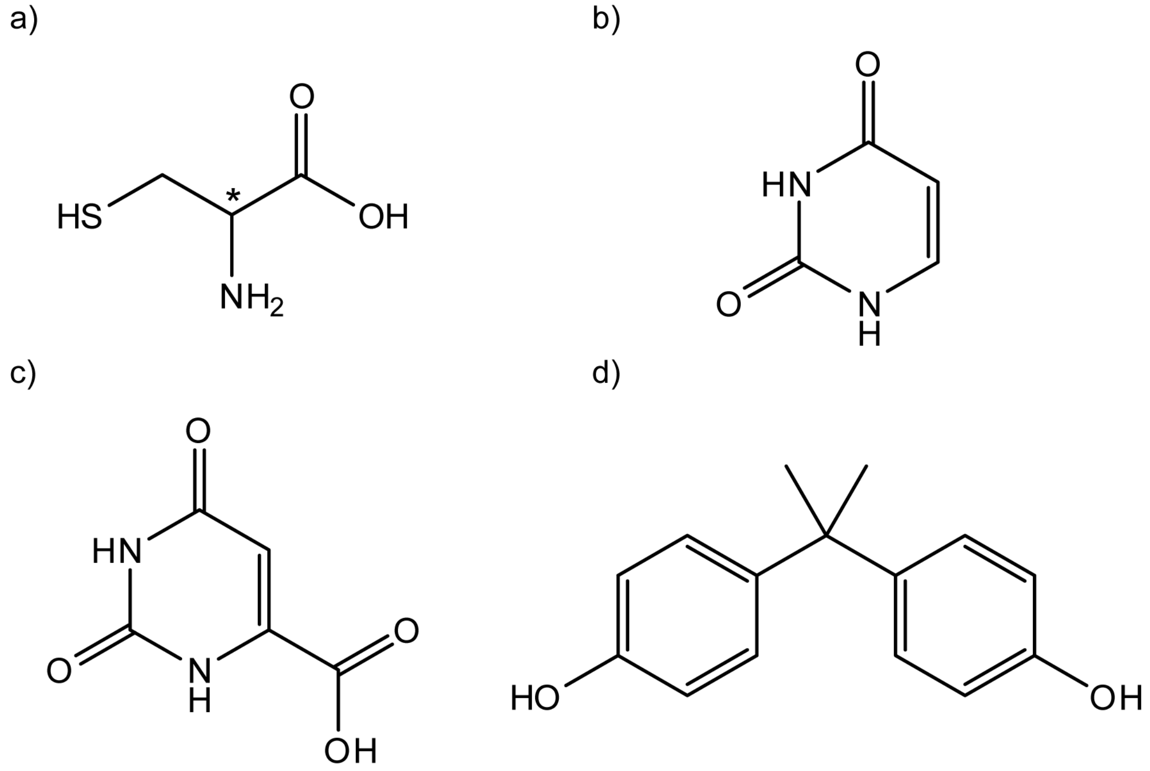

Figure 1.1: Chemical structures of a) cysteine (the star marking the chiral center), b) uracil, c) orotic acid and d) bisphenol A.

with extended, atomically flat terraces perfectly meet the requirements of STM. While silver is weakly interacting with most organic molecules, the copper substrate is more reactive, giving the opportunity to study the influence of the substrate on self-assembly and chemical behavior.

All systems investigated along with the present thesis were studied by means of STM, XPS and NEXAFS. These techniques, which were briefly described above, are explained in finer detail in the following chapter 2. The chapter also describes the detailed experimental setup and the sample preparation procedures.

Chapter 3 comprises four sections, each presenting the results of the investigated molecules. The self-assembly and chemical state as a function of temperature of both enantiomers of the amino acid cysteine (figure 1.1a) adsorbed on the Ag(111) surface are addressed in section 3.1. The naturally occurring L-enantiomer of this molecule represents the only proteinogenic amino acid with a thiol side group, which allows to anchor the molecule stably on noble metal surfaces. The strong binding to the surface allows temperature-induced deprotonation of the ammonium group which results in a significant change in molecular conformation, leading to a completely new arrangement of the molecules where the chirality of the molecule is reflected by the self-assembled structures on the surface. Section 3.2 summarizes the self-assembly and temperature-induced chemical transformations of uracil (figure 1.1b), the nucleobase differentiating RNA from DNA, on both Ag(111) and Cu(111). The strong interaction of the molecule with the copper substrate enables the gradual deprotonation of the functional nitrogen units resulting in different molecular arrangements. This opposes the scenario on the Ag(111) surface, where the self-assembly of the intact uracil molecules is rather driven by intermolecular interactions than by interactions with the silver substrate. A very important derivative of uracil is orotic acid (figure 1.1c), a basic molecule in the natural synthesis of nucleobases, which differs from uracil in a single carboxy substituent. While the chemical behavior of orotic acid is generally similar to uracil on both substrates, the two-dimensional crystallization differs particularly on the copper substrate, where only a single periodic structure with a lifetime of two to three hours could be observed. The results from the study of orotic acid on Ag(111) and Cu(111) are summarized in section 3.3. Finally, the adsorption behavior and thermally stepwise deprotonation of bisphenol A (BPA, figure 1.1d) is presented in section 3.5. Even though BPA is not part of the human biochemistry, is has the ability to trigger or suppress chemical changes of DNA nucleobases [25] and therefore is investigated along with other small biomolecules. Similar to the aforementioned molecules, the interaction of BPA with the silver substrate is much weaker than with the copper substrate. Different polymorph structures comprising intact molecules were found on Ag(111), while on Cu(111), the molecule is anchored quite strongly on the surface and thermally induced stepwise deprotonation of the hydroxy groups leads to different stable molecular arrangements as a function of temperature.

Chapter 4 gives concluding remarks and an outlook towards possible future applications.

2 Experimental Methods: Theory and Setup

The following chapter describes the techniques and instrumentation employed for the experiments performed in context of the present thesis. The first section gives a brief overview on the physical principles of the tunneling effect followed by a general description of scanning tunneling microscopy (STM), the details of the variable-temperature STM and the ultrahigh vacuum chamber setup as well as the distinct preparation procedures. All presented STM experiments were supported by additional X-ray spectroscopy measurements, which were performed at the *HE-SGM* beamline at *BESSY II.* Therefore, a brief outline of the theoretical background of X-ray photoelectron spectroscopy (XPS) and near-edge X-ray absorption fine-structure (NEXAFS) is presented together with the succinct description of the local setup.

2.1 The scanning tunneling microscope (STM)

2.1.1 The tunneling barrier

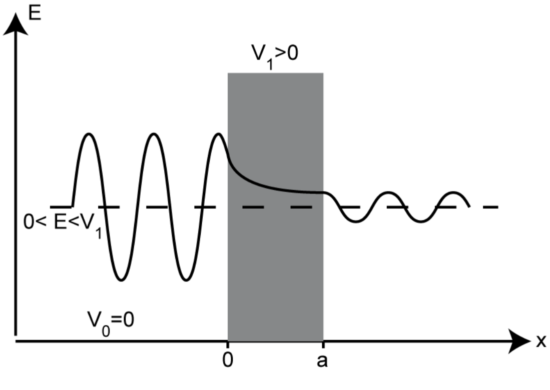

Figure 2.1: Sketch of a electron wave function with the energy E tunneling through a potential barrier of $V_1 > E$ [26].

The tunneling effect is the physical phenomenon on which scanning tunneling microscopy is based. Therefore, the quantum mechanical theory [26, 27] for the one dimensional, time independent approximation is described below. According to classical mechanics, a particle whose overall energy does not exceed the energy of a barrier is unable to penetrate it. In contrast, the quantum mechanical approach finds a finite probability for an electron to overcome the potential barrier even if its energy is lower than the barrier potential (Figure 2.1). The subsequent description will focus on electrons in one dimension. In every region with a potential $V \geqq 0$, an electron with the wave function ψ must fulfill the Schrödinger equation

$$\frac{d^2\psi}{dx^2} = \frac{2m}{\hbar}(V_x - E)\psi \tag{2.1}$$

with m being the mass of the electron, E the energy of the electron and $\hbar$ the reduced Planck constant. For $x \leq 0$ and $x \geq a$, where $V = V_0 = 0$, the solution of 2.1 for ψ is given by:

$$\psi(x) = \psi(0)e^{\pm ikx} \text{ with } k = \frac{\sqrt{E2m}}{\hbar} \tag{2.2}$$

describing an electron which can propagate freely in positive and negative directions of x and has a constant momentum $p = k\hbar$. Considering now the region inside the potential barrier, where $V = V_1 > E$, the solution of the Schrödinger equation is

$$\psi(x) = \psi(0)e^{\pm\kappa x} \text{ with } \kappa = \frac{\sqrt{2m(V_1 - E)}}{\hbar} \tag{2.3}$$

This equation describes the electron's wave function decaying exponentially with x inside the potential barrier. Additionally it shows, that the electron indeed is able to penetrate the potential barrier. The probability of the electron to be at any point inside the barrier is given by:

$$P = |\psi(x)|^2 = |\psi(0)|^2 e^{2\kappa x} \tag{2.4}$$

where $0 \leq x \leq a$.

Even though this equation shows a probability of tunneling through a potential barrier, there is no net current between two electrodes separated by an insulator, as the probability of tunneling from 0 to a is the same as for tunneling from a to 0, for electrons with the same potential. Proceeding towards the more realistic metal-vacuum-metal system, the potential of the barrier V_1 can be replaced by the vacuum level of the metal, therefore, $E_F = -\phi$. The work functions of both, sample and tip, are assumed to be the same. Applying a voltage V_b between them leads to a net tunneling current. Hence, an electron of an occupied sample state ψ_n whose energy lies in between E_F and $E_F - eV_b$ has a possibility to tunnel into the tip (Figure 2.2). Assuming that the sample state n of interest is lying close to the Fermi level $E_F = -\phi \sim E_n$ the probability of an electron from this

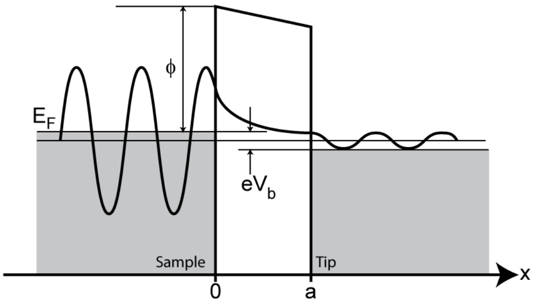

Figure 2.2: 1D sketch of the system metal-vacuum-metal showing the tunneling process from the sample into the tip at finite voltage [27].

sample state to be present at the surface of the tip is analogous to

$$|\psi_n(0)|^2 \, e^{-2\kappa a} \text{ with } \kappa = \frac{\sqrt{2m\phi}}{\hbar} \tag{2.5}$$

As a finite number of sample states exists, summing up over all sample states between E_F and $E_F - eV_b$ leads to the formulation for the tunneling current

$$I_t \propto \sum_{E_F - eV_b}^{E_F} |\psi_n(x)|^2 \tag{2.6}$$

Assuming a constant local density of states (LDOS) for the tip as well as low voltages and T=0, equation 2.6 can be written as

$$I_t \propto V\rho(0, E_F)e^{-2\kappa a} = V\rho(0, E_F)e^{\frac{-2a\sqrt{2m\phi}}{\hbar}} \tag{2.7}$$

where $\rho(x, E_F)$ is the LDOS. From this correlation it is obvious, that the tunneling current is directly proportional to voltage and the LDOS, but it is exponentially dependent on the distance between sample and tip. Retracting the tip from the sample by approximately one Å leads to an order of magnitude decrease in the tunneling current. Thus, I_t is very sensitive to the tip-sample distance or rather the change of the distance.

The formalism of Bardeen [28] takes into account, that tip and sample have different wave functions and that there is a matrix element, which describes the overlap of the two wave functions at a separation surface. Evaluating the matrix element by employing the ansatz of Tersoff and Haman [29] leads to a correlation in which the main tip state involved in the tunneling process is an *s*-state and the two wave functions do not influence each other. For small bias voltages V_b, the tunneling current I_t is directly proportional to the LDOS of the sample.

$$I \propto V_b e^{-2kR} \rho_{tip}(E_F) \rho_{sample}(E_F, r_0) \text{ with } k = \frac{\sqrt{2m\phi_t}}{\hbar} \tag{2.8}$$

where R is the tip radius, ϕ_t the barrier height and r_0 the position of the center of the tip's curvature. This last equation implies, that the information shown in a STM image is not only dependent on the LDOS of the sample and the topography, but also from the LDOS and the shape of the tip.

2.1.2 The STM

The functionality of the scanning tunneling microscope is based on the tunneling effect as it is described in the previous subsection. As the tunneling effect depends exponentially on the distance between sample and tip, it can be used to determine the topography of a surface. Strictly speaking, an STM image does not solely depict the geometry of a surface, but a convolution of geometry and electronic effects, thus the LDOS. By scanning a surface line-by-line and recording the tunneling current with respect to the distance between tip and sample, a 3D image of the surface can be obtained. According to equation 2.8, the radius of the tip's apex plays a considerable role in the resolution of the STM and for optimum resolution atomically sharp tips are used. The fabrication of very sharp tungsten tips and their *in-situ* tuning is explained in subsection 2.1.3. The tip is moved by a piezo tube scanner (Figure 2.3). A thin tube made of piezo ceramics is coated with metal which acts as an electrode for both the inner and the outer part. The outer part is divided into four equally shaped and sized electrodes separated by thin stripes which are uncoated. Applying a voltage between the inner and all outer electrodes leads to a contraction or extension of the scanner in z-direction. The lateral movement is achieved by applying bias between two opposed outer electrodes, leading to a bending of the tube.

The STM can be operated in two different modes: The "constant current mode" (Figure 2.4a) is the one used in most cases. Here, the tunneling current is kept constant during scanning which is achieved by monitoring the current and frequently readjusting the height of the tip. The z-displacement of the tip plotted as a function of x and y generates the 3D STM image. The scanning speed is dependent on the frequency and the number of the feedback measurements. The other mode which is used less frequently is the "constant height mode" (Figure 2.4b). The absolute height of the tip with respect to the surface is kept constant and the tunneling current is used as an indicator for topography and density of states. The advantage of this scanning mode is that there is no feeback loop required which allows high scanning speeds and eliminates related artifacts, but the risk of crashing the tip into the sample makes it suitable only for very even surfaces.

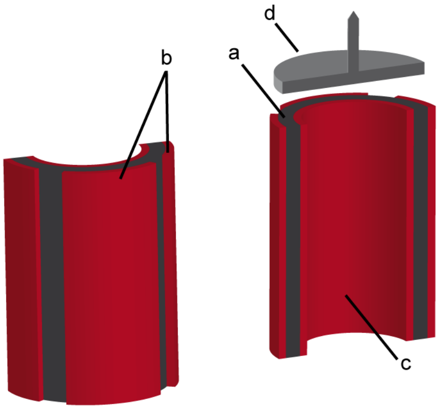

Figure 2.3: Design of a piezoelectric tube scanner with d) mounted tip on the top used for scanning tunneling microscopy: a) A piezo ceramics tube with b) the outer electrodes and c) the inner electrode.

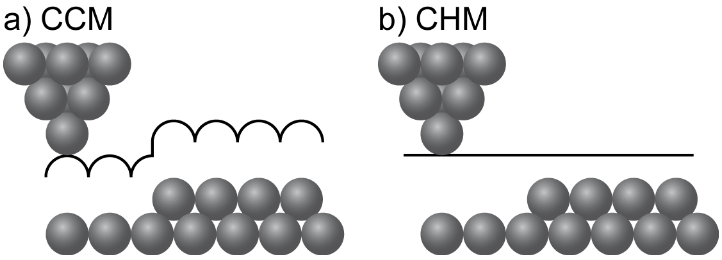

Figure 2.4: Visualization of the two STM operation modes: a) The constant current mode (CCM) and b) the constant height mode (CHM).

2.1.3 Experimental setup

All STM images shown in the present thesis were recored in a custom designed (by Alexander Weber-Bargioni) ultra-high vacuum chamber equipped with a commercially available variable-temperature (VT) STM (*"Aarhus 150" SPECS Surface Nano Analysis GmbH* [30, 31]) . The setup is schematically shown in figure 2.5. The UHV system consists of two-chambers. The preparation chamber and the STM chamber can be separated by a vertical gate valve. A transfer system consisting of a long lateral manipulator and three shorter ones normal to it is employed to transfer samples between the two chambers and the different sample stages. The shorter manipulators are located in the STM chamber, the preparation chamber and the load-lock. The latter is used to transfer samples from air into the UHV chamber without breaking the vacuum. The manipulators employ a bayonet lock on the front part, which allows to grab the sample. They can be moved using magnetic coupling with a tube-like part on the outer side of the manipulator. Both chambers are equipped with Ar^+ -sputter guns (*Eurovac*). Additionally the preparation chamber contains an organic molecular beam epitaxy (OMBE) type *"Dodecon OMBE-4C-250-001"* and a home build metal evaporator. Organic molecules can be filled into quartz crucibles with a diameter of 5 mm and sublimed into vacuum by resistive heating. The distance to the sample is $\sim$ 10-15 cm. In the present case, the OMBE can hold four crucibles with different molecules at the same time. The temperature is measured at the crucible holder. The parking stage stores up to 4 samples and also comprises a heatable preparation stage. Samples on the stage are heated by electron beam heating with acceleration voltages of up to 800 V to temperatures of 870 K and higher. With resistive heating, samples can be heated to temperatures up to 770 K, allowing to anneal electron beam sensitive surfaces.

The ultra-high vacuum chamber is pumped with a system of turbomolecular pumps connected in series. A membrane pump as the first pumping stage of the system is reducing the pressure to approximately 3-5 mbar. A small turbo molecular pump decreases the pressure further to $\sim 10^{-5}$ mbar. The main pump again is a turbo molecular pump which is able to pump the chambers to a base pressure ranging between 2×10^{-9} and 2×10^{-10} mbar after bake-out. The three-stage pumping system is supported by an ion getter pump located on the bottom of the STM chamber.

The sample-holder (See figure 2.6) is build from two molybdenum plates which are connected with four small molybdenum screws and the hat-shaped single crystal in between. K-type thermocouple wires are connected to the back side of the crystal and are fed through a ceramic piece to the back side of the sample plate, where they can be connected to a thermocouple counterpart on the preparation stage for accurate temperature reading on the sample. The upper plate also includes the coupling part for the bayonet

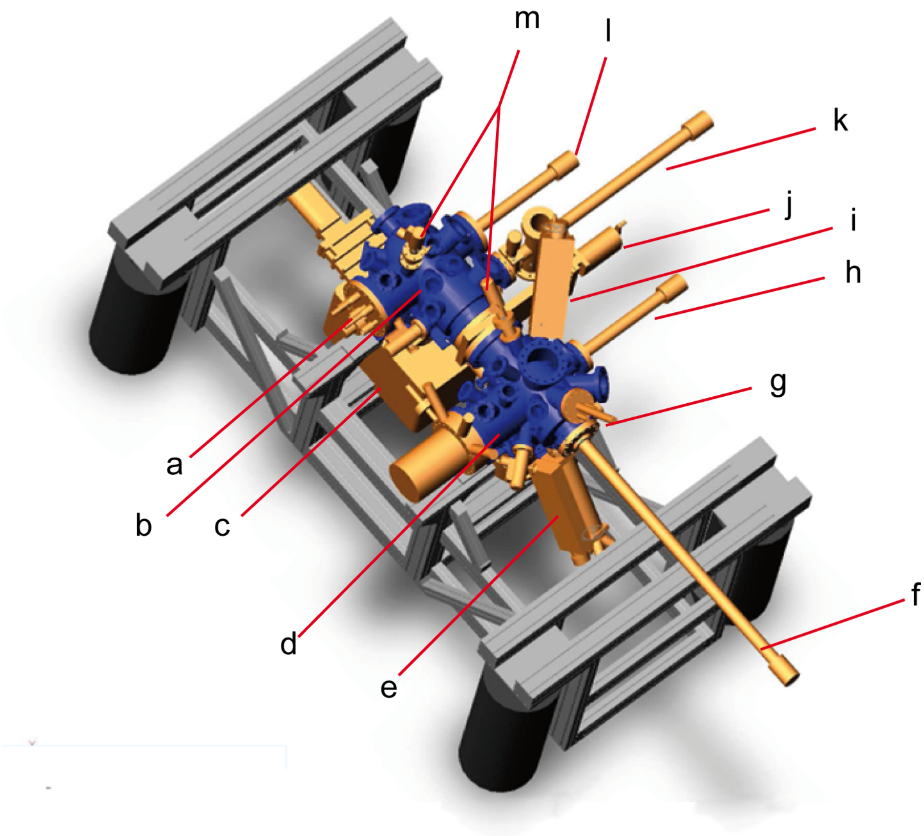

Figure 2.5: Setup of the UHV chamber containing a) the variable-temperature Aarhus STM. The system consists of two chambers: b) STM and d) preparation chamber separable by j) a gate valve. The transfer system includes f) a lateral manipulator and h+l) one manipulator in each of the two chambers. Additionally, there is k) a load-lock, g) a preparation stage with sample parking, e) an OMBE, i) a metal evaporator and m) Ar^+ sputter guns in both chambers. c) The ion getter pump is part of the pumping system.

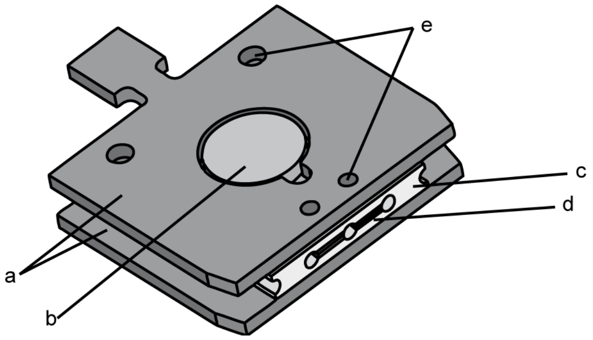

Figure 2.6: Drawing of the sandwich-style sample holder: a) molybdenum plates, b) hat-shaped single-crystal (polished side visible), c) ceramic piece, d) thermocouple wires and e) molybdenum screws.

lock.

The VT-STM can be operated in a temperature range of approximately 130-470 K (setup shown in figure 2.7). The STM tube scanner described in 2.1.2 is located on top of an inchworm motor which is used to coarsely approach the tip towards the sample surface at tunneling distance. This inchworm consists of a SiC rod which is moved by a piezo motor, moving the rod with high precision in a range of several millimeter. A Zener diode is used for counterheating the STM scanner as this kind of scanner is not designed to operate below room temperature.The scanner is mounted inside a base plate and is fixed with three small ceramic balls which electrically and thermally isolate the scanner. The sample itself can be placed on top of this base plate and is held in position by small copper clamps. The base plate with the scanner is mounted in a aluminium block of approximately 200mm × 150mm × 100mm which acts as thermal reservoir. The "finger" (Figure 2.7l) that is used to lock the block can be cooled with a cooling agent, e.g. liquid nitrogen, and, while locked, also cools the aluminium block. For STM meausrements at elevated temperatures, the aluminium block can be resistively heated to $\sim$ 470 K by an additional Zener diode. The whole STM system is suspended via springs when unlocked in order for isolation from external vibrations and electrically isolated from the rest of the UHV chamber.

Tungsten tips were used for all experiments performed in the described STM. The tips were premounted on a copper tip holder plate and sharpened by electrochemical etching with saturated NaOH solution and 3.5-5 V DC. The tungsten wire is placed in the middle of a gold-ring (Figure 2.8). By dipping the wire and the ring into the NaOH solution, a lamella was produced inside the ring which allowed precise etching in the plane of the

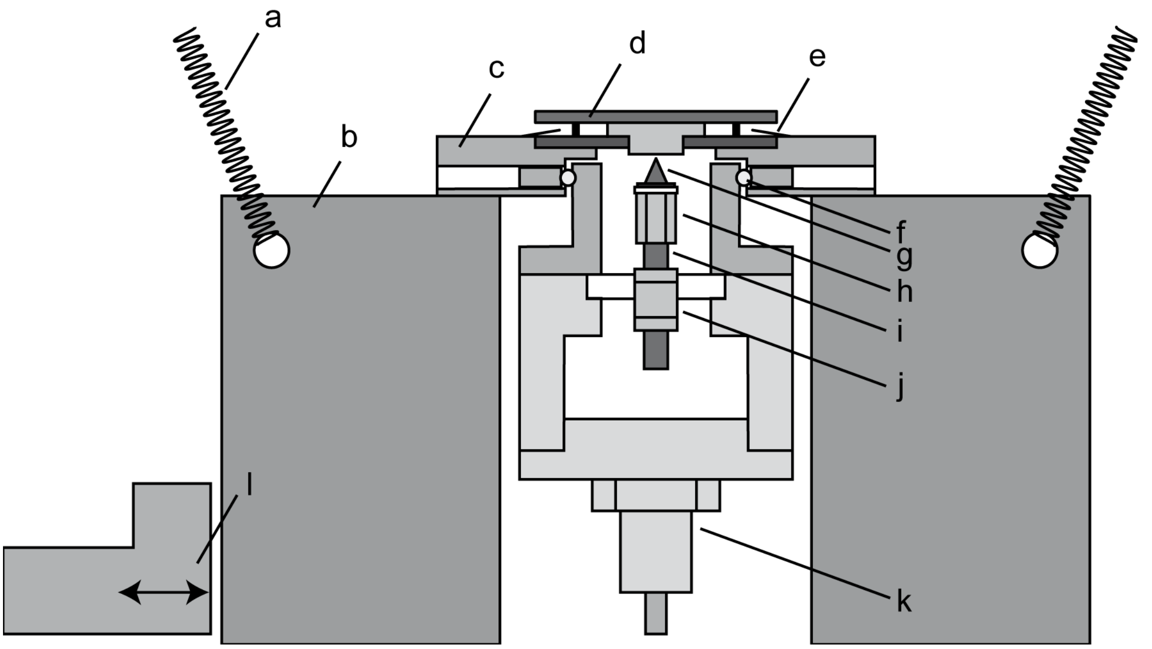

Figure 2.7: Cross-section of the scanning tunneling microscope of the type “Aarhus 150”. a) Suspension springs, b) aluminium block, c) base plate, d) sample holder, e) copper clamps, f) ceramic balls, g) tip, h) STM piezo motor, i) SiC rod, j) inchworm piezo motor and k) Zener diode, l) cooling “finger” [30].

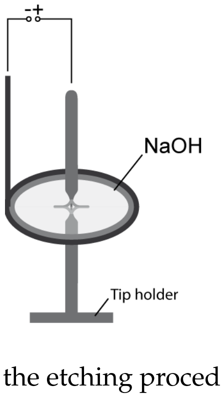

Figure 2.8: Sketch of the setup for the etching procedure of tungsten tips for the STM.

gold ring. The relevant etching process at the anode follows the reaction scheme

$$\mathrm{W(s)} + 8\ OH^- \longrightarrow WO_4^{2-} + 4\ H_2\mathrm{O} + 6\,\mathrm{e}^-$$

and is completed in $\sim$ 20-30 min for a wire of 0.25 mm thickness. Tungsten is inert against extensive oxidation at room temperature and in air due to a passivation by a thin native oxide layer. Mounted on top of the STM scanner, the tip was sputtered *in-situ* in order to remove the tungsten oxide layer from the surface. In addition, there are methods of fine tuning the tip during scanning. Applying a voltage of up to 10 V for a short time allows removal of adsorbed contaminants from the tip. By dipping the tip carefully into the substrate, there is a chance of some metal atoms from the substrate sticking to the tip, creating an extremely sharp tip.

2.1.4 Sample preparation procedures

Clean metal single crystals with extended atomically flat terraces are crucial for the investigation of self-assembled systems by means of STM and X-ray spectroscopies. The silver and copper single crystals used in STM experiments are hat-shaped with 6 mm diameter of the polished side, 8 mm diameter of the back side and 2 mm total height. They are specified with a roughness of less than 30 nm and an orientation mismatch better than 0.1°. All crystals were prepared by cycles of sputtering and annealing. The Ar^+-sputter gun ionizes argon and accelerates the ions with high voltage. Typical parameters here are 1 kV and 15 mA emission current. By bombarding the single crystal surface with Ar^+, the surface gets exempt from adsorbates and surface impurities and the upper atomic layers of the sample's surface are partly removed, leading to a roughened surfaces. Annealing the Cu(111) and Ag(111) sample by means of electron beam heating for 10 min to 770 K and 630 K, respectively, increases the mobility of the surface atoms which rearrange themselves into large terraces. The cycles were repeated until extended atomically flat and clean areas were detected throughout the crystal by STM. Cysteine, uracil, orotic acid and bisphenol A were dosed onto the clean surface using the OMBE described earlier. The vacuum sublimation temperatures are liste in table 2.1.

The sample temperature during deposition was 300 K, except for the low temperature preparation of bisphenol A, where the molecules were dosed onto a sample which was previously cooled on the STM stage. STM measurements were performed at 130 K to 380 K. To achieve the latter, the STM block (described in subsection 2.1.3) was pre-cooled with liquid nitrogen to a minimal temperatures of 130 K upward, higher temperatures can be controlle by the Zener diodes. For the analysis of the STM measurements, images were processe with the WSxM software [32].

Molecule	Vac. Subl. T / K	Manufacturer	Purity
L-Cysteine	413-433	Fluka	$>$99.5%
D-Cysteine	413-433	Sigma Aldrich	$\geq$99%
Uracil	420-470	Sigma Aldrich	$\geq$99%
Orotic Acid	480-500	Sigma Aldrich	$\geq$99%
Bisphenol A	400	Sigma Aldrich	$\geq$98%

Table 2.1: Vacuum sublimation temperatures, manufacturer and purity of the investigated molecules.

2.2 Synchrotron X-ray spectroscopy

STM measurements provide information concerning the topography of the surface, the self-assembly, possible phase transformations and can even hint towards the molecular orientation of adsorbates. However it's major drawback is the lack of chemical specificity. X-ray photoelectron spectroscopy (XPS) can fill this gap in our understanding of molecular overlayers on surfaces by providing information about chemical behavior, state and environment of surface adsorbates and further enable us to monitor chemical changes during phase transformations. Additionally, with angle resolved near-edge X-ray absorption fine-structure spectroscopy (NEXAFS) the orientation of molecules and submolecular groups with respect to the surface can be determined within 10°. Both techniques were carried out at the synchrotron facility of *BESSY II* in Berlin.

Synchrotron radiation is emitted by radially accelerating charged particles, e.g. electrons (for synchrotron setup, see figure 2.9). The frequencies of the so produced radiation range over the entire electromagnetic spectrum and the radation has a distinct horizontal polarization. The horizontal polarization is a result of the - according to the construction - horizontal orientation of the large storage ring. The particular properties of the synchrotron radiation allow X-ray spectroscopy measurements with high intensities which is unmatched by smaller laboratory X-ray sources and, due to the possibility of the selection of a single wavelength via monochromator, a very high resolution.

All spectroscopy data presented in this work were recorded at the *HE-SGM* dipole beamline of *BESSY II.* This beamline provides horizontally polarized light with a grade of polarization of 90% and a photon energy range of approximately 200 eV - 800 eV. A more detailed description of the system is provided in subsection 2.2.3.

2.2.1 X-ray photoelectron spectroscopy (XPS)

X-ray photoelectron spectroscopy (XPS) is a powerful tool for chemical element analysis. The method is based on probing the element's characteristic core level binding energies. The basic principle of XPS is the excitation of inner shell electrons by X-ray radiation (for

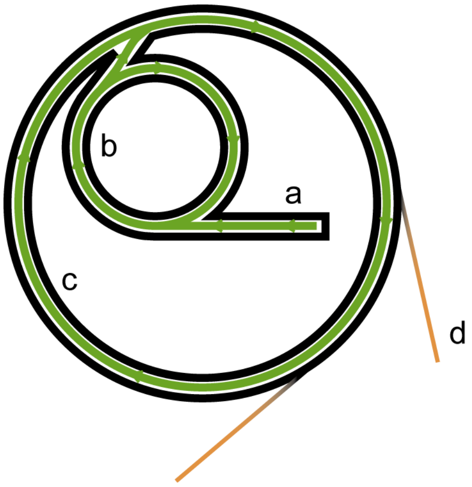

Figure 2.9: Common setup of a synchrotron storage ring, including a) the either linear accelerator or microtron injector, accelerating electrons to $\sim$ 100 MeV, b) the accelerator, which accelerates the electrons to $\sim$ GeV before they are injected into c) the storage ring and d) the seperate beamlines [26, 33].

soft X-rays usually in a regime of 200-2000 eV) and the measurement of the photoelectron kinetic energy. The element's binding energy is given by:

$$E_B = h\nu - E_{kin} - \phi_s$$

where ϕ_s is the element's workfunction, $h\nu$ is the excitation energy and E_{kin} is the measured kinetic energy of the photoelectron. As the binding energy is usually normalized to the fermi edge, the workfunction must be taken into account (see figure 2.10). Even though the core electrons play a minor role in the formation of chemical bonds, their binding energy varies at a small scale due to the redistribution of the residual electrons, when a bond is created. For this reason, XPS is not only suitable for elemental analysis but also sensitive to an atom's local chemical environment, e.g. the chemical state of an investigated molecule.

The photon beam is able to penetrate the sample in a range up to microns, however the short mean free path of the photoelectrons result in an electron escape depth from the surface of only few nm making XPS a quite surface sensitive method [35]. The surface sensitivity can be additionally increased by altering the photon energy (Figure 2.11) or decreasing the angle between the surface and the analyzer (grazing emission vs. normal emission).

When recording an XPS spectrum, the system is exposed to photons of a specific energy. The detected intensity of photoelectrons is then plotted in dependence of their bind-

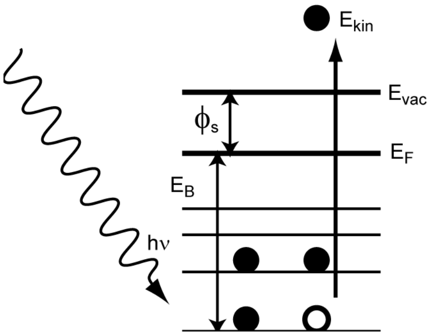

Figure 2.10: Visualization of the excitation of core electrons into continuum states by X-ray radiation with a photon energy of h˚. The kinetic energy of the photoelectrons is detected with an electron analyzer.

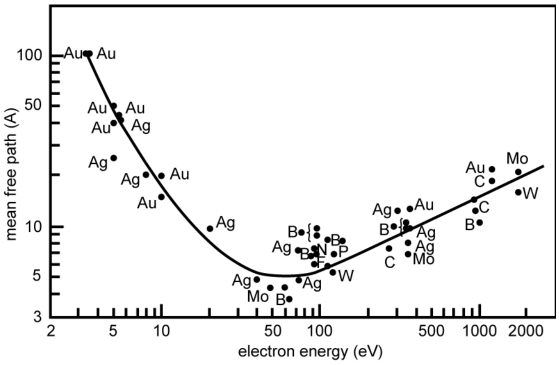

Figure 2.11: Graph showing the electron mean free path in a dense packed solid with respect to the electron energy [34].

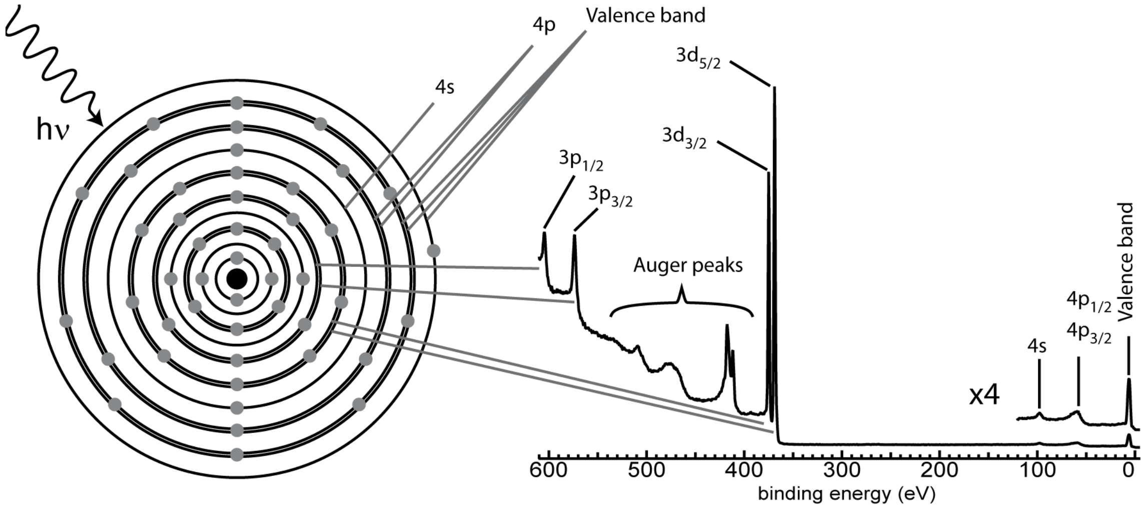

Figure 2.12: Right: Typical XPS spectrum of a bare Ag(111) surface. The peaks are assigned to their energy level of origin. Left: Model of a silver atom with the energy levels drawn as black circles and electrons as grey dots.

ing energy. The binding energies of the observed elements can be seen as peaks in the spectrum. The sensitivity of XPS to different chemical environments, results from considerable shifts in the binding energy allowing to discriminate between elemental signals of chemically different species. The differences in binding energy for the same element can reach 10 eV. In this respect, the intensities for differently shifted core level binding energies reflect the ratio between the chemically different species of the corresponding element. Identifying the ratio between different elements is more complicated as the ionisation cross sections must be taken into account. A negative partial charge of an atom is screening the nuclear charge, leading to lower binding energies of the core electrons. This leads to the rule of thumb, that the higher the negative partial charge on an atom, the lower it's binding energy and the higher the positive partial charge, the higher the binding energy of this atom [35]. Additionally, for excitations from p, d, and f-orbitals, spin-orbit coupling needs to be taken into account (see figure 2.12). The coupling leads to a splitting of the energy levels ending up with a doublet signal in the XPS spectrum [36]. Beside the emission of first-order photoelectrons, Auger electrons must be taken into account. After the creation of a core hole (α), the core hole can refilled by another electron from an orbital with higher energy (β). The energy gained by this process is tranferred to another electron (Auger electron) with a higher binding energy (γ) which is excited to the continuum. As Auger electrons from the same process arise with the exactly the same kinetic energy, $E_{kin,A} = E_\alpha - E_\beta - E_\gamma - \phi_S$, Auger peaks can be distinguished in an XPS spectrum from photoelectron signals, as their peak position shifts with the excitation energy.

2.2.2 Near-edge X-ray absorption fine-structure (NEXAFS)

NEXAFS is a powerful tool to gain information about the orientation of molecules and molecular subgroups with respect to the surface. This technique probes the unoccupied molecular orbitals by means of absorption of photons with an energy $h\nu$ close to the absorption edge of the system and detects the associated number of emitted photons. For simplicity, the following section refers to absorption close to the K-edge. Exposure of the investigated system to X-ray radiation with a distinct frequency excites electrons of the K-shell (thus the 1s orbital) into unoccupied molecular orbitals (e.g. the π^* molecular orbital) wherever the energy difference of the orbitals equals the photon energy ($h\nu = E_{\pi^*} - E_{1s}$) and does not exceed the ionization potential ($IP = E_{vac} - E_{1s}$). The absorption intensities are measure by the quantity of emitted seconary Auger electrons (Figure 2.13). In case of the photon energy exceeding the ionization potential, electrons can also be excited into a virtual σ^* orbital with the shape of a σ orbital. For a neutral molecule, usually both, the σ^* and the π^* orbitals are situated above the vacuum level, but the

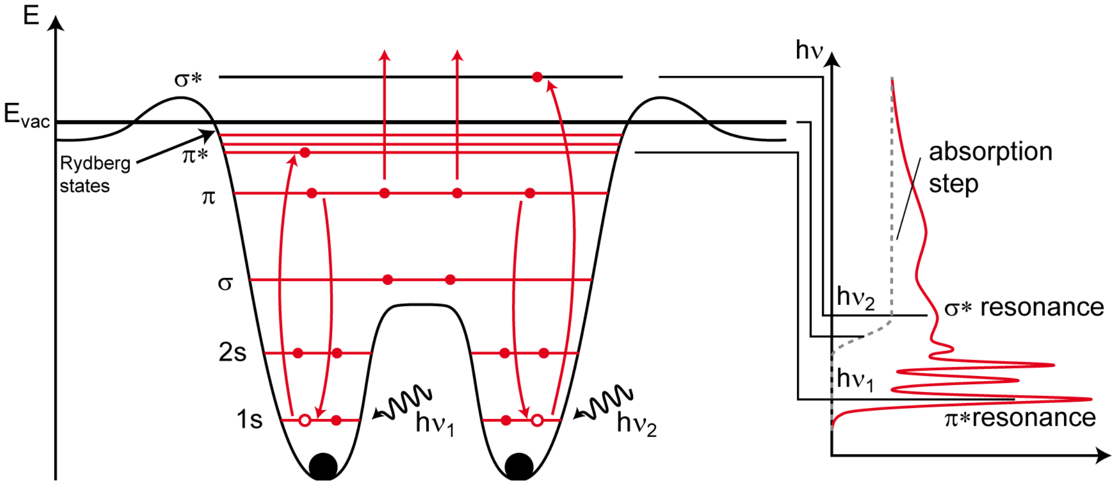

Figure 2.13: Schematic model of the Auger electron emission for a diatomic molecule. The excitation of 1s electrons by two different photon energies hν_1 and hν_2 into a π^* and σ^* orbital respectively leads to the corresponding signals in the NEXAFS spectrum shown on the right side. The absorption edge is drafted by a dotted line in the spectrum [cf. 37].

latter is pulled below due to electron-hole Coulomb interactions [37].

By sweeping the X-ray energy close to the absorption K-ege in a range of approximately -10 eV to +20-50 eV and measuring the associated number of emitted Auger electrons, a NEXAFS spectrum is recorded. The number of emitted Auger electrons is directly proportional on the number of absorbed photons, i.e. on the probability of the 1s electron to be excited into the corresponding unoccupied orbital. A retarding potential in front of the electron detector (channeltron) suppresses electrons with low kinetic energies and thus results in a better signal-to-noise ratio as contributions from inelastic electron scattering, emitted photoelectrons and multi-electron processes are minimized. This detection method is called partial electron yield (PEY).

Exploiting the fact, that the direction of polarization is well known for synchrotron radiation, NEXAFS reveals information about the orientation of molecules with respect to the surface plane. The relation between the absorption cross section σ_x, the initial state ψ_i and final state ψ_f can be described in an equation which is based on the quantum mechanical description of the excitation process for a single electron in the dipole approximation (“Fermi’s Golden Rule”):

$$\sigma_x \propto \left| \langle \psi_f \,|\, \vec{e} \cdot \vec{p} \,|\, \psi_i \rangle \right|^2 \rho_f(E)$$

where $\vec{e}$ is the unit electric field vector, $\vec{p}$ the dipole transition operator, and $\rho_f(E)$

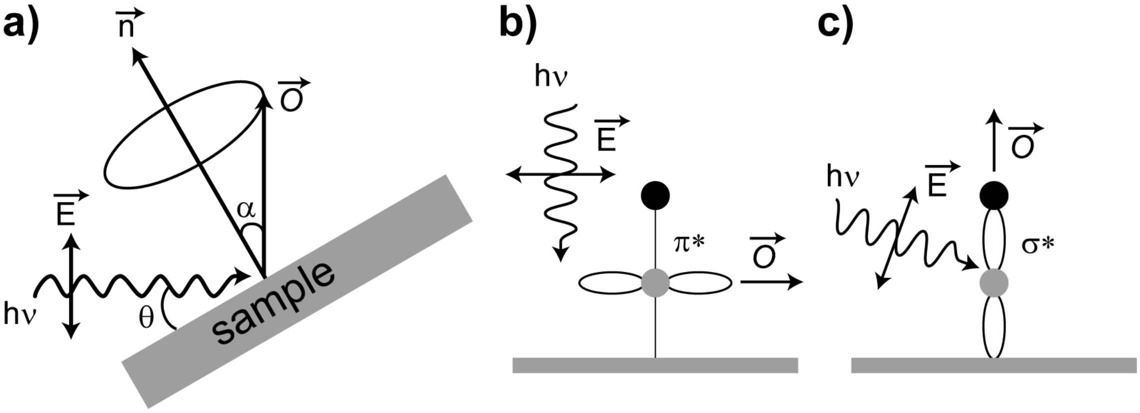

Figure 2.14: a) Schematic NEXAFS setup, showing the photon incident angle θ, the photon beam, h °, and the electric field vector, $\vec{E}$. The angle α reflects the angle between the surface normal $\vec{n}$ and the final orbital direction $\vec{O}$. b) and c) visualize the interaction of $\vec{E}$ with the π^* and the σ^* orbital of a diatomic molecule, whose bond is normal to the surface plane. Maximal intensity is recorded for b) normal incidence or c) grazing incidence respectively [33].

the density of the final state. The transition intensity depends on the orientation of the electric field vector $\vec{E}$ relative to the spatial orientation of the molecular orbitals, whose maximum orbital amplitude ($\vec{O}$ being the direction of the final state molecular orbital) are oriented either along (in the case of a σ^* orbital) or perpendicular (for π^*) to the bond axis. Assuming solely linearly polarized light, the matrix element of the equation $\left|\langle \psi_f \,|\, \vec{e} \cdot \vec{p} \,|\, \psi_i \rangle\right|^2$ can be simplified to $\left|\langle \psi_f \,|\, \vec{p} \,|\, \psi_i \rangle\right|^2$. In the case of the initial state being a 1s orbital and the final state being directional, the matrix element $\langle \psi_f \,|\, \vec{p} \,|\, \psi_i \rangle$ point in the direction of $\vec{O}$, which makes the transition intensity:

$$I \propto \left|\vec{e}\,\langle \psi_f \,|\, \vec{p} \,|\, \psi_{1s} \rangle\right|^2 \propto \left|\vec{e}\,\vec{O}\right|^2 \propto \cos^2 \delta$$

with δ being the angle between $\vec{E}$ and $\vec{O}$. This equation reveals, that the intensity of a resonance is maximal, if the electric field vector is parallel to the direction of the final state orbital, and minimal if they are oriented normal to each other. With recording NEXAFS spectra at three different incident angles (see figure 2.14), the orientation of bonds or whole molecules can be investigated [33].

2.2.3 Experimental setup

Figure 2.15 shows the setup of the end-station of the HE-SGM beamline at *BESSY II.* It consists of three chambers, namely the preparation chamber, the analysis chamber and

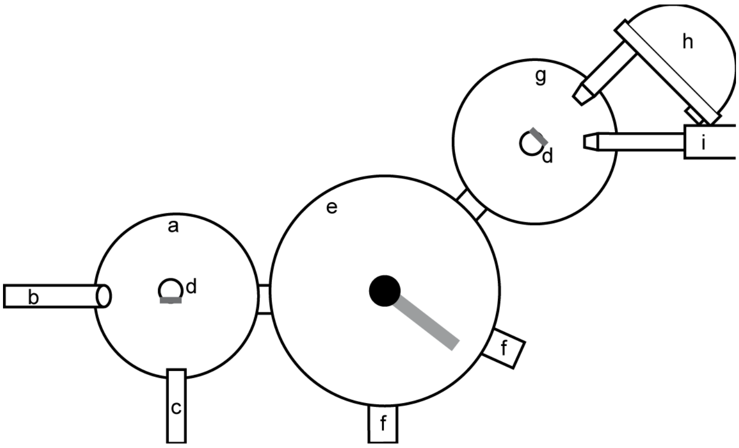

Figure 2.15: Setup of the fixed end station at the HE-SGM beamline at BESSY II: a) preparation chamber equipped with b) a organic molecular beam epitaxy (OMBE), c) sputter gun and d) manipulator. e) Transfer chamber with a turnable manipulator ("UFO"). f) Compartments such as a magazine and a loadlock are connected to the UFO. g) Analysis chamber with heatable and d) coolable manipulator, h) electron analysor and channeltron. i) Position of the beamline connection with the incoming photon beam.

a chamber with a rotatable transfer system which allows to transfer samples between the different chambers. The base pressures in the preparation and analysis chamber are 2×10^{-8} mbar and 2×10^{-10} mbar respectively. Both, the analysis and the preparation chambers are pumped with a system of turbo molecular pump supported by titanium sublimation pumps. The transfer chamber (figure 2.15e) is pumped by an ion getter pump. Preparation and analysis chambers are equipped with rotatable 3D manipulators at which it is possible to heat the sample by electron beam or resistively to more than 870 K, as well as cool the sample to 100 K. In addition, the preparation chamber is equipped with a sputter gun and an organic molecular beam epitaxy (OMBE). The samples are here prepared following the protocols described previously in subsection 2.1.4. The analysis chamber is equipped with a *Scienta R3000* hemispherical electron energy analyzer which is situated in an angle of 45° with respect to the direction of the incoming photon beam from the beamline. The channeltron detector used for NEXAFS measurements is located at approximately the same geometry as the electron energy analyzer (for this reason not shown in figure 2.15)

XPS spectra were recorded in normal emission. For the acquisition of the C 1s, N 1s, O 1s and S 2p spectra, the excitation energies were 435 eV, 550 eV, 680 eV and 305 eV, respectively. The binding energy scale was calibrated against the Ag $3d_{5/2}$ core level at a binding energy of 368.3 eV [38] or the Cu $2p_{3/2}$ at 75.1 eV [39]. After the subtraction of either linear or Shirley [40] background, peaks were fitted with Voigt functions.

The carbon and nitrogen K-edge spectra were recorded in partial electron yield mode with a retarding voltage of -150 V and -250 V respectively. The incident angle θ of photon light was altered by rotating the sample with respect to the incoming beam. Spectra were recorded at three angles of incidence: grazing (20° or 25°), magic angle (53°) and normal (90°). Simultaneously to the PEY spectra the photocurrent signal of a contaminated gold grid traversed by the X-ray beam was recorded. After referencing the energy scale against a characteristic peak at 285 eV for carbon or 399 eV for nitrogen, the signal of the bare crystal was subtracted from the sample spectrum, followed by a correction for the photon flux and a normalization of the edge jump to one.

3 Results

In this chapter, the results of the investigations performed along with the present thesis are presented. Besides the interaction of small biomolecules with a metal substrate, the influence of Co adatoms on the self-assembly of the RNA and DNA nucleobases uracil, adenine, cytosine and thymine and the uracil derivative orotic acid adsorbed on the Ag(111) surface was investigated by means of STM. From the overlayer structures found on the surface, there was no evidence of an incorporation of any metal adatoms into the molecular arrangement. Cobalt was found to cluster on the plane surface, accumulate at the boarders of molecular islands and occasionally in the interface of the molecular layer with the metal substrate, e.g. for adenine on Ag(111). Since no metal-organic networks are formed on the silver surface, this experiments are not described in details in this thesis and no further studies on this topic were performed. Section 3.1 describes the interaction of both cysteine enantiomers with the Ag(111) surface and the different phases which are forming dependent on surface coverage and sample annealing temperature. The adsorption behavior, self-assembly and chemical behavior of uracil dependent on its surface coverage and sample temperature is presented in section 3.2. It is followed (section 3.3) by a study of its 6-carboxy derivative, the molecule orotic acid, which is studied under similar conditions aiming to compare the results with the uracil study and getting insight insight in the influence of an additional substituent. The results of the study on self-assembly and chemical behavior of bisphenol A adsorbed on the Ag(111) and Cu(111) surface are shown in section 3.5.

3.1 L- and D-cysteine on Ag(111): Temperature- and coverage dependent phase transformations

Cysteine, as most other proteinogenic amino acids, is a chiral molecule with its chiral center on the C2-carbon (for labeling of the atoms, see figure 3.1). Among the 22 naturally occurring amino acids, L-cysteine (also *(R)*-cysteine) is the only one with a thiol side chain. The molecule is generally found in different proteins, especially in keratin, a group of fibrous structural proteins which are the building blocks of hair, nails, horn and many other similar biologic materials, where L-cysteine with its ability of forming disulphide bridges is in charge of the stiffness of the keratin fibers. In contrast to L-cysteine, due to its lack of biological relevance, the related D-enantiomer (D- or *(S)*-cysteine) is studied much less frequently. Comparative studies however have focused on the behavior of racemic mixtures of cysteine adsorbed on Au(110) [41–43]. As an amino acid, cysteine contains a carboxy and an amino group along with the previously mentioned thiol group. In solid form and in many solvents, amino acids adopt a zwitterionic configuration with the carboxy group deprotonated to carboxylate (R-COO$^-$) and the amino group protonated to ammonium (R-NH$_3^+$) as illustrated for L-cysteine in figure 3.1. On certain solid surfaces, some amino acids were found to adsorb as zwitterions [44–46], however, amino acids that deprotonate on bare noble metal surfaces at room temperature [47] and above [45] have been reported, resulting in formally negatively charged molecules (Figure 3.1). The thiol group is known to interact strongly with noble metals, such as gold, silver and copper [48] and binds covalently to them as thiolate. Therefore, cysteine is the most widely used anchor for longer peptides, for example at metal nanoparticles employed in bioanalytical and drug delivery protocols [49–51] or for molecular electronics concepts [11, 12]. To provide fundamental understanding of this type of interaction, the model system of cysteine on single-crystal metal surfaces has attracted considerable attention: past works examined the behavior of L-cysteine adsorbed on different faces of gold [41, 52–64], silver [65] and copper [55, 66] both in vacuo [41, 52–59, 66] and in solution [60–65], as well as with with density functional theory (DFT) calculations [57, 67, 68]. A DFT study on the adsorption of L-cysteine on Ag(111) published by Luque et al. [69] in 2012 investigates in detail two particular conformers on Ag(111) corresponding to the more stable local minima at the lowest (0.88 molecules/nm^2) and highest (4.56 molecules/nm^2) coverage. However, especially regarding the driving forces of structural rearrangements and the scission of the thiol bond upon room-temperature deposition, the aforementioned results are partly contradictory [52, 53, 55, 70].

The study presented in this chapter, which has been published in part previously [71], focuses on a comprehensive approach to clarify the chemical nature, anchoring and chirality of two dimensional layers of both cysteine enantiomers on the close-packed silver surfaces. While STM experiments clearly show the different phases of the adsorbed molecules on the Ag(111) surface and their temperature- and coverage dependent rearrangement, whereas XPS measurements provide information about the chemical state of the molecule in different phases. Information on the orientation of the functional groups with respect to the surfaces is gained by additional NEXAFS measurements.

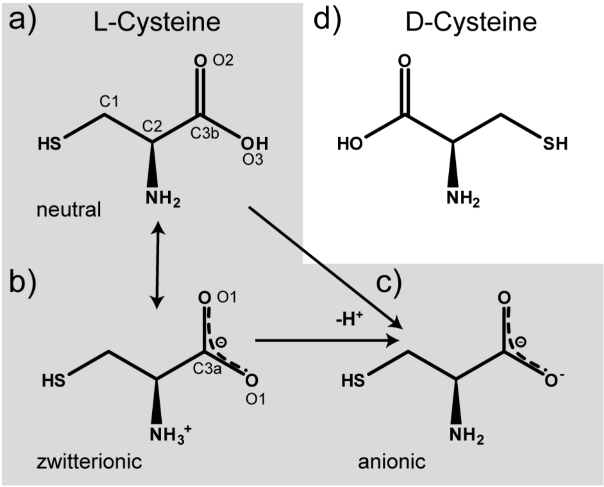

Figure 3.1: Structural formulas of a-c) L-cysteine in its a) neutral, b) zwitterionic and c) anionic form and of d) D-cysteine in its neutral form.

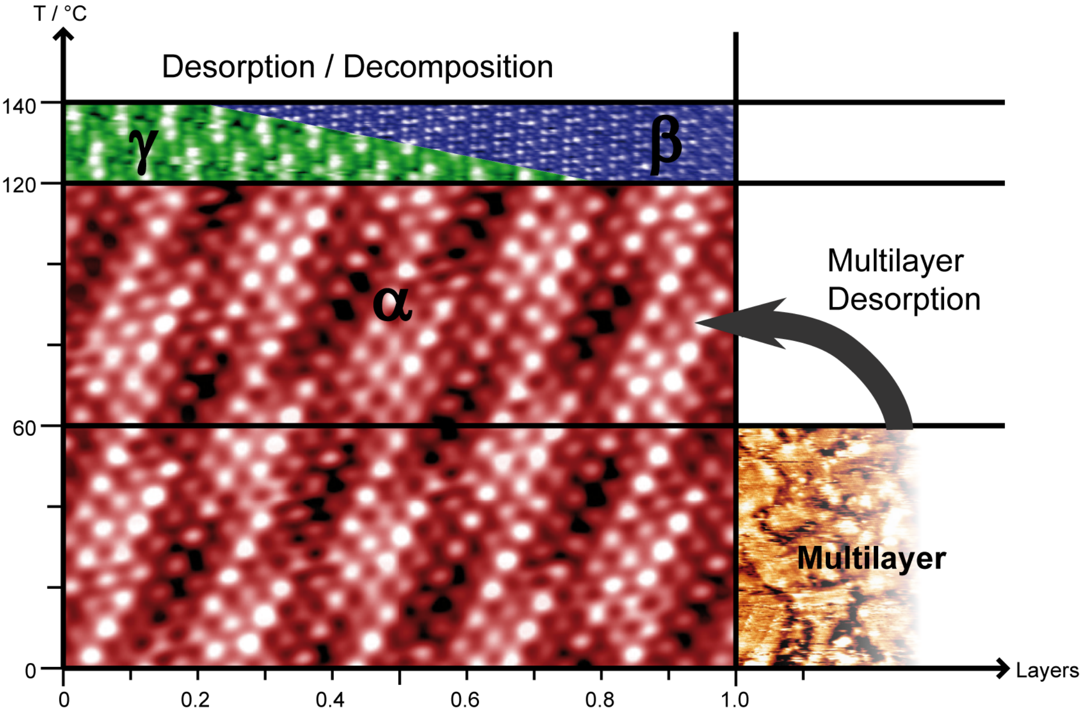

Figure 3.2: Overview of the different phases of cysteine on Ag(111) as a function of the surface coverage and the annealing temperature.

3.1.1 Microscopy

Upon deposition of cysteine on Ag(111) at room temperature, a close packed structure appears, which shows a clear moiré pattern (Figure 3.2, red). This structure (α) can be observed throughout all coverage regimes up to a full monolayer (1 ML (monolayer) being defined as 100% of metal surface covered by the adsorbate). Deposition of more than one monolayer of cysteine molecules leads to a multilayer without a clearly ordered structure (Figure 3.2, yellow), which desorbs when warmed to 333 K and above. After observing an intermediate unordered structure for annealing temperatures between 383 and 393 K, annealing to 393 K leads to a complete reorganization of the organic layer into two new arrangements dependent on the coverage. For coverages of 0.8 ML and above, solely a phase called β (Figure 3.2, blue) was observed while in the regime below 0.2 ML a phase called γ with lower density and a roughly hexagonal arrangement was found (Figure 3.2, green). For coverages between 0.2 and 0.8 ML, both phases coexist on the surface.

Figure 3.3 shows typical STM micrographs of the structure appearing upon room temperature deposition of a (sub)monolayer coverage of L-cysteine on Ag(111) (phase α). In the high resolution image (Figure 3.3a), bright protrusions corresponding to single cysteine molecules are discerned. The molecules build up a close packed hexagonal structure with a nearest neighbor distance of 5.8 ± 0.2 Å and a density of 3.66 molecules/nm^2. A moiré pattern evident in figure 3.3b indicates that the dense-packed layer is incommensurate with the underlying Ag(111) substrate. Incommensurate molecular layers of organic thiols adsorbed on Ag(111) [72] and Au(111) [73] surfaces have been observed in the past and indicate multiple adsorption sites of cysteine units. The unit cell axes of phase α are rotated by 30° with respect to the silver $\langle 1\bar{1}0 \rangle$ directions. In the submonolayer regime, molecules assemble into islands extending over 50 nm and occasionally covering the entire atomically flat terrace.

Annealing to 393 K leads to a rearrangement of the molecules into two phases with completely different appearance, phase β, which is present for higher coverages, and phase γ for lower coverages (Figure 3.2). The disappearance of the moiré pattern as well as the lower density suggests a change of the binding site selectivity of the molecules during heat treatment. The high coverage phase β consists of extended two-dimensional islands as well, but it is described by a rhombic unit cell of nine molecules with $a = 1.80 \pm 0.04$ nm, $b = 1.86 \pm 0.09$ nm and an angle of 70° between them (Figure 3.3c). That leads to a density of 2.78 molecules/nm^2, which is $\sim$ 75% of the density of phase α. It is characterized by molecular rows of cysteine (highlighted in red in figure 3.3d), running along the Ag(111) $\langle 1\bar{1}0 \rangle$ axis sandwiched between molecular rows with lower corrugation. The molecules comprising a pair are not arranged in parallel: instead, they are rotated by approximately

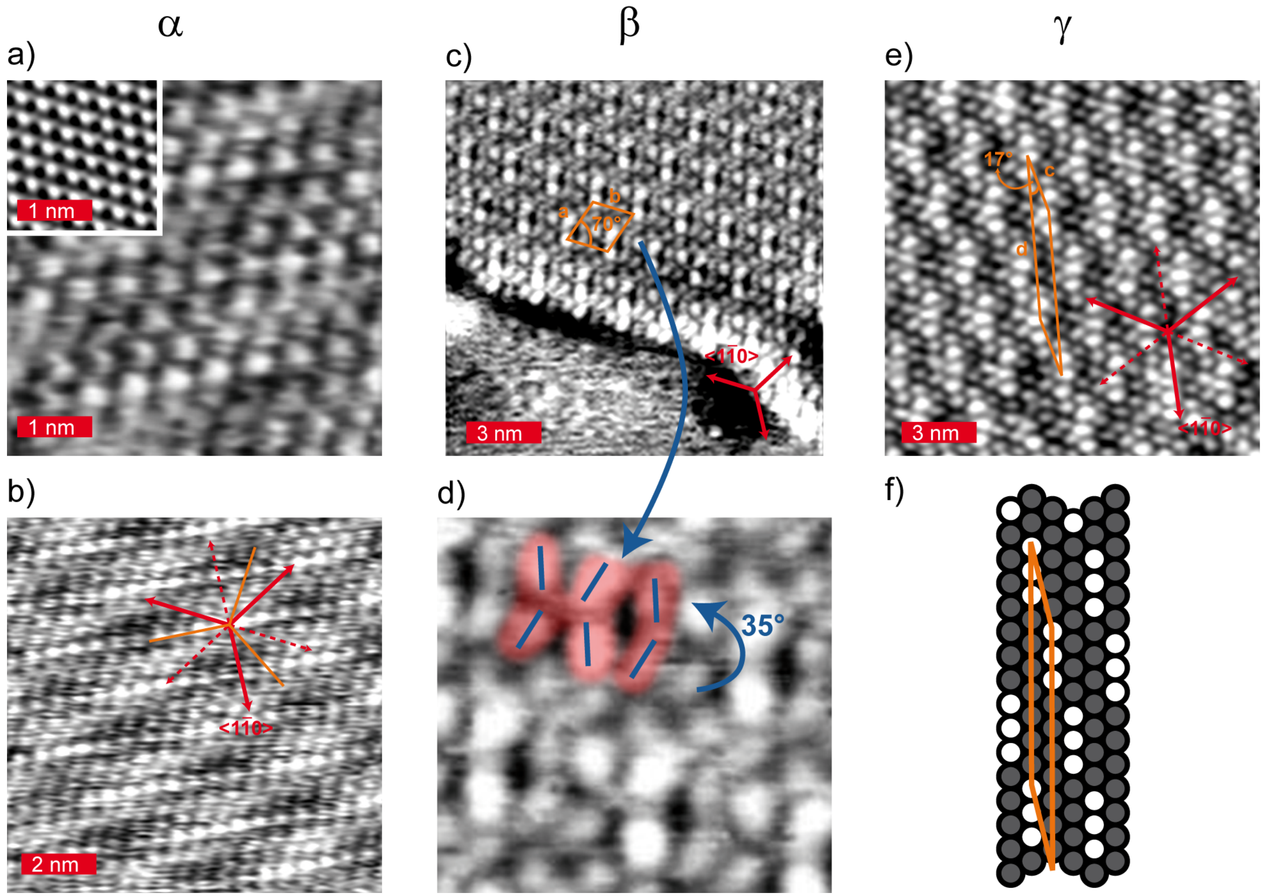

Figure 3.3: STM images of the different phases of L-cysteine adsorbed on Ag(111): a) Hexagonal structure α after room temperature deposition (I_t=100 pA, U_t=1.25 V). Inset: atomically resolved image of the Ag(111) substrate, I_t=-170 pA, U_t=-0.88 V.) b) Moiré pattern of the α structure with the orientation of the hexagonal arrangement indicated in orange (I_t=100 pA, U_t=1.25 V). (c) β structure formed after annealing the system to 393 K for coverages between 0.2 and 1.0 ML (I_t=320 pA, U_t=1.25 V) with the unit cell indicated in orange. d) Enlargement of c) with the molecular pairs lining up along the substrate $\langle 1\bar{1}0 \rangle$ direction, highlighted in red and their molecular orientation indicated in blue. e) γ structure formed after annealing to 393 K for coverages up to 0.8 ML with the unit cell indicated in orange (I_t=120 pA, U_t=1.25 V). f) Sketch of the quasi hexagonal arrangement of the γ structure with the unit cell drawn in orange. The high symmetry axes of the substrate are indicated in red in images b), c) and e).

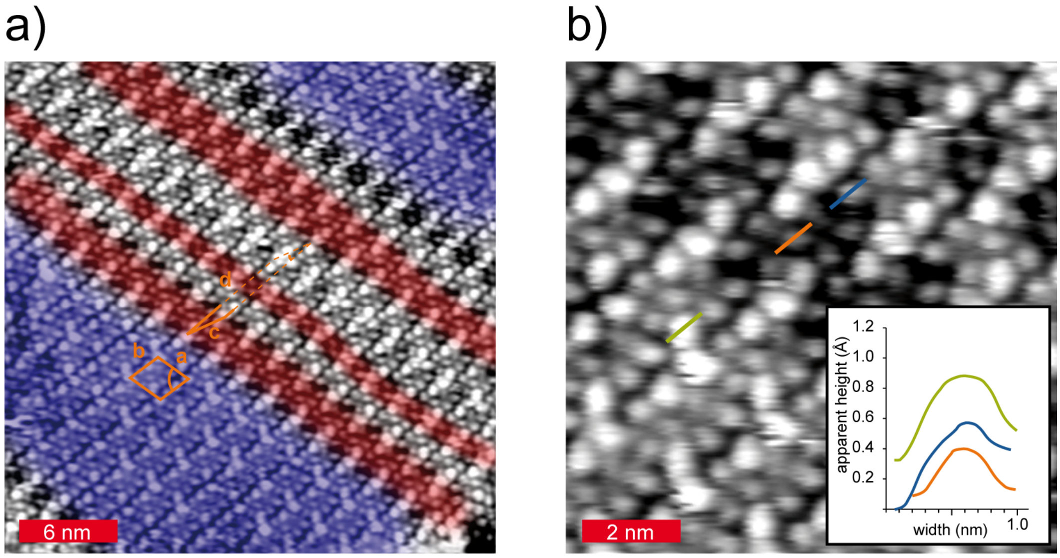

Figure 3.4: a) Island with alternating stripes of β (blue) and γ (red) phase of D-cysteine adsorbed on Ag(111) (I_t=120 pA, U_t=1.25 V). The axes b and d of the two unit cells align with the Ag(111) high symmetry axis. The grayscale areas are the border regions between the two structures, where neither of the structures can be clearly identified. b) Magnification of a) showing line profiles of three different molecular species featuring different apparent heights. Inset: Relative apparent heights of the adsorbates.

35° (Figure 3.3d), mirror images of each other with respect to the Ag(111) $\langle 1\bar{1}0\rangle$ direction. Looking at the pair rows along the high-symmetry axis, we also note that every third molecules has an increased apparent height by 0.3 Å compared to the other molecules. Apparent height differences in this range are close to the S-Ag(111) distance between S at atop versus hollow sites, as modeled for hydrogen sulfide and methanethiol on Ag(111) [74]. Alternatively, these variations might suggest chemically different, coexisting cysteine molecules in phase β: a plausible scenario that is addressed along with the results from the XPS measurements.

As well as β, phase γ consists of extended islands which are, due to the lower coverage, generally smaller in size. The molecules arrange in a nearly hexagonal pattern. The rhombic unit cell, which is described by the axes $c = 2.49 \pm 0.07$ nm, $d = 6.66 \pm 0.27$ nm and an angle of 17° between them (Figure 3.3e) incorporates 10 molecules, leading to a density of 2.06 molecules/nm^2, $\sim$ 74% of the density of β. The structure appears as rows of single molecules, in contrast to phase β, which are running along the $\langle 1\bar{1}0\rangle$ directions of the Ag(111) substrate. Three out of ten molecules appear brighter (for model see figure 3.3f), the difference in the apparent height between the molecules ranging between 0.4 and 0.6 Å.

In the coverage regime between 0.2 and 0.8 ML both phases coexist on the surface.

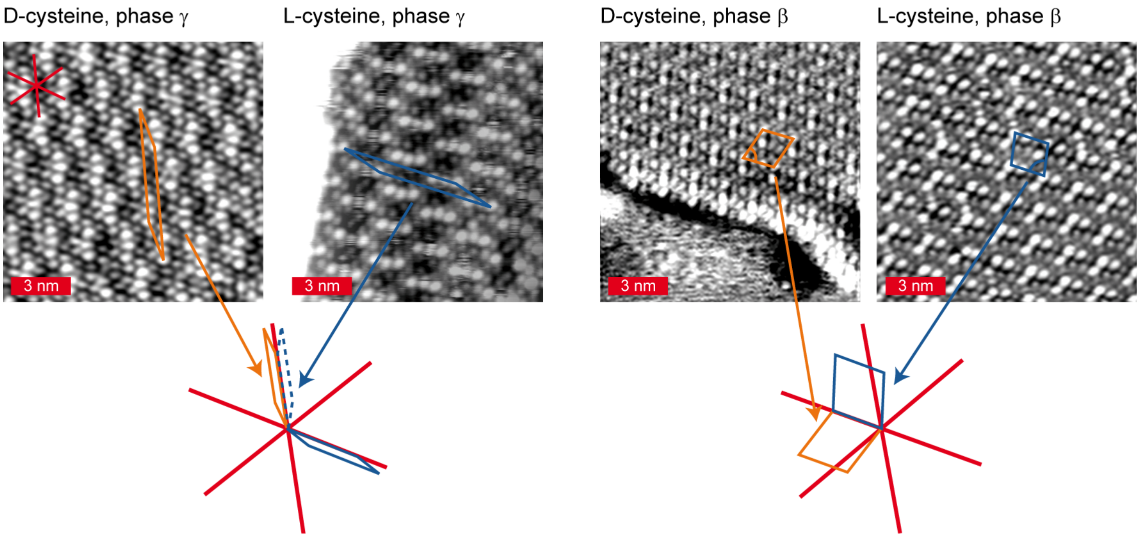

Figure 3.5: STM images of domains of phases γ (left) and β (right) reflecting the transfer of chirality from the two cysteine enantiomers to the two dimensional islands. The unit cells for the domains created by adsorption of L- or D-cysteine are indicated in orange and blue, respectively. The high symmetry axes of the underlying Ag(111) substrate are shown in red.

Instead of forming separated islands, stripes of the two structures with different widths alternate, forming one combined island (Figure 3.4a) where the directions b and d of the unit cells align with the same $\langle 1\bar{1}0 \rangle$ high symmetry direction of the substrate. Overall, the ratio of γ and β changes with increasing coverage in favor of the latter, even though this ratio might differ within a single island. Line profiles of these "combined" islands show protrusions featuring three different apparent heights (Figure 3.4b), indicating different molecular species co-existing on the surface. Additionally to the transformation from α to γ, a transformation from β to γ is observed. Extensive annealing of a sample featuring a monolayer coverage of adsorbed cysteine at 413 K, the onset of molecular desorption, leads to a reduction of the surface coverage and the appearance of phase γ. Comparing the STM micrographs of both enantiomers, only the three clockwise symmetrically equivalent domains for D-cysteine and the three mirrored domains with respect to the substrate high symmetry axes for L-cysteine (shown in figure 3.5) are found, reflecting the transfer of chirality from the molecule to the assembled structures β and γ.

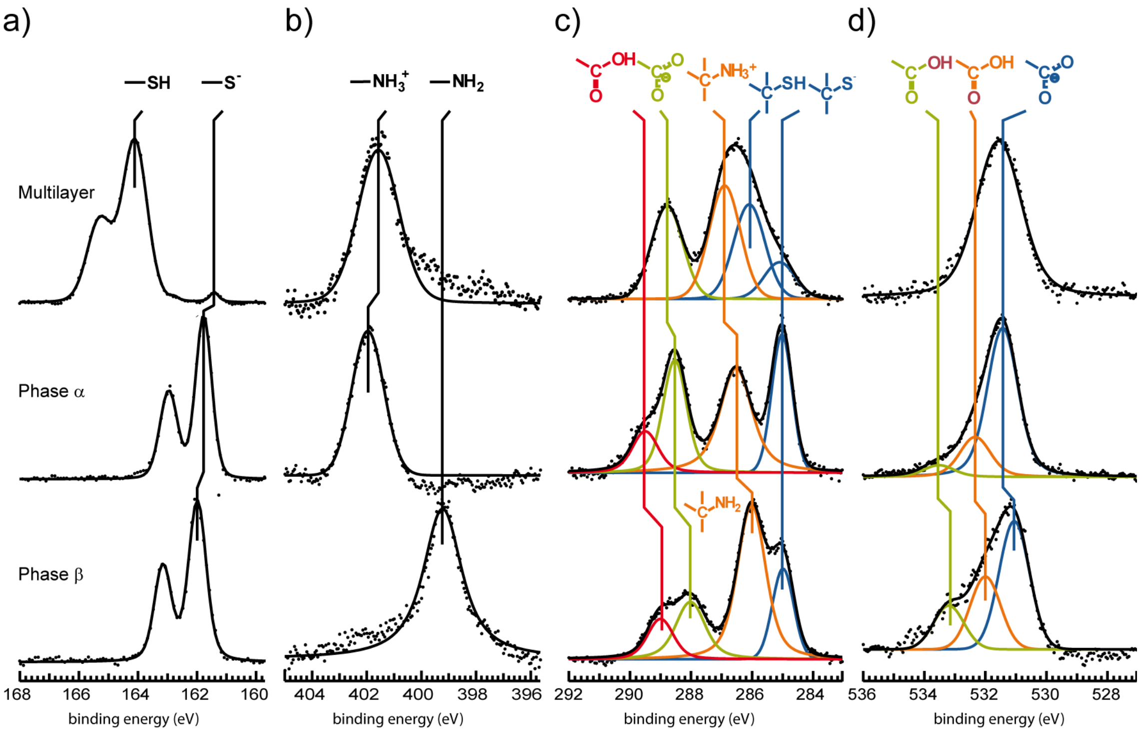

Figure 3.6: High-resolution X-ray photoelectron spectra of the a) S 2p, b) N 1s, c) C 1s, and d) O 1s core levels of an as-deposited multilayer film (top), of phase α (middle), and of phase β (bottom) on Ag(111).

3.1.2 X-ray spectroscopy

XPS investigations:

To analyze the chemical state of the adsorbed cysteine and to clarify the reason for the layer transformation during heat treatment, XPS experiments for a full monolayer coverage of L-cysteine on Ag(111) were performed. For comparison with the pristine molecule, the core level binding energies of a L-cysteine multilayer on Ag(111) were measured. In the multilayer, the S $2p_{3/2}$ appears with a binding energy of 164.4 eV (Figure 3.6a, top), indicating an intact thiol group. The O 1s signal of a single peak at 531.6 eV (Figure 3.6d, top), typical for carboxylate groups in zwitterionic molecules [54, 55, 75], as well as the binding energy of the single peak in the N 1s region (Figure 3.6b, top) clearly show the multilayer film to contain predominantly molecules in the zwitterionic state as expected [55] and demonstrates the successful and controlled deposition of intact L-cysteine molecules. The C 1s signal (Figure 3.6c, top) comprises a broad feature at a binding energy of 286.5 eV due to a combination of C1 (C1 being the thiol-related carbon of the physisorbed L-cysteine) and C2 (ammonium-related carbon) species and a feature at 288.8 eV from the carboxylate-related C3a carbons (for the labeling of the carbon atoms see figure 3.1) [75]. The small energy shoulder at 285.1 eV originates from thiolate species of the first chemisorbed layer (C1a) because the thickness of the prepared film ($\sim$ 3-4 molecular layers) is smaller than the photoelectron escape depth. It could also be assigned to the thiolate signal of the unconventional zwitterion with a negatively charged sulfur, a positively charged ammonium-group, and an intact carboxy group; however, this species has been reported to be stable only up to 200 K [76].

The XP spectrum of the S 2p region of phase α shows a single doublet with the S $2p_{3/2}$ signal at a binding energy of 161.8 eV (Figure 3.6a, middle). This downward shift of 2.6 eV between the multilayer and phase α marks the chemisorption of L-cysteine via a thiolate end group in phase α [53, 54]. The N 1s region of phase α shows a single peak at a binding energy of 402.0 eV (Figure 3.6b, middle), typical for a L-cysteine ammonium group (-NH_3^+) [54]. The corresponding O 1s core level consists mainly of a peak at 531.6 eV (Figure 3.6d, middle), which can be attributed to a a carboxylate group (-COO^-) [54], The peak width is significantly smaller with respect to the multilayer (the fwhm decreases from 1.8 to 1.2 eV), which indicates a homogeneous local environment for the surface-confined carboxylate group. It can be deconvoluted in contributions from O1 (531.4 eV) and minority species O2 (532.3 eV) and O3 (533.5 eV), corroborating the presence of both carboxylate and carboxyl groups in the phase α with the carboxylate species dominating [54]. Since the amino group is fully protonated, the additional proton likely originates from the scission of the S-H bond. Accordingly, the C 1s spectra of

assignment	multilayer		phase α		phase β	
assignment	E_B(eV)	relative intensity (%)	E_B (eV)	relative intensity (%)	E_B(eV)	relative intensity (%)
C1a	285.1	11	285.0	26	285.0	19
C1	286.1	28				
C2	286.9	34	286.5	39	286.0	52
C3a	288.8	28	288.5	27	288.0	20
C3b			289.5	11	289.0	12
O1	531.6	100	531.4	76	531.0	52
O2			532.3	20	532.0	30
O3			533.5	6	533.2	18

Table 3.1: XPS core-level peak assignment of the C 1s and O 1s regions for multilayer, phase α, and phase β of L-cysteine on Ag(111).

a monolayer sample featuring phase α can be well fitted with four components (Figure 3.6c, middle). The peak with the lower binding energy (285.0 eV) is attributed to the thiolate carbon (C1a) and thus is shifted to lower energies with respect to the thiol carbon (C1) [54, 75]. The ammonium-related feature (C2) shifts by $\sim$ 0.4 eV to lower binding energies with respect to the multilayer, due to the multilayer-to-monolayer transition. Finally, the two signals at 288.5 and 289.5 eV originate from the carboxylic carbon (C3), the former stemming from the carbon of the deprotonated carboxylate group (C3a), whereas the latter from the -COOH group (C3b) [54]. Table 3.1 summarizes the binding energies and the relative intensities of the C 1s and O 1s peaks. The relative intensities are varying up to $\sim$ 50% with respect to the expected atomic ratios of the chemically different atoms of L-cysteine, a discrepancy that can be tentatively associated with diffraction effects from the substrate [77]. This leads to the conclusion, that L-cysteine molecules in contact with Ag(111) follow a predominantly zwitterionic bonding scheme in phase α. Similar core-level binding energies of N 1s and O 1s have been observed and identified also for tyrosine and methionine on coinage metal surfaces, underlining the general trend in the amino acid zwitterionic bonding motif [44–46].

Upon annealing and formation of phase β, the S 2p core-level binding energy remains virtually unchanged (Figure 3.6a, bottom). A shift of 0.2 eV towards higher binding energy in the S 2p signal of phase β is associated with the difference in the local environment of the thiolate, going along with the structural transformation. With the conversion to the β structure, the N 1s signal shifts by approximately 3.0 eV to a lower binding energy of 399.2 eV (Figure 3.6b, bottom), which is consistent with a deprotonation of the former ammonium cation of phase α to an amino group (-NH_2) [53–55, 70]. The observed energy shift of the nitrogen is not abrupt, but the result of a decrease in the ammonium-related signal and a concurrent increase of the amino-related signal within a temperature range of 383-393 K. This change is also affecting the amino-related carbon (C2), which shifts downward by 0.5 eV, presumably due to the interaction with the surface via the nitrogen lone pair. Concurrently, the oxygen peak ratio of carboxylate to carboxyl components increases (Figure 3.6d, bottom), indicating that the carboxylate group captures a fraction of the proton lost from the ammonium groups. The O 1s peaks and the two related carbon (C3) peaks exhibit shifts of -0.3 to -0.5 eV, which probably result from increased hole screening due to polarization of the metal surface in phase β. Such an increased screening is consistent with the assumption, that the oxygens and C3 carbons are closer to the silver surface than in the phase α, a consideration that is taken into account in the proposed models below. This mixture of formally negatively charged and neutral adsorbed L-cysteine species might account for the different STM appearance of the adsorbates in phase β. Regarding the fact, that all phases that were observed by means of STM are quasi identical for both L- and D-cysteine and only differ in their orientation with respect to the surface, it can be assumed that this investigations account for both enantiomers.

Taking into account that the formation of phase γ is, as described in subsection 3.1.1, dependent on the molecular surface coverage and a structural change of phase β to phase γ is possible by reducing the surface coverage, one might expect that the ammonium group is also deprotonated in phase γ. However, due to the lower density, the interaction of the molecule with the surface may change, which in turn might lead to a difference in the ratio of neutral and anionic molecules, i.e. the ratio of carboxylic to carboxylate moieties, with respect to phase β. This tentative interpretation can account for the phase transformation from β to γ and partly explains the different apparent heights observed in the STM images. Indeed a coverage dependent deprotonation of the carboxylic group has also been observed for orotic acid (subsection 3.3.2) on Cu(111): at higher molecular coverage, the -COOH group is protected against deprotonation.

NEXAFS measurements:

The molecular conformation of the L-cysteine phases α and β was further investigated by angular-dependent NEXAFS. The NEXAFS spectra exhibit two main resonances at a photon energies of 290.0 eV and 288.7 eV, related to the σ^* orbital of the C-N bond (green components in figure 3.7a and b) and the π^* system of the carboxy group (blue components in figure 3.7a and b), respectively [56, 66, 78–80]. The curve-fitting analysis of the angular dependent NEXAFS (blue circles in figure 3.7c and d) of the latter shows the direction of the final state orbital $\overrightarrow{O}$, which is the direction of maximum orbital amplitude, is approximately 60° in both phases. Thus, for the π^* resonance of the carboxy group, $\overrightarrow{O}$ is normal to the plane defined by the group resulting in a tilt of the carboxy group of

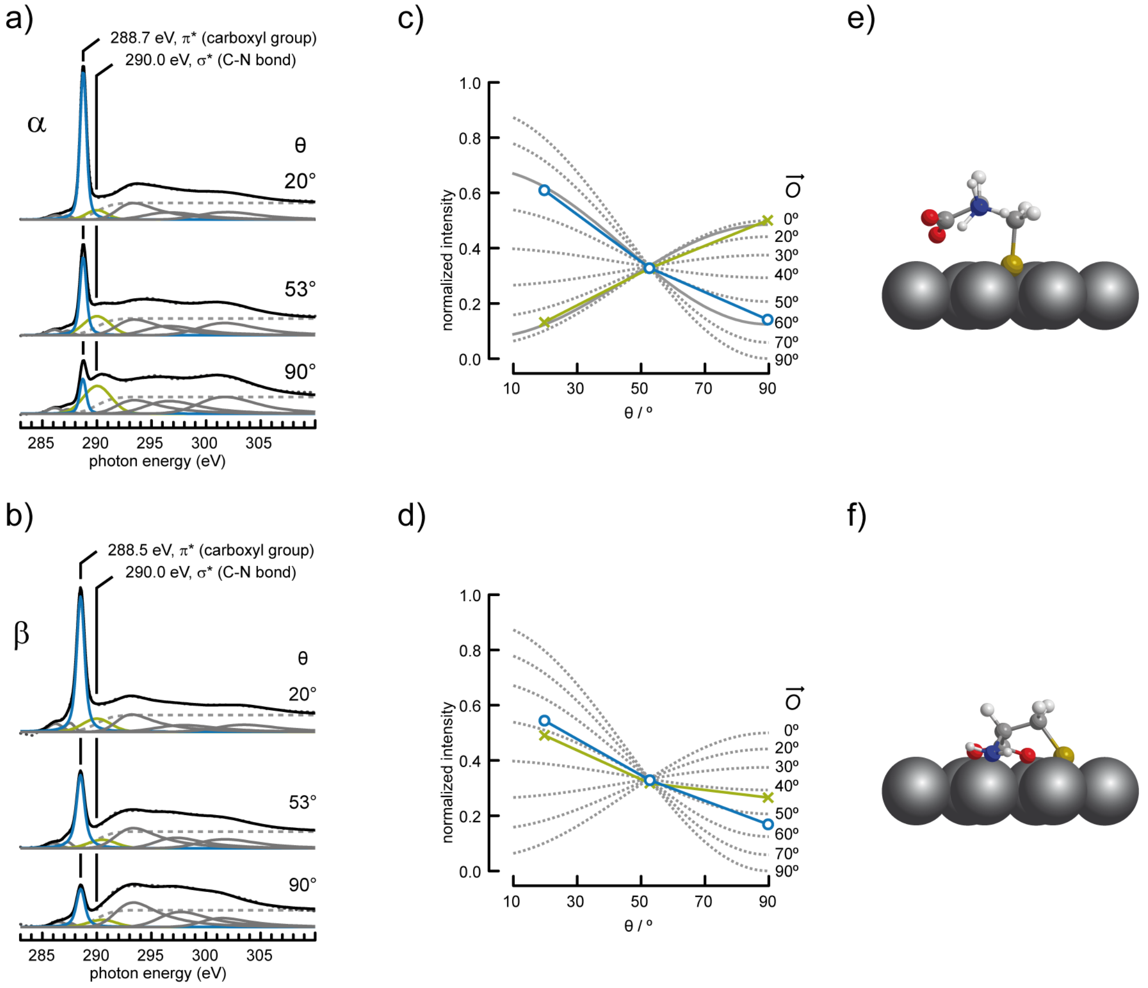

Figure 3.7: a-b) Fitted C K-edge NEXAFS data acquired at three angles of photon incidence, θ, of a) phase α and b) phase β. c-d) Curve-fitting analysis of the photon angle dependence of the carboxy group π^* resonance (blue) and the amino group σ^* resonance (green) to estimate the corresponding directions of the final state orbitals $\vec{O}$ in c) phase α and d) phase β. e-f) Tentative local adsorption models of L-cysteine in e) phase α, where the COO$^-$ plane is tilted by $\sim 30°$ with respect to the surface, whereas the C-N bond is tilted $\sim 10°$, and f) phase β, where the COO$^-$ plane remains tilted by $\sim 30°$, but the C-N bond tilts further to 40-50°.

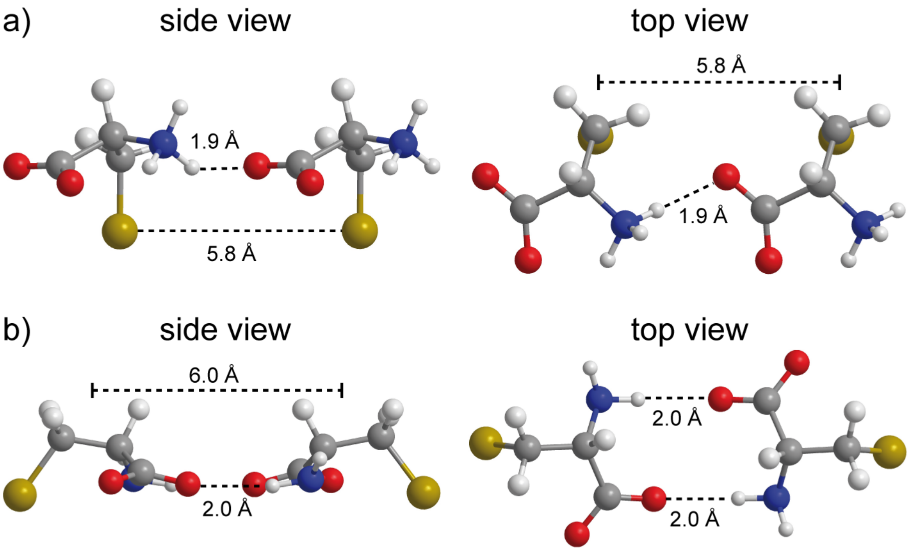

Figure 3.8: Tentative models of L-cysteine in a) phase α and b) phase β in a ball-and-stick representation.

approximately 30° with respect to the surface in both phases. In contrast, the C-N bond changes its orientation (the σ^* resonance $\vec{O}$ is along the C-N axis, green crosses in figure 3.7c and d) during the phase transformation from being nearly parallel to the Ag(111) surface in phase α to a tilt angle of 40-50° with respect to the substrate in phase β; e.g. there is a marked conformational change, as illustrated in figure 3.7e and f). As NEXAFS is providing information for the whole surface molecular ensemble and as it is shown along with the XPS data that different molecular species coexist in both phases α and β, the calculated tilt angles represent the average tilt angles of the L-cysteine molecules. As it was discussed for the XPS data, due to their equivalent behavior shown in STM investigations, it can be assumed, that both enantiomers, D- and L-cysteine show the same behavior concerning their orientation towards the surface.

3.1.3 Modeling

To test the consistency of the experimental data with a physically reasonable model, a molecular packing model for L-cysteine in phase α (Figure 3.8a) and phase β (Figure 3.8b) is proposed here. The atomic coordinates of the conformations in the two phases were obtained by allowing rotations of the existing L-cysteine σ bonds, until the geometry was consistent with the NEXAFS results. Aware that the STM and XPS data suggest distinct coexisting species in all three phases, for the present simplified picture, only the majority species present for each phase were taken into account, e.g. zwitterions for phase α and anions for phase β. The average intermolecular distances derived from the STM data were used to define the offset distance for the second molecule (5.8 Å in phase α, 6.0 Å in phase β). For both phases, it is well possible with these restrictions to construct molecular layers which are stabilised by intermolecular hydrogen bridges. The O$\cdots$H distances for these models are 1.9 Å and 2.0 Å for the zwitterionic and the anionic phase, respectively. This tentative model suggests that in the zwitterionic case, the cysteine molecules optimize the carboxylate-ammonium interaction and exhibit a more upright conformation (S - C bond nearly perpendicular to the surface). A DFT study on the conformation of L-cysteine on Ag(111) [69] reports the zwitterionic molecule being chemisorbed to the surface by the sulfur, as reported in the present study, but only appearing at high coverage. In our experimental study only phase α is formed, independent of the surface coverage. The density of α is smaller than the one considered by the DFT study (3.66 vs. 4.56 molecules/nm^2), giving enough space for the C-N bond to tilt toward the surface instead of tilting away from the surface. They also report a weakening of the silver-sulfur bond with increasing coverage and lateral interactions. The bonding energies of all different binding sites on the silver surface are within an energy range of less than 0.2 eV and form local energy minima. These results support our explanation of the L-cysteine phase α, whose self-assembly is driven by the strong intermolecular Coulombic interactions rather than by the surface binding site specificity as also evidenced by the moiré pattern. Such strong intermolecular interactions were also found in the self-assembled monolayer of the zwitterionic L-cysteine molecules on Au(111), which was stabilized by hydrogen bonding [81]. In contrast, in the anionic phase, cysteine is accomplishing a more planar conformation optimizing the molecule-surface interaction in a tetradentate mode with all functional groups connected to the surface. For lower surface densities DFT calculations [69] of a neutral L-cysteine molecule on Ag(111) show strong interactions of the carboxy group with the silver surface and there is an indication that the oxygen participates in the bond with the surface. Even though these calculations refer to L-cysteine at very low coverage, they support the suggested bonding scheme of the molecule in phase β. The interactions between functional groups and the surface mainly stabilize the molecules on the silver surface in this phase; in addition lateral H-bonding and van der Waals interactions should be taken into account in order to explain the assembly of the molecules on the surface. The observed pairing of the molecules in phase β strongly suggests a head-to-head interaction, which can be stabilized by H-bonds as shown in figure 3.8b.

3.1.4 Summary and conclusions

By combining STM and X-ray spectroscopy data, the chemical nature of the room-temperature adsorption of cysteine on the Ag(111) surface could be shown and the driving forces of the structural changes induced by annealing were investigated and understood. Upon room temperature deposition, cysteine chemisorbs via its sulfur, in contrast to the behavior shown for L-cysteine on Au(111) [52, 82], and forms a dense-packed layer. When the coverage increases beyond a monolayer, further cysteine layers physisorbed on top of the chemisorbed layers. In this phase, cysteine exists mainly as a zwitterion, having a protonated amino group and a deprotonated carboxy group. Annealing to 333 K leads to a desorption of the multilayer, leaving only the chemisorbed cysteine monolayer of phase α on the surface. The monolayer molecules chemisorb in a hexagonal arrangement with a nearly upright conformation, the plane of the carboxylate group tilted by approximately 30° with respect to the surface and the amino group C-N bond being almost parallel to the surface. The molecular assembly with a density of 3.66 molecules/nm^2 is rather stabilized by intermolecular hydrogen bonding than by the interaction with the surface, resulting in a reduced surface site bonding selectivity and showing a moiré pattern. Further annealing to 393 K induces a phase transformation into the coverage dependent phases β and γ. The high coverage phase β involves a deprotonation of the ammonium group resulting in a majority of formally negatively charged cysteine molecules and a minority of neutral molecules, where the carboxylate group captures the nascent proton from the deprotonation of the ammonium group. While many amino acids have been reported to adsorb in an anionic form [47, 78–80, 83–85], temperature induced deprotonation of the ammonium group has only been reported for methionine, the only other sulfur containing proteinogenic amino acid, on Cu(111) [45]. In that case, the strength of the molecular anchoring to the surface was caused by the higher reactivity of the copper substrate, hence a similar transformation does not occur on the more inert silver surface. For the high coverage phase β, NEXAFS measurements show, that simultaneously with the deprotonation, the amino C-N bond tilts further towards the surface, while the tilt angle of the carboxylate group with respect to the surface remains virtually unchanged. Along with the decreased molecular density determined by STM measurements, a molecular orientation is suggested, in which the amino group as well as the carboxy group interact with the surface via their electron lone pairs. Similar binding motifs have been reported for the amino acids L-alanine and glycine adsorbed on Cu(111) and Cu(110), where nitrogen atoms coordinate to the substrate in near-atom positions and the oxygens bind to the copper in off-atop positions. This type of configuration has been inferred from XPS, X-ray photoelectron diffraction, NEXAFS and DFT modeling [47, 80, 86]. The formation of phase γ is observed upon annealing the sample to 393 K, but for lower initial surface coverage, resulting in a structure with a decreased molecular density (approximately 74% of the density of β). Accordingly a phase transition from β to γ has also been observed upon extensive annealing, it is proposed that the ammonium group is deprotonated in phase γ. However, the lower density leads to an altered interaction between molecules and surface which might result in a different fraction of the carboxy-group being protonated. The absence of molecular pairs, as described for β, indicates intermolecular interactions other than the proposed head-to-head pairing. Presumably, a fine interplay in the intermolecular and molecule-surface interaction is driving the formation of the different structures.

In conclusion, these experiments show that the cysteine thiol group deprotonates into thiolate upon deposition at room temperature on Ag(111), allowing a robust anchoring of the molecule to the substrate without showing pronounced site selectivity. The robust anchoring resulting from the metal-sulfur molecular binding is essential for the temperature induced deprotonation of the ammonium group, resulting in a mixture of molecules existing in either a formally negatively form or a neutral form. The deprotonation comes along with a conformation change into a molecular orientation in which all functional groups interact with the silver surface. The mechanism is reported for the first time for a molecule on the mainly inert silver surface and hitherto it is unknown, whether this can be transferred to other noble metal surfaces.

These observations can offer new pathways in tailoring biofunctionalized surfaces. Cysteine and cysteine-containing peptides or larger biomolecules can be tethered to noble metal surfaces or metal nanoparticles allowing temperature induced changes between chemical forms and further specific chemical reactions for the creation of tailored surfaces.

3.2 Uracil on Ag(111) and Cu(111): Self-assembly and chemical transformations

Besides amino acids which are the building blocks of proteins, DNA and RNA nucleobases are another important group of biological molecules. Uracil (figure 3.9) is an RNA base, in particular the base differentiating RNA from DNA, and as such plays a vital role in biological interactions of major importance, notably those governing information transport and catalytic functions. Historically, uracil has been employed in the 1961 illustrious experiment of Nirenberg and Matthaei [87], which demonstrated that polyuridylic acid translates into a protein of poly-L-phenylalanine, functioning as a synthetic template or mRNA and therefore cracking the first genetic codon, UUU. Currently, the advance of RNA deciphering has shown that, together with adenine, uracil is a part of all three stop codons.

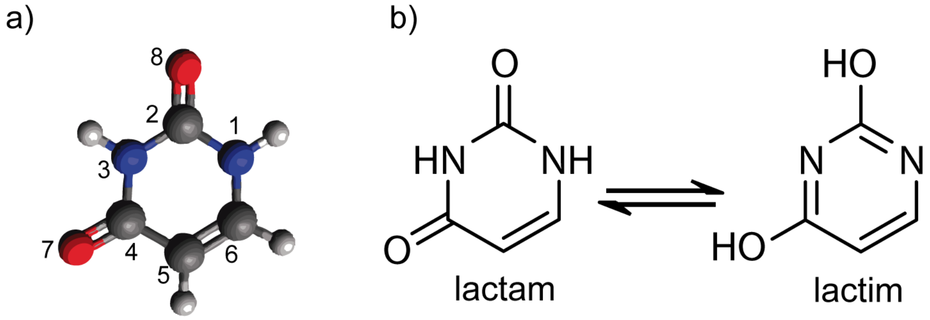

Figure 3.9: Uracil: a) 3D ball-and-stick model in its canonical form showing the labeling convention for the constituent atoms and b) molecular structure highlighting the lactam and lactim tautomers, the most comonly observed uracil tautomers in nature.

The surface adsorption and self-assembly of the fundamental building blocks of the genetic code and especially of the nucleobases have been the subject of intensive investigations in the last decades. There is a twofold aspect in these works. One part focuses on gaining a fundamental understanding of biological reactions on surfaces. For instance, the adsorption of biological molecules on inorganic solids is regarded as a relevant prebiotic process, and it is considered to be related to the origin of life [88].

Also, insight into the behavior of these building blocks similarly provides potential in biomimetic applications. Nature is extremely successful in performing tasks such as information storage, transfer, and catalysis by using these building blocks. Hence in the emerging field of nanotechnology, which focuses on the interactions between nanoscale moieties [89, 90], biomimetic applications have been proposed for performing the same tasks [91, 92].

The unique chemical functionalities of nucleobases offer a plethora of possible applications: their potential for chiral recognition on surfaces, an important target of the fine chemical industry, was shown by the elegant work of Chen and Richardson, who visualized the enantiomeric interaction between adenine and phenylglycine on the Cu(110) surface [93]. In the field of surface nanoarchitectonics they have been used as monomers or moieties, which offer multiple sites for hydrogen bonding, in binary and ternary supramolecular networks [94–96]. Additionally DNA bases offer the possibility of metal ligand interactions [97], thus of engineering metal–organic networks [98, 99]. Their attractiveness is obvious, being inexpensive, nontoxic, and biocompatible. However, in order to harness their full potential in such applications, it is vital to be able to predict their chemical reactivity toward the employed templates, which include close-packed coinage metals, TiO_2, and graphite.

These reasons have spurred numerous studies on the adsorption of nucleobases, which will not be discussed here in detail, however the findings of the here presented study are discussed alongside previous work on uracil and the related DNA base, the 5-methyluracil, thymine. Briefly, uracil was studied by STM on MoS_2, where it assembles into islands with clearly distinguished dimers, which do not correlate to the uracil single-crystal structure [100, 101]. On the more inert support graphite, STM showed a structure that bears a close resemblance to the single crystal [100–102]. On Cu(111), trimeric units form at low surface coverage, whereas at higher surface coverage two-dimensional domains form, which were also modeled with a trimeric motif [103]. All the above studies assumed adsorption of uracil in its lactam form. However, vibrational spectroscopy revealed that uracil on Si(100)-2×1 adsorbs in its lactim form and interacts with the surface by cleavage of the O-H bond [104]. On Cu(110) photoelectron diffraction (PhD) coupled with XPS and NEXAFS indicated that N-H cleavage allows coordination to the surface with both O atoms and the N atom (N3) in between [105]. Finally, on Au(100) [106–108], Au(111) [107], and Ag(111) [109], cyclic voltammetry experiments showed uracil to switch from physisorbed to chemisorbed state. A recent DFT study of uracil adsorbed on Au(100) [110] reveals that lateral interactions between the molecules mainly drive the self-assembly rather than covalent bonding to the surface, indeed, a flat adsorption geometry is crucial for strong intermolecular hydrogen bonding.

Despite this extensive volume of work, there is a lack of multitechnique studies to unravel the fine interplay of uracil's functional units with the underlying substrate, which determines the molecule's chemical state, bonding configuration, and the resulting self-assembly scenario. Here, a comprehensive study of uracil on Ag(111) and Cu(111) is presented. Silver and copper were chosen as commonly employed templates for molecular self-assembly and engineering of biomolecular nanostructures confined in two dimensions. The present study includes experimental investigations combining STM, XPS, and NEXAFS coupled with DFT simulations to elucidate the surface bonding and the charge transfer between the surface and the molecule as well as intramolecular electronic changes. Structural aspects were characterized at the molecular level by STM, revealing exquisite details of an intricate self-assembly scenario on Cu(111), which could be understood only by the complementary spectroscopic investigations and first-principles modeling using DFT. In particular, it is shown that the nanostructures formed are decisively influenced by specific interactions of uracil functional groups with the metal surface driving chemical transformations, which were previously unknown.

3.2.1 Uracil on Ag(111)

STM:

As a model system, where intermolecular interactions prevail in the molecular surface organization, the system uracil on Ag(111) was investigated. Figure 3.10 shows a typical STM image corresponding to uracil in contact with the hexagonal substrate. It is characterized by a uniformly packed structure. The close-packed islands furnish areas adjacent to step edges, without completely wetting the step edge. This is somewhat different from the observation of monolayer growth of uracil on Au(111), where the molecules form one-dimensional filaments at low coverages, but as the coverage increases toward the saturated monolayer, close-packed two-dimensional islands form [94]. Similar to orotic acid (subsection 3.3.1), on Ag(111) close-packed islands at uracil coverages as low as 0.3 ML are observed. The molecule-to-molecule distances are measured to be within the range of 7-9 Å, consistent with flat-lying hydrogen-bonded molecules. The self-assembled layer has a loose connection to the substrate high-symmetry axes, but the broad spots of the fast Fourier transform (FFT) STM image in the inset of figure 3.10a indicate that the registry of uracil to the Ag surface is not perfectly regular and therefore suggest an intermolecular interaction-driven pattern formation. As it was pointed out in a theoretical study of the 10 uracil homopairing possibilities, the energetically most favorable two-dimensional assemblies are not necessarily formed using only the most stable pairs, but other potential pairs may also be involved to accommodate additional bonding between nearest molecules [111]. For instance, the same authors found that the 21 possible adenine hydrogen-bonded homopairs can result in thousands of possible monolayer structures, many of which have similar lattice vectors [111, 112]. So it comes as no surprise that in a system with a very weak interaction between surface and molecule, where the surface acts mainly to confine the overlayer in two dimensions and not as a strict directorial template, there is poor long-range ordering of the resulting overlayer. An illustration of these

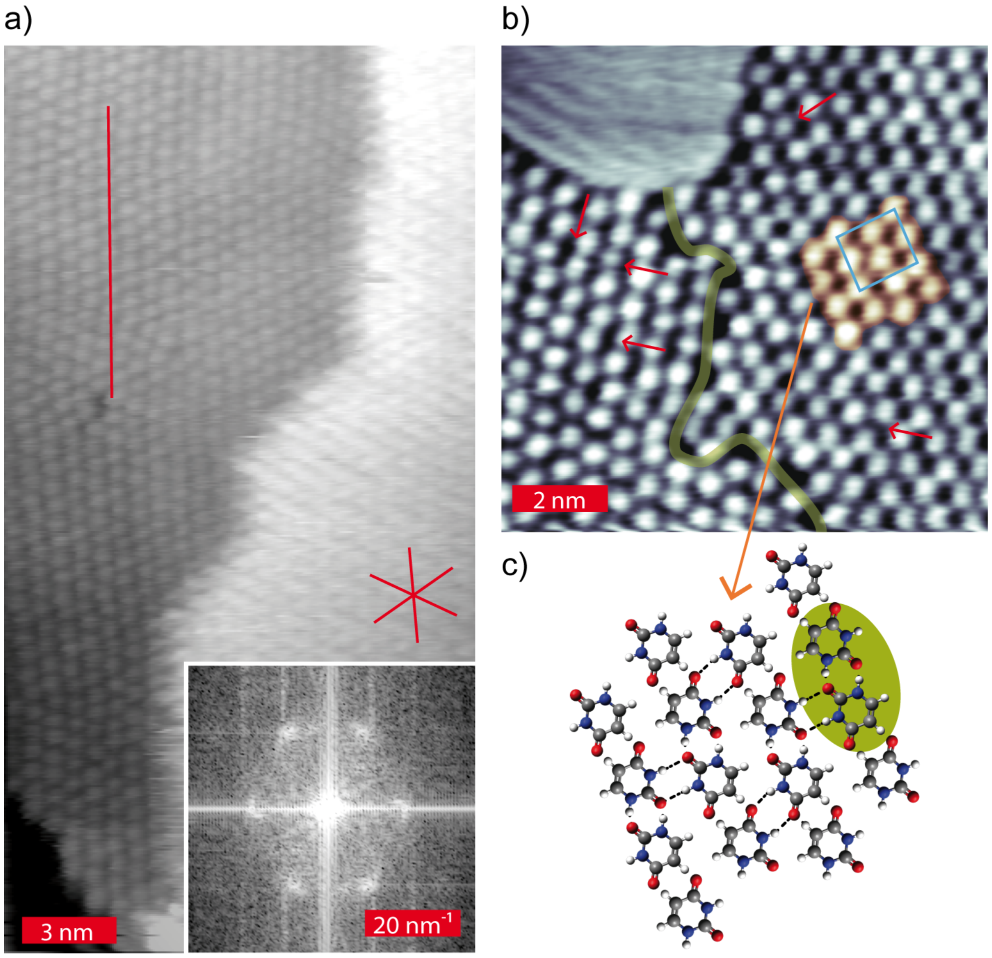

Figure 3.10: STM image of ∼ 0.3 ML of uracil on Ag(111): a) overview ($I_t = 120\,\text{pA}$, $U_t = 0.63\,\text{V}$); inset shows the corresponding FFT; b) detail with single-molecules resolution ($I_t = 110\,\text{pA}$, $U_t = 0.63\,\text{V}$) showing a boundary of two domains (green thick line) and the unit cell of the overlayer structure (in blue); c) tentative molecular model based on the most stable uracil homopairs (highlighted in green) for the orange highlighted area in b). Red marks and arrows indicate deviations from the molecular model proposed in c), and the Ag(111) high-symmetry axes are indicated in red.

peaks	E_B(eV)	assignment
A	284.7	C 1s → π^* (C5)
B	285.9	C 1s → π^* (C6)
B'	286.4	C 1s → π^* (C6)
C	288.0	C 1s → π^* (C4)
D	289.4	C 1s → π^* (C2)
D'	290.2	C 1s → π^* (C2)
E	293.5	C 1s → π^*
F	295.0	C 1s → σ^*
G	303.0	C 1s → σ^*

Table 3.2: Peak assignments for the C K-edge NEXAFS of 1 ML uracil on Ag(111). [116, 117].

observations can be seen in figure 3.10: although a model similar to the one proposed for uracil on graphite [102] can be fitted in small regions (figure 3.10c), the structure exhibits frequent irregularities, as indicated by the red marks.

X-ray spectroscopy:

Further XPS and NEXAFS characterization of this system confirms the interpretation of the STM data. Figure 3.11 summarizes the C 1s, N 1s, and O 1s XP spectra of uracil adsorbed in the temperature range of 300 to 330 K on Ag(111) and Cu(111). The central row shows the XP spectra corresponding to a monolayer of uracil on Ag(111). The C 1s region exhibits four clear peaks corresponding to the four carbon atoms of uracil, namely, in order of increasing binding energy, the atoms C5, C6, C4, and C4 (for the labeling of the uracil atoms see figure 3.9a) [113]. The N 1s region is characterized by a single peak (fwhm $\sim$ 1.3 eV) centered at a binding energy of 400.8 ± 0.1 eV. The O 1s core level also appears as a single broad peak at a binding energy of 532.0 ± 0.1 eV with fwhm of 1.5 eV, in good accord with amide [114]. Comparing the spectra with the corresponding ones of the multilayer of physisorbed uracil (figure 3.11 top spectra), it becomes evident that adsorption leads to an almost rigid shift of all six peaks by -0.5 eV. This shift is attributed to a polarization screening by the substrate and is typical for intact organic species on a metal substrate [115]. The uniformity of the shift is consistent with planar adsorption geometry with moderate metal–molecule interactions suggested by the STM data. In the multilayer regime, it is known that uracil is intact and in its canonical form, i.e. as the lactam tautomer [116]; thus the same conclusion holds for the present system: uracil adsorbs intact as a lactam species at the Ag(111) vacuum interface.

Figure 3.12a shows C K-edge NEXAFS data of 1 ML of uracil on Ag(111) at 300 K recorded at three photon incidence angles θ. The first four sharp resonances A to D correspond to transitions from C 1s to each of the first two available π^* orbitals, respectively.

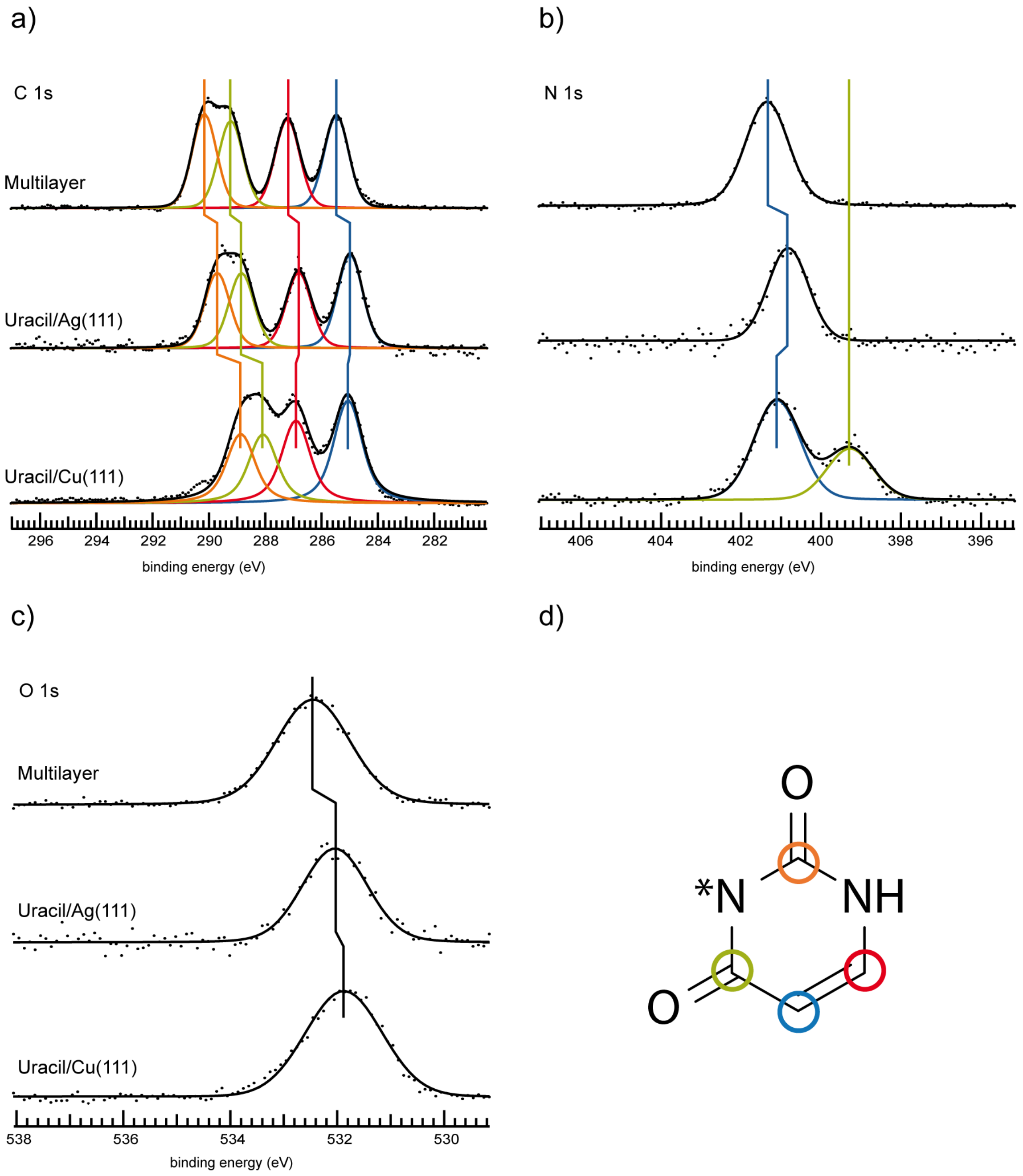

Figure 3.11: Uracil XP spectra corresponding to a multilayer formed at 300 K, a saturated monolayer on Ag(111) formed at 330 K and a saturated monolayer on Cu(111) formed at 320 K for the a) C 1s, b) N 1s and c) O 1s core levels. d) Structural formula of uracil with assignment of the signals from the C 1s spectrum to the different carbon atoms.

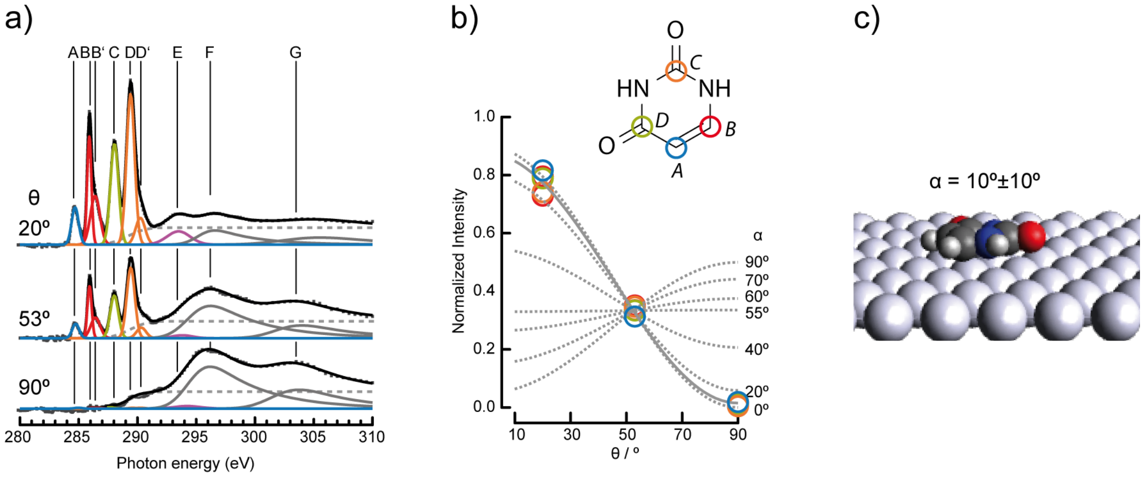

Figure 3.12: a) Experimental C K-edge NEXAFS data acquired at three angles of photon incidence, θ, for the 1 ML coverage of uracil on Ag(111) and respective fit analysis. b) Curve-fitting analysis of the photon angle dependence of π^* resonances A and D to estimate the corresponding molecule tilt angle, α. c) Illustration of adsorption geometry of uracil in the monolayer on Ag(111): the molecule tilt angle with respect to the surface is $\sim 10°$.

Resonance E exhibits an angular dependence following the π^* transitions; however it appears in a region where transitions cannot be clearly distinguished; two broad σ^* resonances F and G occur beyond the step edge of ionization (figure 3.12a, gray dashed lines). A summary of the assignments and associated transitions is given in table 3.2, based on the comparison with simulated NEXAFS [117] of the gas phase uracil molecule and experimental NEXAFS [116] of condensed uracil. As expected, both groups of π^* and σ^* resonances display distinct dichroism in their angular dependence.

Since the C atoms are approximately coplanar, the angular dependencies observed in the C K-edge spectra provide a powerful means of determining the orientation of uracil with respect to the surface. Figure 3.12b presents such an analysis for the principal π^* resonances A to D, the observed normalized intensities being overlaid with a best-fit theoretical curve (solid gray line) for the molecular tilt angle (α) with respect to the surface. (In principle, σ^* resonances may be subject to a similar analysis, but their larger width and the fact that they are superimposed on the step background preclude accurate fitting.) The normalized intensities of the π^* resonances fit very consistently a uracil tilt angle of 10°±10°, indicating that the molecule is lying almost flat on the surface (figure 3.12c).

The findings of this spectroscopic study are in line with the interpretation of the microscopy data. Perhaps the only discrepancy with earlier STM studies of uracil on inert surfaces, such as Ag(111) [109], Au(111) [107], and graphite [102], is that in this work at room temperature STM data shows that there is poor long-range order, with relatively small patches of different two-dimensional networks. This could either arise from differences in experimental conditions, as the present work was carried out under ultrahigh vacuum rather than at the solid-liquid interface, or be a consequence of the local nature of the STM technique, which samples a minute surface area.

3.2.2 Uracil on Cu(111)

The following section is split into three parts: The first two describe the experimentally observed chemical modifications of uracil in different temperature regimes, as it will be revealed by the subsequent XP spectra; the third addresses the aforementioned chemical modifications with *ab-initio* calculations.

From 300 to 360 K.

On the Cu(111) surface, structures completely unrelated to those formed on Ag(111) appear in the first layer. Deposition of $\sim$ 0.3 to 0.8 ML of uracil at room temperature on Cu(111) yielded a surface with a mixture of two phases, a "tiare" (figure 3.13) and a "zigzag" (figure 3.14) pattern imaged by STM at room temperature. The self-assembly of these phases is described before proceeding with the description of their dynamical interchange.

The tiare phase is a commensurate phase, as evidenced by the lack of any moiré pattern, and its rhombic unit cell (figure 3.13a) can be described in Wood's notation by a $9(\sqrt{3} \times \sqrt{3})R30°$ overlayer. This means that on the (111) surface there is only one symmetry domain. However, this is an intrinsically chiral phase, as evidenced by the S and R "petal" orientation of the tiare motif (figure 3.13b-c). As such, it is a rare example of a nondensely packed two-dimensional chiral phase of a nucleobase, other reported examples being guanine/Au(111) [118] and xanthine/Au(111) [119]. In the center of the tiare motif and in between the petals, features of high contrast are commonly observed (figure 3.13c), which are attributed to weakly bound diffusing molecules trapped in the tiare nanocages. The tiare phase was observed in an earlier study of uracil on Cu(111) at $\sim$ 77 K and described as "snow-crystal-like" [103], because in those STM images the chirality could not be resolved. In contrary to the previous study, the STM micrograph in figure 3.13 shows 30 distinct bright protrusions per unit cell versus the 18 reported earlier [103]. Each tiare flower consists of six pentamer petals. In that earlier study it was concluded that the bright protrusions correspond to single, intact molecules, their round shape and apparent height indicating flat-lying molecules and their separation be-

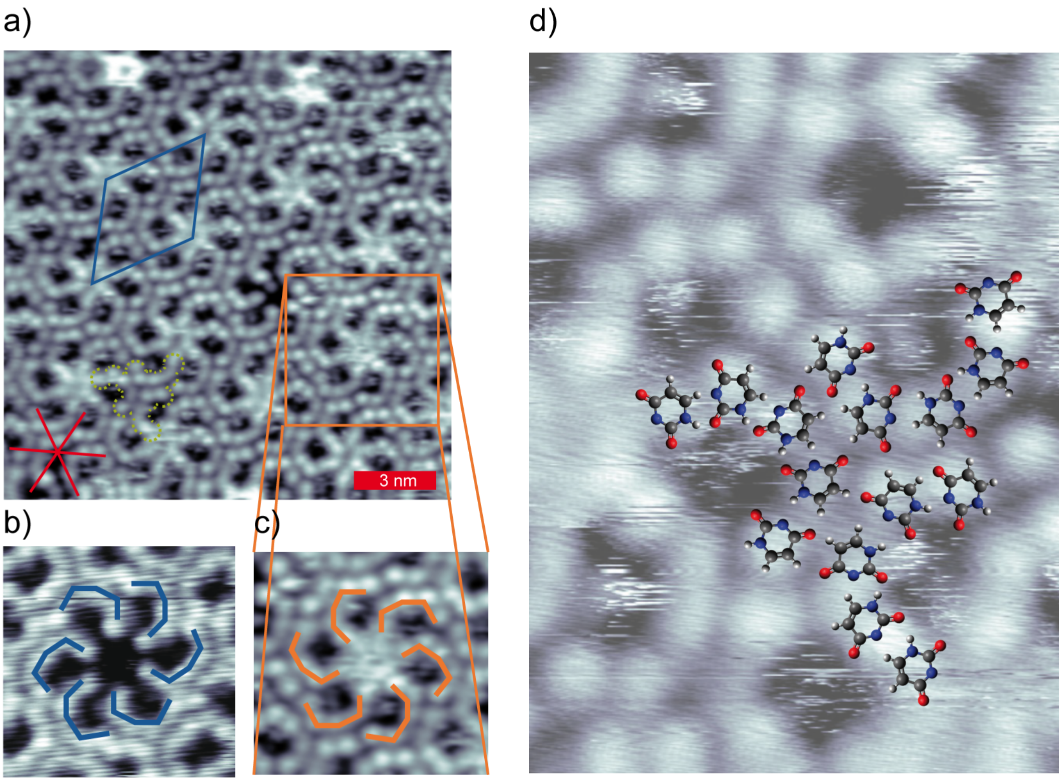

Figure 3.13: a) STM image of submonolayer coverage of uracil on Cu(111) at ∼ 300 K showing a domain of the tiare phase ($I_t = 130\,\text{pA}$, $U_t = 1.2\,\text{V}$). The Cu(111) high-symmetry axes are indicated in red and the superstructure's unit cell in blue. b) Tiare motif in STM images of an *S*-petalled domain ($I_t = 110\,\text{pA}$, $U_t = 0.857\,\text{V}$) and c) that of an *R*-petalled domain, indicated by the orange square in a). d) Tentative model of tiare phase, corresponding to an area indicated by the green dotted line in a) overlaid on the STM image.

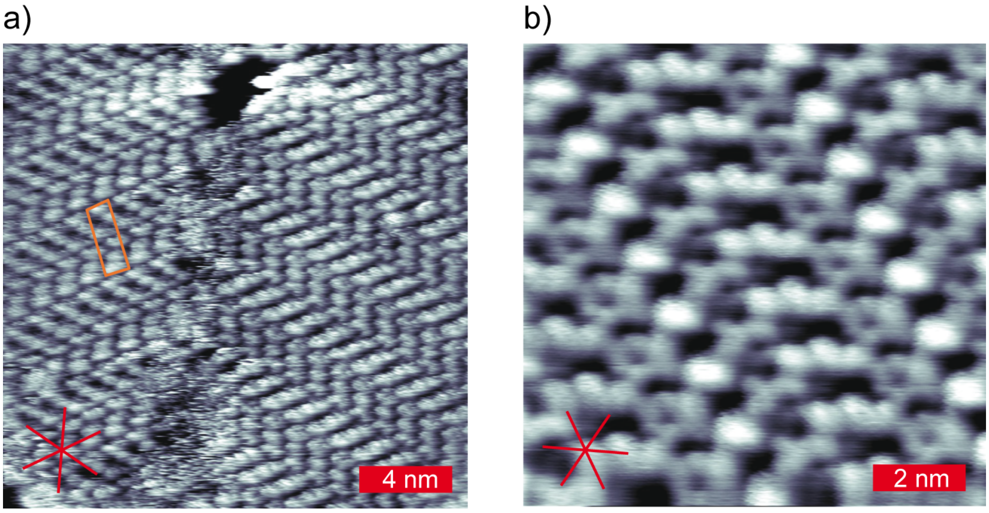

Figure 3.14: STM images of the "zigzag" phase of uracil on Cu(111) at ∼ 300 K showing a) overview (I_t = 110 pA, U_t = 0.857 V) and b) detail (I_t = 130 pA, U_t = 1.25 V. The Cu(111) high-symmetry axes are indicated in red and the superstructure's unit cell in orange.

ing consistent with hydrogen bonding. However, the proposed model [103] cannot be substantiated if 30 intact, flat-lying molecules per unit cell are assumed: the resulting molecular distances are, in fact, too small for such a model to be consistent.

In the zigzag phase the molecular density is even higher, the bright protrusions having oblong shapes. This suggests tilted molecules, which interact strongly with the underlying substrate. To understand the mixture of the phases, temperature- and coverage-dependent STM measurements were performed. It was found that the balance of the mixture is shifted with heating this surface to just 320 K: only the tiare phase is observed. The opposite effect in this balance comes from increasing the coverage to a saturated monolayer: only the zigzag phase was present after the preparation of a saturated monolayer. This implies that both of these phases must be made of the same molecular unit.

Looking at the 1s core level binding energies of the uracil's distinct atoms gives insight into their chemical state in order to identify the molecular unit. These spectra are displayed in figure 3.11 and show marked differences relative to the case of the Ag(111) substrate. Most prominent is the appearance of a new, additional peak in the N 1s level shifted in binding energy by ∼ -2 eV with respect to that of the intact protonated nitrogen, which is assigned to deprotonation of a single uracil nitrogen. This proton is not recaptured by the molecule: The O 1s core level does not show any significant change when compared to the multilayer of uracil, apart from the shift associated with the metal surface interaction. Furthermore, by close inspection of the C 1s core level the deproto-

peaks	**E_B(eV)**	**assignment**
A	284.9	C 1s → π^* (C5)
B	286.0	C 1s → π^* (C6)
B′	286.4	C 1s → π^* (C6)
C	287.9	C 1s → π^* (C4)
D	289.2	C 1s → π^* (C2)
E	292.1	C 1s → π^*
F	295.0	C 1s → σ^*
G	302.0	C 1s → σ^*

Table 3.3: Peak assignment for the C K-edge NEXAFS of 1 ML uracil on Cu(111) [116, 117].

nated N atom can be identified. The peaks originating from atoms C5 and C6 (marked in figure 3.11 by blue and red, respectively) are unaffected by the chemical transformation of the molecule, whereas peaks C4 and C2 (marked in figure 3.11 by green and orange, respectively) are both shifted downward by $\sim$ 1 eV, reflecting the rearrangement of electron distribution after the chemical change in the nearest neighboring N atom. Had it been a deprotonation of the N1 site, the chemical shift would be observed in the peaks corresponding to C2 and C6 atoms. Consequently, it is the N3 atom that undergoes deprotonation, as it is also the case for uracil and the closely related species, thymine, on the Cu(110) surface [77, 105] and in solution [120], but not in the gas phase, where the N1 atom is found to be more acidic [121]. However the authors of the last study argue also that the stability of $N3^-$ is enhanced in polar solvents, therefore tuning the deprotonation selectivity in a biological environment. Our study shows that in the case of metal-mediated deprotonation, it is the N3 site that undergoes preferential deprotonation.

From the previous considerations, it is clear that the tiare phase described above bears a nontrivial interaction with the underlying substrate: it consists of uracil molecules with the N3 atom deprotonated, and hence there is a need to establish an atomistic structural model of this phase. Given that the STM indeed shows roundish protrusions, similar in shape to uracil/Ag(111), flat-lying molecules can be assumed and a tentative model is proposed in figure 3.13d. It is a structure consisting of homochiral pentamer "petals", repeated with 6-fold symmetry (as dictated by the substrate symmetry) to generate a "tiare" motif. The resulting molecular structure is stabilized by hydrogen bonding, N-H$\cdots$O=C, and additional lateral interactions involving, N^-, C-H, and C=O groups at the pentamer and C-H and C=O moieties between neighboring pentamers. Uracil is an achiral molecule in the gas phase; however its reduced symmetry turns it into chiral once confined on a two-dimensional plane. It is noteworthy that in the model proposed above the two chiral domains consist of enantiopure uracil monomers deprotonated at N3.

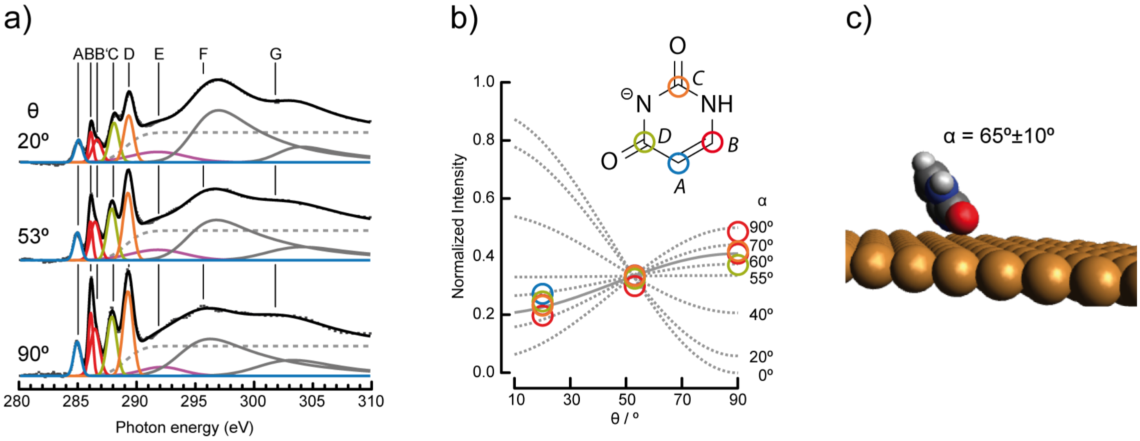

Figure 3.15: a) Experimental C K-edge NEXAFS data acquired at three angles of photon incidence, θ, for the 1 ML coverage of uracil on Cu(111) and respective fit analysis. b) Curve-fitting analysis of the photon angle dependence of π^*resonances A to D to estimate the corresponding molecule tilt angle, α. c) Illustration ofn the adsorption geometry of uracil in the monolayer on Cu(111): the molecule tilt angle with respect to the surface is $\sim 65°$.

The STM images of the zigzag phase, on the other hand, suggest a strongly tilted molecule. Indeed, this is in accordance with NEXAFS measurements on the saturated monolayer, which consists only of this phase. Figure 3.15a shows the corresponding NEXAFS data at three angles of photon incidence. The resonances observed are assigned in table 3.3. From the curve-fitting analysis of the photon angle dependence of π^* resonances A to D (figure 3.15b), the molecule tilt angle of the zigzag phase is estimated to be $\sim 65°$ (figure 3.15c).

By close inspection of the zigzag phase it can be noticed that the longer axis of the molecular elliptical shapes aligns along the high-symmetry axes. This is consistent with PhD measurements, a powerful technique for accurate determination of the adsorbate geometry, of uracil and the similar DNA base, thymine, on Cu(110) [77, 105]. Both molecules are found to bind along the close-packed direction of Cu. The close match of the O-N$^-$-O projected distances presumably drives the binding to the Cu atoms of the close-packed rows along the $\langle 1\bar{1}0 \rangle$ direction. Figure 3.14b reveals also features of different contrast in STM data; therefore it is plausible that molecules with different adsorption geometries are present. From the NEXAFS measurements the average tilt of the molecular ensemble is determined to be $\sim 65°$; therefore, it is concluded that this phase consists *mainly* of strongly inclined molecules.

At the temperature of formation the presence of diffusing Cu adatoms is known to play an important role in the deprotonation and surface coordination of compounds with car-

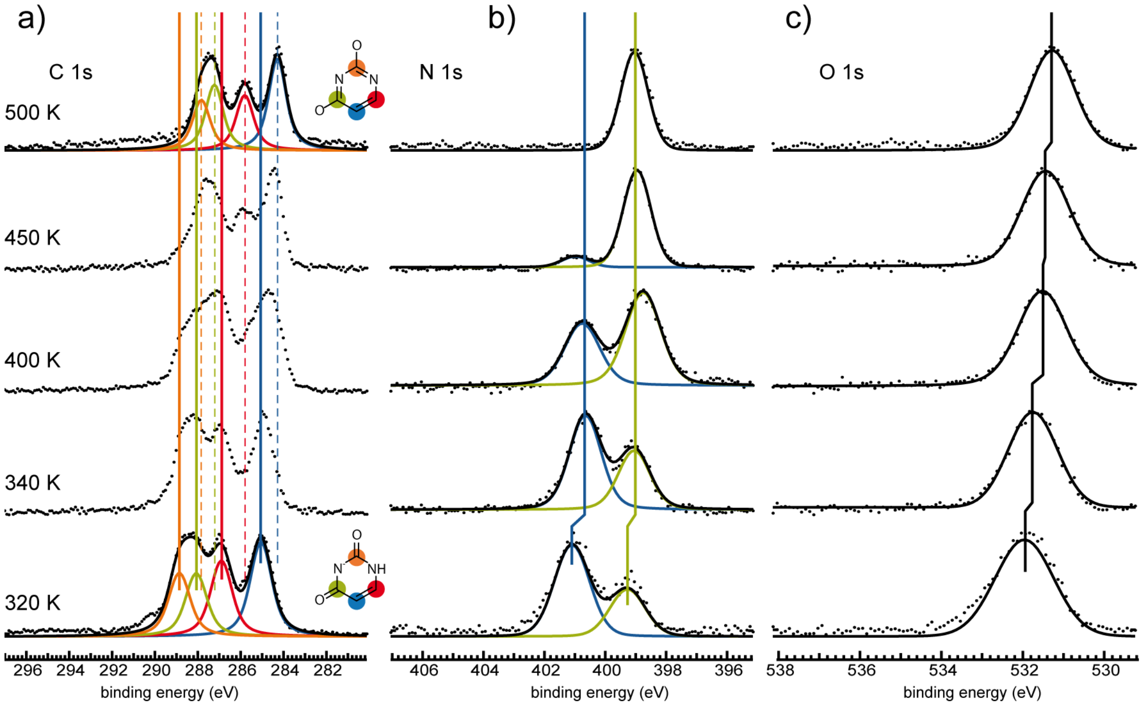

Figure 3.16: Uracil XP spectra of a) C 1s, b) N 1s and c) O 1s core levels corresponding to a saturated monolayer on Cu(111) as a function of annealing temperature. Solid and dotted lines mark the binding energies of the molecules of a layer formed at 320 K and after annealing to 500 K, respectively.

boxylic acid moieties [122, 123] and in the surface coordination and adsorption of compounds containing pyridyl groups [124–126]. In the phases described above there is no direct evidence for their involvement in the structure. In the tiare phase the intermolecular distance is too short to allow the incorporation of metal adatoms. In the zigzag phase, the molecules have a high tilt angle, allowing uracil molecules to coordinate with both oxygen atoms and the deprotonated N3 toward the surface, as also supported by the DFT results presented below. However, it is possible that undercoordinated adatoms are important in activating the N-H scission observed [127].

From 400 to 550 K

Heating the uracil monolayer on Cu(111) to higher temperatures and monitoring the N 1s signal (figure 3.16b), one can primarily observe the increase of the deprotonated N signal along with a concomitant decrease in the molecular coverage. By 500 K only deprotonated N is present, while a shift of -0.8 eV is observed in the O 1s signal (figure 3.16c) and the C 1s shows a significant charge redistribution (figure 3.16a). Clearly, the uracil

assignment	**singly deprotonated uracil (320 K)**		**doubly deprotonated uracil (500 K)**	
	exper. (eV)	**DFT (eV)**	**exper. (eV)**	**DFT (eV)**
C2	288.9	297.5	287.8 (- 1.1)	296.4 (- 1.1)
C4	288.1	296.2	287.2 (- 0.9)	296.0 (- 0.2)
C6	286.9	295.0	285.8 (- 1.1)	294.4 (- 0.6)
C5	285.1	293.9	284.3 (- 0.8)	293.1 (- 0.8)
N1	401.1	412.0	399.0 (- 2.1)	408.8 (- 3.2)
N3	399.3	410.1	399.0 (-0.3)	409.6 (- 0.5)
O1	531.9	543.5	531.1 (- 0.8)	542.6 (- 0.9)
O2	531.9	543.1	531.1 (- 0.8)	542.8 (- 0.3)

Table 3.4: Peak assignment for the XPS signals corresponding to a saturated monolayer formed at 320 K on Cu(111) (singly deprotonated) and 500 K (double deprotonated) and the related calculated binding energies from DFT. The relative shifts with respect to the binding energies of the singly deprotonated uracil are given in parenthesis in the columns referring to the doubly deprotonate uracil.

molecules after this heat treatment are doubly deprotonated and the spectroscopy data are comparable to the case of uracil on Cu(110) [105].

However, unlike the topography of uracil on Cu(110) after annealing to 400 K [128], no adsorption-induced surface faceting was observed on Cu(111). The corresponding topography observed by the STM investigation is shown in figure 3.17. Trilobed structures, oriented along the $\langle\bar{2}11\rangle$ direction of Cu(111), appear among less ordered mobile molecules and are stable on the surface after heating in the range from 400 to 550 K. In the trilobed structures (figure 3.17b) elliptically shaped protrusions corresponding to the lateral dimensions of tilted single molecules are discernible. Their separation along the $\langle\bar{2}11\rangle$ Cu(111) direction is $\sim$ 4.5-4.7 Å, whereas that along the close-packed $\langle 1\bar{1}0\rangle$ is $\sim$ 6 Å, supporting that the trilobed structures consist of tilted molecules in a similar local adsorption geometry to that in the zigzag phase (figure 3.14b).

Indeed the corresponding angular dependence of NEXAFS reveals an average tilt angle of $\sim 60°$ (figure 3.18). However it is striking that the doubly deprotonated uracil forms close-packed structures, such as the ones of the trilobe. Intuitively, the formation of such dense packing can be rationalized with charge transfer from the substrate metal. But having a tilted uracil molecule means that both nitrogen atoms cannot be in close contact with the metal surface. Hence most probably the electron charge is relocalized on the uracil oxygen atoms, both of which can be in close contact with the surface.

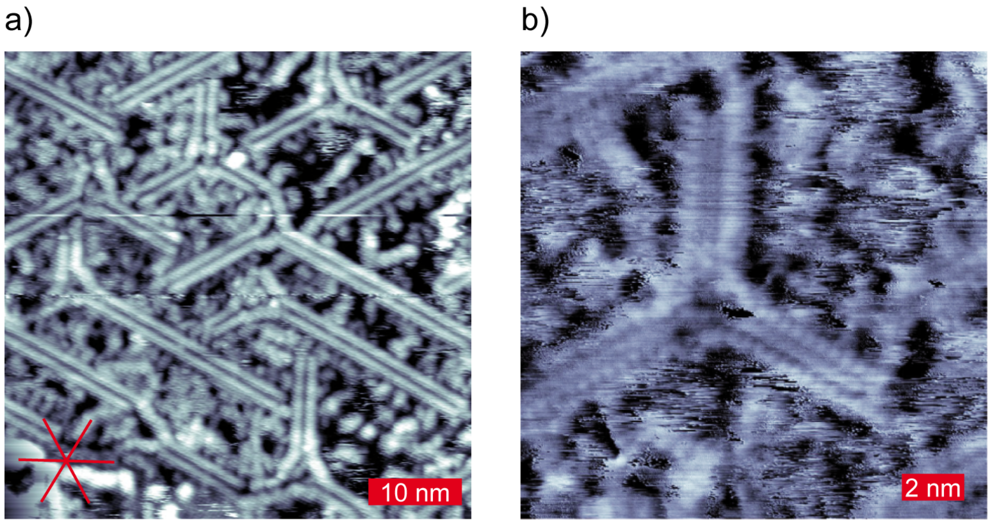

Figure 3.17: STM images of 1 ML of the trilobed structure (uracil on Cu(111) after heating to 500 K): a) overview ($I_t = 290\,\mathrm{pA}$, $U_t = 2.9\,\mathrm{V}$)and b) detail ($I_t = 140\,\mathrm{pA}$, $U_t = 1.25\,\mathrm{V}$). The substrate high-symmetry axes are indicated in red.

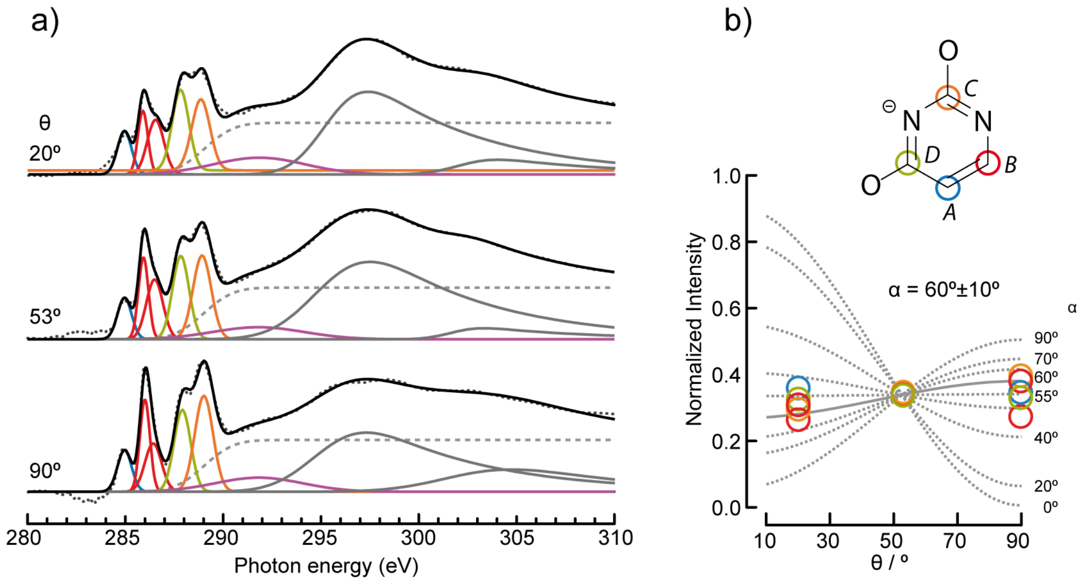

Figure 3.18: a) Experimental C K-edge NEXAFS data acquired at three angles of photon incidence, θ, for the 1 ML coverage of uracil on Cu(111) formed at 320 K and postannealed to 500 K, and respective fit analysis. b) Curve-fitting analysis of the photon angle dependence of π^*resonances shown in a) to estimate the corresponding average molecule tilt angle, $\alpha \sim 60°$.

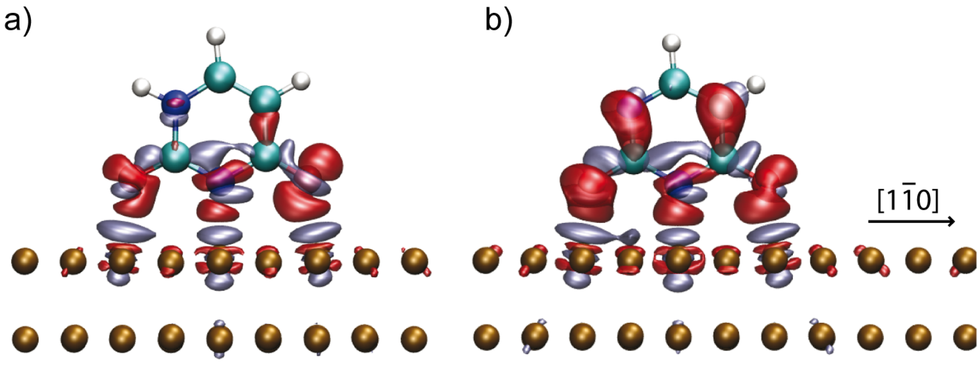

Figure 3.19: Three-dimensional representation of the electron density differences of a) a singly and b) a doubly deprotonated uracil molecule on Cu(111) from the electron density of the corresponding uracil radical and the pristine Cu(111) surface. Red and blue regions indicate areas of gain and loss of electrons, respectively.

DFT Modeling[1]

In order to get deeper insight into the uracil surface chemical bonding and electronic structure, DFT calculations of singly and doubly deprotonated single uracil molecules on Cu(111) were performed. From these, the binding energies of the C 1s, N 1s, and O 1s core levels were computed (Table 3.4). The good agreement obtained in the relative shifts between experimentally measured and theoretically calculated core levels supports the approximation of the ensemble of adsorbed uracil molecules with an isolated molecules as well as the interpretation of the XPS data.

Figure 3.19 shows the corresponding fully relaxed adsorption geometries superimposed on the electron density differences between the adsorbed molecule on the Cu(111) and the corresponding uracil radical and the pristine Cu(111) surface; for a one-dimensional charge difference averaged along the surface plane see figure 3.20. As for the case of uracil [105] and thymine [77] on Cu(110), the deprotonated uracil is coordinatively anchored upright along the Cu closed-packed direction in a tridentate configuration. The smaller tilt angles derived by the NEXAFS analysis reported above originate presumably from the intermolecular interactions in the self-assembled structures and/or because of the coexistence of different local adsorption modes. The binding energies of these configurations are given by $E_{\text{bind}} = -(E_{\text{uracil/Cu}} - E_{\text{uracil}} - E_{\text{Cu}})$, where "uracil" here refers to the uracil radical, and are 3.433 and 4.438 eV for the singly and doubly deprotonated molecules, respectively. The electron density differences of the adsorbed uracil from the radical molecules (figure 3.19) in both cases exhibit significant charge redistribution upon

---

[1] The DFT Modeling was performed by Ari P. Seitsonen. DFT calculation details are published in [129].

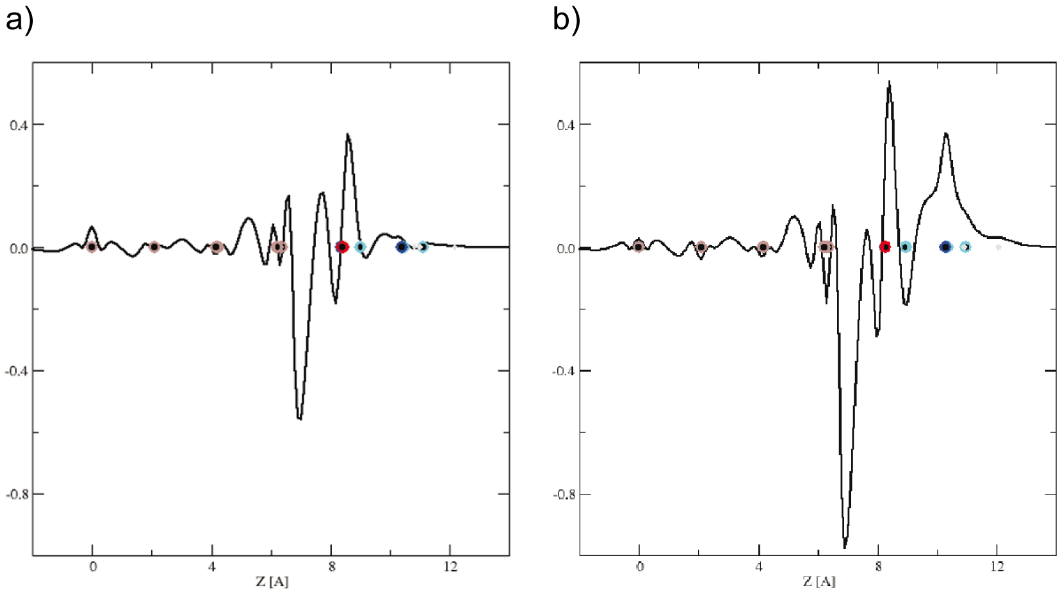

Figure 3.20: One-dimensional representation of the electron charge difference averaged along the surface plane of a) a singly and b) a doubly deprotonated uracil molecule on Cu(111) from the electron density of the corresponding uracil radical and the pristine Cu(111) surface. The positions of Cu, O, C, N, and H atoms are marked with brown, red, light blue, dark blue, and gray circles, respectively. The y-axis shows distance along the Cu $\langle 111 \rangle$ direction in Å.

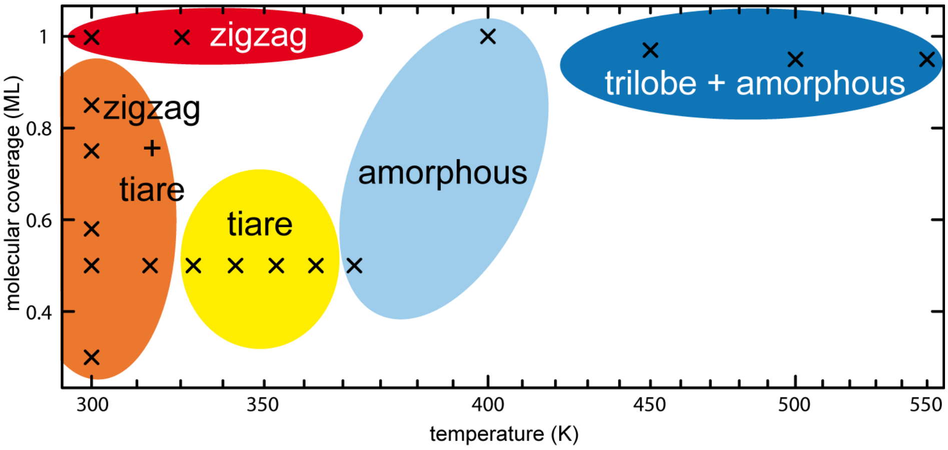

Figure 3.21: Schematic overview of the overlayer structures formed by uracil on Cu(111) as a function of coverage and annealing temperature.

adsorption, with a gain of electrons (red regions) and loss of them (blue) in several regions. Moreover, the substrate atoms seem to gain negative charge in the d_{xz} and d_{yz} orbitals when the molecule is adsorbed and lose from the d_{z^2} orbitals. The Bader analysis gives a charge transfer of 0.6 electron to the molecules in the configuration shown in figure 3.19a (deprotonated at N3) and 1.1 electrons in the configuration shown in figure 3.19b (deprotonated at both N1 and N3).

Such a scenario of electron charge shifting can actually help interpret earlier reflection absorption infrared spectroscopy (RAIRS) results of thymine on Cu(110) [130], which showed that the C=O vibrational mode disappeared after annealing at 558 K, indicative of the formation of strong bonds to surface atoms. The PhD study of the same system revealed that thymine preserves its tridentate adsorption geometry upon annealing and creates doubly deprotonated thymine molecules.[77] Moreover, PhD investigations of both uracil and thymine on Cu(110) found the O-Cu distances to be comparable with the typical O-Cu distances of acetate species on the same surface, further supporting the formation of molecular bonds between O and Cu [77, 105].

3.2.3 Summary and conclusion

A detailed study of the first molecular layer of uracil on close-packed noble metal surfaces was performed, using state-of-the-art STM, synchrotron XPS, and NEXAFS coupled with DFT, which provides a deep understanding of these systems. On Ag(111) uracil adsorbs almost flat, intact, and forms a densely packed hydrogen-bonded network with poor long-range order. This is contrasted by the behavior on Cu(111), where uracil deprotonates at the N3 site upon adsorption at room temperature. Two different phases are revealed depending on the local density of uracil. A tiare phase, which prevails at low coverages where the presence of bare Cu patches facilitate molecular diffusion, consists of flat-lying monomers, thus maximizing the interaction of the π orbitals of the molecule with the metal surface. As the coverage increases, the molecule tilts with respect to the surface with an average tilt angle of $\sim$65°, accommodating a more dense layer in contact with the Cu surface. By heating the saturated monolayer uracil film on Cu(111) to 500 K, also the N1 atom deprotonates, and a new type of trilobed nanostructure forms. A schematic overview of the overlayer structures found is depicted in figure 3.21.

Similarly to the different behavior of methionine on Ag(111) [46] and on Cu(111) [45], the importance of the subtle increase in substrate reactivity in tailoring the resulting nanoarchitectures was demonstrated. Among the phases formed, a tiare phase forming chiral nanocages was observed, which additionally feature reactive sites in their inner periphery, thus making this phase suitable for exploitation as a molecular recognition template. Finally, the gradual deprotonation of the uracil nitrogen atoms and the occurring charge redistribution within the molecule was addressed, providing a coherent description of the uracil interaction with the metal surface. These chemical transformations are of relevance in the biological environments, tuning the interaction selectivity of particular sites of uracil.

3.3 Orotic acid on Ag(111) and Cu(111): Self-assembly and chemical behavior

Orotic acid, also known as 6-carboxyuracil (figure 3.22) is an important derivative of the RNA base uracil, addressed previously in section 3.2. It is a basic educt for the formation of uridine monophosphate, the most important intermediate in the *de-novo* synthesis pathway, i.e. the synthesis from simple molecules such as sugars or amino acids, of pyrimidine nucleobases such as thymine, uracil and cytosine [131]. Similarly to other pyrimidine bases, it undergoes a lactim-lactam tautomerization with the lactam form (shown in figure 3.22b) being the energetically favored and hence the most commonly occurring one. However it has been shown that by the interaction of these functionalities with solid surfaces the preferential molecular configuration can differ from the lactam tautomer. For example an experimental study revealed that uracil adsorbs in its lactim form on the Si(100)-2 $\times$ 1 [104], whereas a DFT study of uracil on Au(100) [110] shows the enol with N3 deprotonated and O7 protonated (for labeling of the uracil atoms, see figure 3.9) as the most stable surface tautomer. Besides the different tautomer forms, orotic acid exists in two rotameric conformations resulting from the rotation of the carboxy group where the anti-conformation is slightly more stable [132]. On the surface, the carboxy group's proton is expected to transform freely from one oxygen to the other leading to unhindered transformations between the syn- and the anti-conformation [133, 134]. In combination with the molecules prochirality this results in four different conformations for each tautomer when adsorbed on the surface (figure 3.23). The rich array of possible chemical and structural conformations outlined above renders orotic acid a promising candidate for biofunctionalization and biological surface reactions as well as to deepen the understanding of hydrogen bonded networks of biomolecules. Biofunctionalization of well-defined surfaces has attracted attention in recent years because of their use in biocompatible surfaces [5, 135, 136], biomimetic engineering [137] as well as selective metallization templates [138]. Therefore, specific chemical reactions of surface anchored molecules came into focus, as they allow distinct tailoring of the surface chemical properties [139–141]. Despite the multitude of studies that have focused on the adsorption behavior and reactivity of many amino acids (e.g. [13, 44–46, 71, 93, 142, 143] and section 3.1) as building blocks of proteins and of DNA/RNA nucleobases (e.g. [113, 129, 144] and section 3.2), their precursor molecules or derivatives present a relatively unexplored playground. Moreover, the investigation of hydrogen bonded networks and the understanding of the influence of substituents is crucial for gaining knowledge of the intermolecular interactions which control and tailor biomimetic bottom-up nanoarchitectures, as hydrogen bonds and hydrogen transfer are primary for biological self-assembly processes and evolution [145].

The present work of orotic acid on coinage metal surfaces is an extension of the study on the adsorption and self-assembly of uracil (section, 3.2) and thymine [144]. The carboxy group differentiating orotic acid from uracil could partly prohibit the intermolecular interactions due to steric hindrance but simultaneously represents another functional group which is able to contribute in the formation of hydrogen bonds or metal coordination. A previous study has examined the effect of having an additional methyl group on uracil by looking into the DNA base thymine (5-methyluracil) on Cu(111) [144] where STM data showed only disordered patches at ∼ 80 K, while uracil forms extended, periodic two dimensional structures at equal conditions [103].

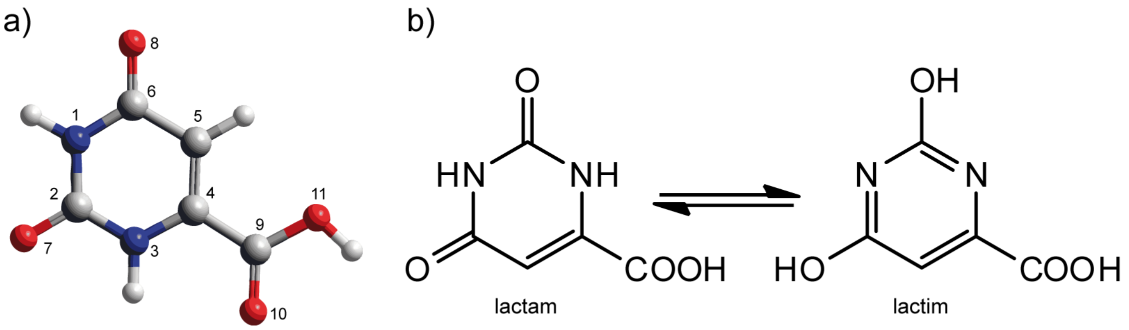

Figure 3.22: Orotic acid: a) Ball-and-stick model of orotic acid showing the labels of the constituent atoms and b) structural formulas showing the most common lactam and lactim tautomers.

The here presented comparative study focuses on the self-assembled structures and the chemical behavior as a function of heat treatment and coverage of orotic acid on the hexagonal Ag(111) and Cu(111) surfaces. Strong intermolecular interactions allow the formation of two coexisting structures on the silver surface, comprised of molecules in the lactam form. In contrast, the chemical state of the molecules on the copper substrate is strongly dependent on the temperature and the packing density. The STM investigation reveals a single transient periodic structure within a "sea" of diffusing monomers at room temperature at a given coverage. Freezing the molecular motion at 210 K shows molecular islands which lack identifiable periodic motifs. The comparison with uracil (section 3.2) studied under equal conditions gives insight in the influence of the carboxy substituent on self-assembly and chemical reactivity.

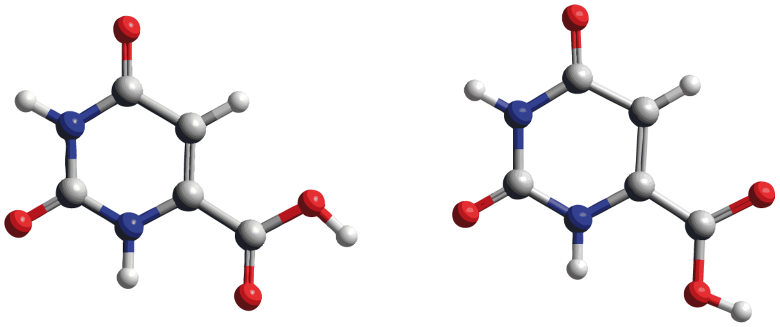

α-anti α-syn

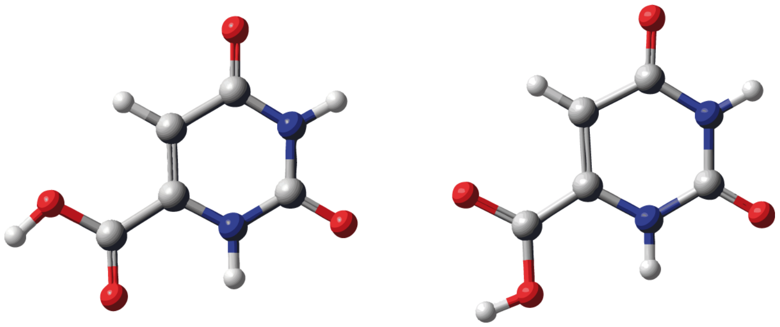

δ-anti δ-syn

Figure 3.23: Orotic acid featuring four different planar adsorption geometries. The α and δ conformation refers to the two faces of the prochiral orotic acid molecule, *syn* and *anti* refers to the different rotamer conformations resulting from rotation of the carboxy substituent.

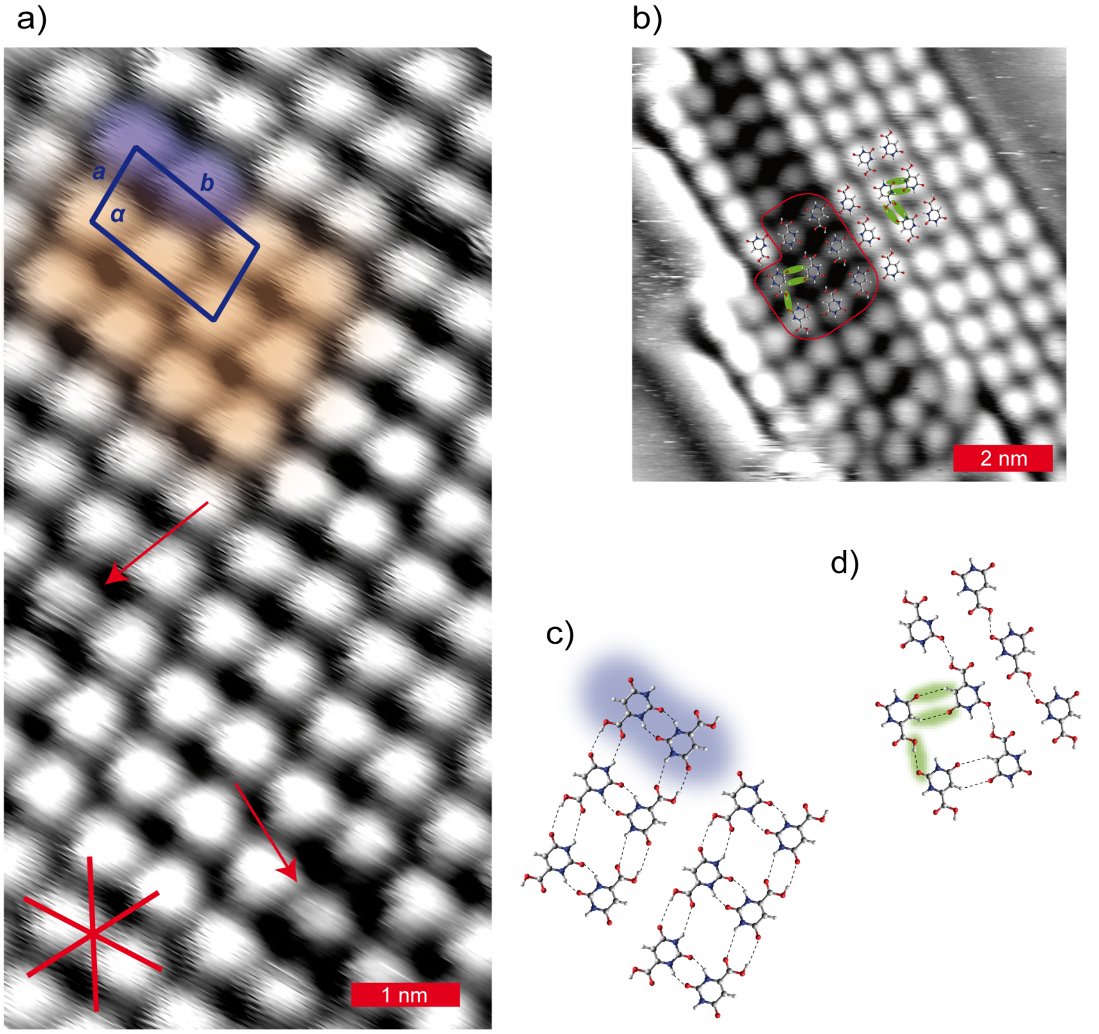

Figure 3.24: STM images and molecular model of orotic acid adsorbed on Ag(111). a) Molecular resolution of the close-packed phase. The structure's unit cell and the Ag(111) high symmetry axes are shown in blue and red, respectively. Arrows indicate molecules with lower apparent height. ($I_t = 110\,\text{pA}$, $U_t = 0.13\,\text{V}$). b) Different area of the close packed phase where a part of the molecular ensemble has lower apparent height. ($I_t = 110\,\text{pA}$, $U_t = 0.58\,\text{V}$). A molecular model consisting solely of α-anti molecules is superimposed onto the STM images, with the intermolecular interaction motifs highlighted in green. A different molecular model comprising "flipped" molecules in δ-anti conformation is framed in red and accounts for the deviation from the dimer-phase. c) Molecular model of the area highlighted in color in a), the single dimer is indicated in blue in a) and c). d) Magnification of the area framed in red in b). Dotted lines indicate the intermolecular hydrogen bonds in c) and d).

3.3.1 Orotic acid on Ag(111)

STM:

Focusing on the investigation of the intermolecular interaction of orotic acid molecules adsorbed on a metal surface, the chemical chemical inert and close packed Ag(111) surface is the substrate of choice as it is allowing the diffusion of adsorbates which facilitates the self-assembly and does not thermally activate the molecular adsorbate's moieties at room temperature (section 3.2.1). STM imaging revealed two different phases forming at room temperature and after annealing to temperatures up to 370 K independent of the surface coverage. The molecules assemble into islands which nucleate at the step edges. A minority phase with a nanoporous paddle wheel structure (described below) and a majority phase consisting of rows of molecular dimers close packed into two dimensional islands (referred to as "close-packed phase" hereafter). The dimer rows run along the $\langle 1\bar{2}1 \rangle$ directions. The close packed phase is characterized by a rhomboidal unit cell with $a = 8.1 \pm 0.5$ Å, $b = 13.7 \pm 0.4$ Å and an angle of $\alpha = 95°$ between them (figure 3.24a). It incorporates two molecules which have intermolecular separations consistent with flat-lying hydrogen bonded molecules. This close-packed structure shows a distinct similarity to the dense packed structure observed for uracil adsorbed on the Ag(111) substrate (see subsection 3.2.1 and figure 3.10). It is possible to fit a molecular model consisting of dimers from two molecules in α-anti conformation, whose bonding scheme is analogous to the most stable dimers of thymine and uracil calculated by DFT [111] (figure 3.24c), with the formation of two N3-H$\cdots$O10 hydrogen bonds. The N3/O10 binding site was also shown to form the most stable hydrogen bonds with a water molecule [146]. The bond length between the N and O atoms involved in this hydrogen bond is measured to be $\sim$ 2.8 Å from the molecular models superimposed into the STM data and is consistent with the reported values of the uracil and thymine dimers [111]. The dimers extend into rows by N-H$\cdots$O and O-H$\cdots$O hydrogen bonds. Occasionally, the structure shows single molecules with a lower apparent height by 0.26 Å with respect to the surrounding molecules (indicated by red arrows in figure 3.24a). These can most likely be attributed to either defects in the chemical structure of the molecule or to structural defects, e.g. the carboxylic moiety in a syn conformation or the presence of the both surface enantiomers α and δ (figure 3.23) amplified by tunneling through an asymmetric tip [147]. Some of the islands have larger areas with lower apparent height (figure 3.24b) featuring a unit cell with similar shape but mirrored with respect to a. A careful analysis of these areas reveals an apparent height decrease of 0.5 Å with respect to the molecules appearing brighter and molecular distances which are uniformly increased by 4 %. Despite discrimination between two different surface enantiomers (figure 3.23) due to an asymmetric tip, the lower apparent height in these areas can also be explained by a decreased electronic interaction between neighboring molecules. While the brighter regions can be well fitted with the model explained above, it is not possible to fit the areas appearing darker with a similar model comprising molecules in δ conformation. Instead, the molecular model which can be best fitted here involves fewer and weaker hydrogen bonds (highlighted in green in figure 3.24b), namely C5-H$\cdots$O8 and O11-H$\cdots$O10 interactions.

A nanoporous paddle wheel phase can be observed additionally to the close-packed phase on the silver substrate, representing a minority phase characterized by a $7(\sqrt{3} \times \sqrt{3})R30°$ unit cell (figure 3.25a). The structure can be described as paddle wheels consisting of a ring of six molecules (highlighted in blue in figure 3.25c-d), each of the molecules connected to a molecular dimer ("paddle", highlighted in orange in figure 3.25c-d) in close proximity to the dimer paddle of a neighboring wheel. The slight rotation of the axis connecting the two molecules of the dimer with respect to the normal of the unit cell axes results in the chiral arrangement of the paddles leading to the formation of extended domains of *(S)*-paddle wheels (figure 3.25c) or *(R)*-paddle wheels (figure 3.25d). The paddle wheel phase can be modeled (figure 3.25b and e) by a ring of six molecules linked by a head-to-tail N1-H$\cdots$O10 hydrogen bonds and six paddles, consisting of a dimers linked by a similar hydrogen bond. The dimers in the paddles are connected to the inner ring by an interaction of the ring's N3 and the paddle's carboxylic oxygen O10. The here employed dimer binding motif is stabilized by two N-H$\cdots$O hydrogen bonds but differs from the one shown for the close packed phase (figure 3.24c), as the aforementioned does not fit the smaller intermolecular distances between two dimers due to the steric hindrance of the carboxylic group. This structure which is not comprised solely of dimers demonstrates the point made earlier in section 3.2.1, that for a molecule with several functional groups able to form hydrogen bonds, the self-assembly is not solely driven by the stability of the dimers but additional interaction with neighboring molecules need to be taken into account. The cavity in the center of the six-membered ring is occasionally filled by an additional trapped molecule as exemplified in figure 3.25d.

X-ray spectroscopy:

In order to get insight into the chemical state of orotic acid in contact with the silver substrate and to verify the suggested models, XPS measurements were performed, while angle resolved NEXAFS spectroscopy revealed the orientation of the molecule with respect to the underlying substrate. The C 1s spectrum of a high submonolayer coverage ($\sim$ 0.8 ML) of orotic acid on Ag(111) can be clearly fitted with five signals of approximately equal intensities (figure 3.26a, middle), attributed with decreasing binding energy to the carbon atoms C2 and C9, C6, C4 and C5 (for binding energy and peak assignment

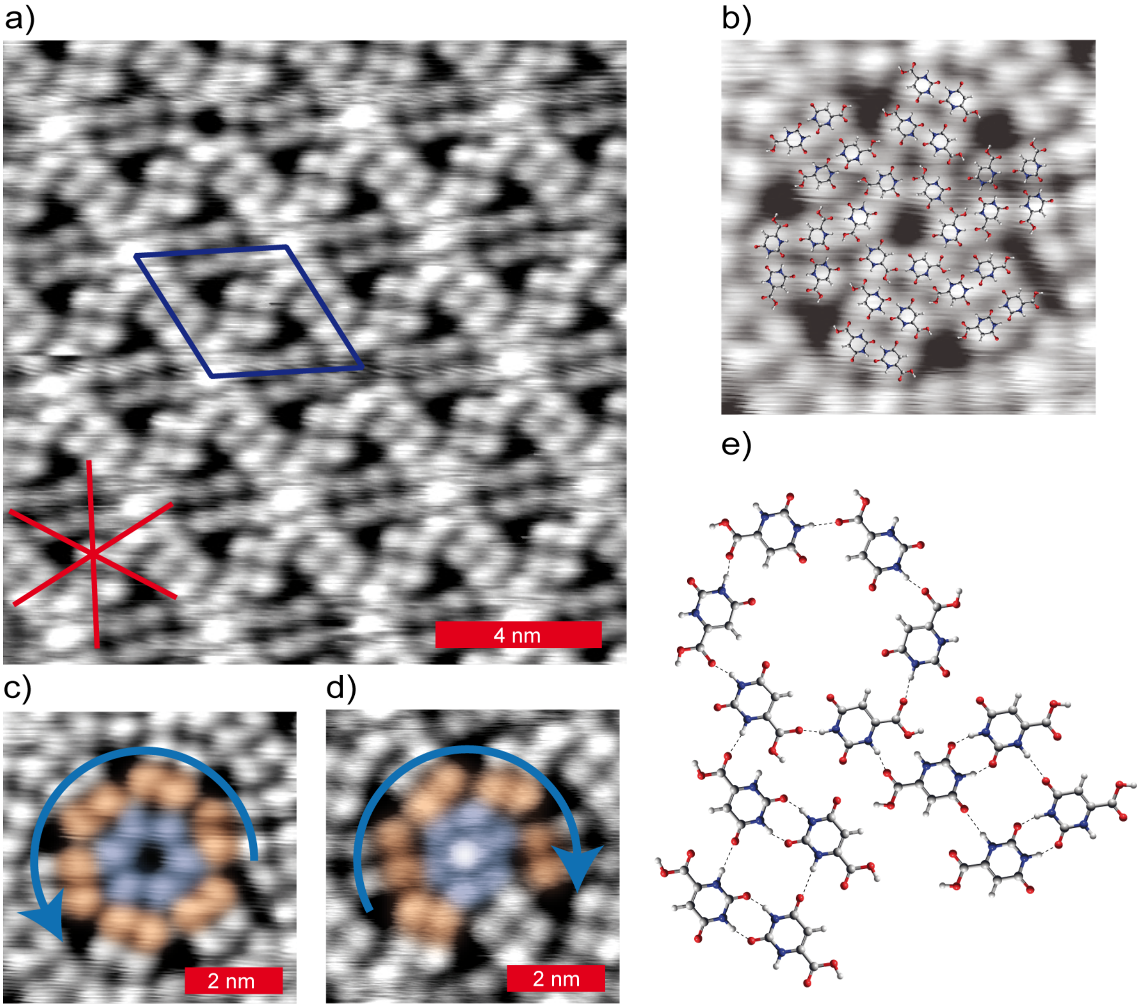

Figure 3.25: STM micrographs showing the "paddle-wheel" structures of orotic acid on Ag(111). a) Paddle wheel structure featuring a hexagonal unit cell ($I_t = 130\,\text{pA}$, $U_t = 1.25\,\text{V}$). The high symmetry directions of the Ag(111) substrate and the overlayer unit cell are indicated in red and blue, respectively. b) Molecular model for a single paddle wheel ($I_t = 120\,\text{pA}$, $U_t = 1.25\,\text{V}$). c-d) Visualization of the chirality of the paddle wheels, featuring c) an *(S)*-paddle wheel ($I_t = 120\,\text{pA}$, $U_t = 1.25\,\text{V}$) and d) an *(R)*-paddle wheel. ($I_t = 130\,\text{pA}$, $U_t = 1.25\,\text{V}$). e) Magnification of the molecular model fitting the paddle wheel structure.

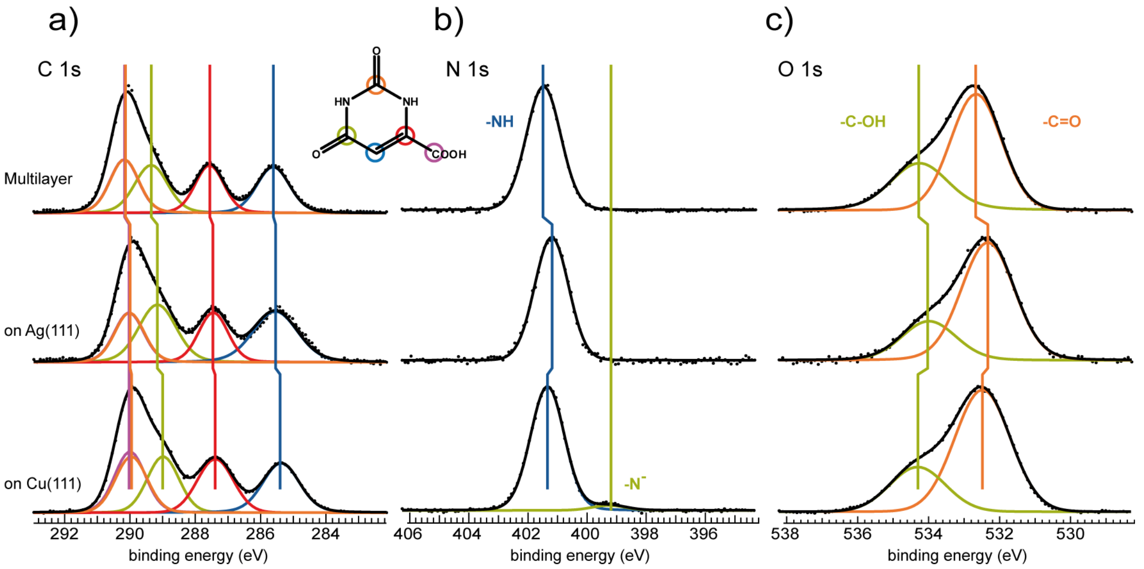

Figure 3.26: Orotic acid XP spectra corresponding to a multilayer of orotic acid (top) and a high submonolayer coverage ($\sim$ 0.8 ML) on Ag(111) (middle) and on Cu(111) (bottom) for the a) C 1s, b) N 1s and c) O 1s core levels.

assignment	multilayer binding energy (eV)	on Ag(111) binding energy (eV)	on Cu(111) binding energy (eV)
C2	290.2	290.0	290.0
C4	287.6	287.4	287.4
C5	285.6	285.5	285.4
C6	289.3	289.2	289.0
C9	290.2	290.0	290.0

Table 3.5: Peak assignment of the C 1s spectrum of an orotic acid multilayer and a high submonolayer coverage adsorbed on the Ag(111) and Cu(111) surface.

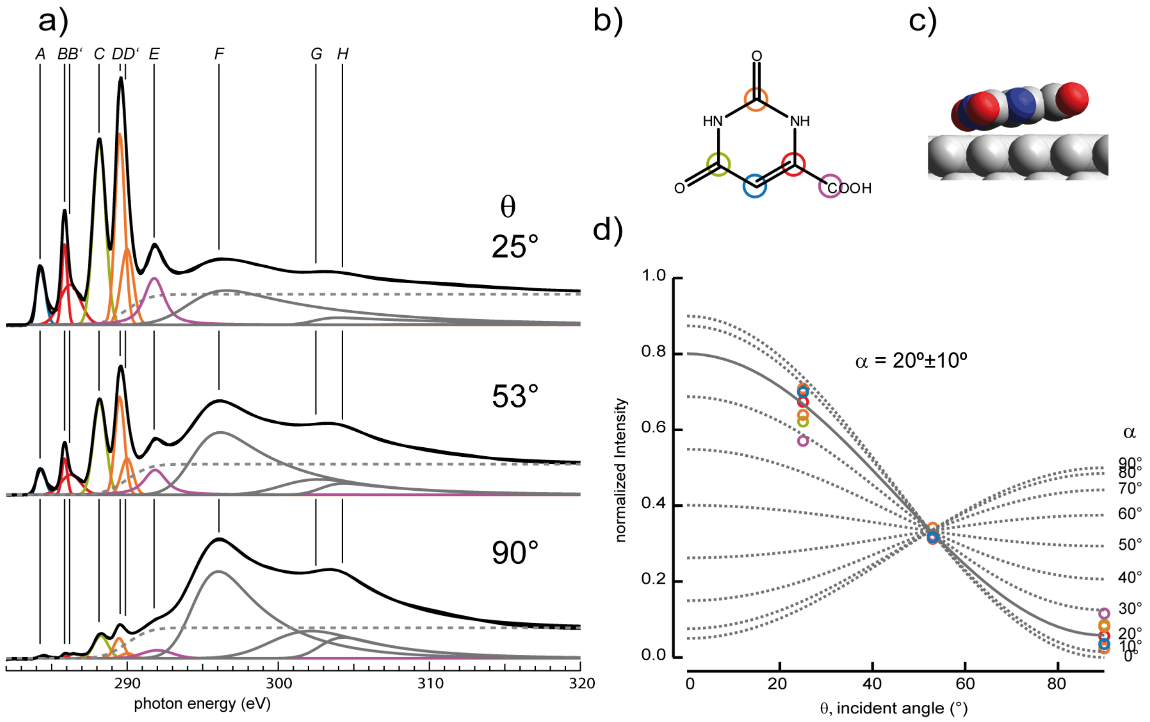

Figure 3.27: a) NEXAFS carbon K-edge spectra, recorded at three angles of photon incidence θ. b) Structural formula of orotic acid color coding the carbon atoms giving rise to the π^* transition resonances indicated by the same color in a) and d). c) Side view of a space filling orotic acid model on the Ag(111) surface illustrating of the average molecular orientation deduced by d) the curve fitting analysis of the intensities of the π^* resonances (circles) as a function of photon incidence angle.

of the C 1s core level spectra, see table 3.5). This values are in good agreement with the binding energies found for uracil on Ag(111) and for the carboxy group of L-cysteine on Ag(111) (subsections 3.1.2 and 3.2.1). Based on the N 1s spectra, which shows a single peak at 401.0 eV attributed to protonated nitrogen, and the O 1s spectra, featuring two signals at 532.2 eV and 533.8 eV attributed to the oxygen signals of the carbonyl and the hydroxy groups, respectively, it is deduced that the adsorbed molecule is intact and in its lactam form. All signals appear at lower binding energies, compared to the signals of the physisorbed molecules in the multilayer (figure 3.26a, top): the carbon signals shift by -0.1 to -0.2 eV while the oxygen and nitrogen signals shift by -0.4 and -0.3 eV, respectively. These shifts result from the multilayer to monolayer transition due to the higher hole screening by the metal substrate [115]. Annealing up to 370 K as well as reducing the surface coverage to ~ 0.7 ML did not lead to a change in the XPS and NEXAFS (discussed below) results.

NEXAFS measurements of the carbon K-edge were taken at three angles of photon in-

peaks	energy (eV)	assignment
A	284.3	C 1s → π^* (C5)
B	285.9	C 1s → π^* (C4)
B'	286.2	C 1s → π^* (C4)
C	288.2	C 1s → π^* (C2)
D	289.5	C 1s → π^* (C6)
D'	290.0	C 1s → π^* (C6)
E	291.8	C 1s → π^* (C9)
F	294.2	C 1s → σ^*
G	302.4	C 1s → σ^*
H	307.0	C 1s → σ^*

Table 3.6: Peak assignments for the C K-edge NEXAFS of ∼ 0.8 ML orotic acid on Ag(111) [116, 129].

cidence θ (figure 3.27a). The spectra show five sharp signals *A, B, C, D* and *E*, attributed to the C 1s to π^* transitions. The asymmetry of peaks *B* and *D*, represented by the additional peaks B' and D' result from transitions to the higher lying LUMO+1 and LUMO+2 transitions [116]. The highly asymmetric and broad signals above the adsorption edge (dotted line in figure 3.27) *F, G* and *H* result from C 1s to σ^*transitions. A detailed peak assignment is shown in table 3.6. The curve fitting analysis of the spectra's angular dependence reveals an average tilt angle of the molecular plane with respect to the surface plane of 20±10°. As NEXAFS spectroscopy is a space averaging technique, the deduced tilt angle must be understood as having contributions from the adsorption geometries of all molecules. A plausible explanation is that the molecules are slightly deformed resulting in a small tilt angle with respect to the surface. A similar tilt angle was recently found by DFT calculations for individual uracil molecules adsorbed on Au(100) [110]. Taking into account, that STM images reveal smaller disordered areas besides the close packed and the paddle wheel phase, one could also consider completely flat lying molecules forming the ordered phases and a smaller fraction of strongly tilted molecules forming disordered patches. Both scenarios are plausible regarding the fact, that STM resolution does not discriminate between these adsorption scenarios.

The presented data from STM, XPS and NEXAFS measurements provide a conclusive view on the self-assembly behavior of orotic acid on Ag(111). The comparison with uracil on Ag(111) studied under equivalent conditions, reveals many similarities but also interesting differences. As for uracil, a close packed structure nucleating at the step edges of the substrate could be observed on the surface. It comprises flat lying and intact molecules in contrary to the behavior of the molecule on the copper substrate discussed below. Additionally a more open second phase (the minority nanoporous paddle-wheel

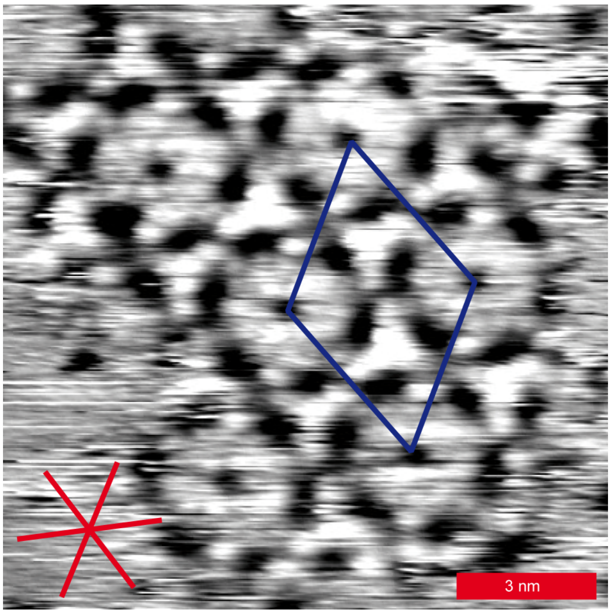

Figure 3.28: STM micrograph of the transient arabesque structure formed by orotic acid adsorbed on Cu(111) at room temperature ($I_t = 110\,\mathrm{pA}$, $U_t = 0.74\,\mathrm{V}$), with its unit cell indicated in blue and the Cu(111) high symmetry directions shown in red.

structure) could be found by the STM investigations. The nanoporous paddle-wheel structure has no analogue to the assemblies of uracil on Ag(111) and therefore is attributed to the influence of the additional carboxy group.

3.3.2 Orotic acid on Cu(111)

STM:

Changing the substrate to the more reactive Cu(111) surface results in STM images which exhibit an entirely different scenario of the orotic acid self-assembly. Investigations of coverages approximately between 0.5-0.8 ML and scanning temperatures of 190-300 K reveal a single periodic structure observed for $\sim$ 0.8 ML at $\sim$ 300 K. STM images of samples featuring coverages below 0.5 ML and/or being annealed up to 480 K showed only fuzzy stripes which indicate diffusing molecules. The transient “arabesque” structure shows up as small islands with undefined island borders and a lifetime of few minutes at 300 K, surrounded by diffusing molecules appearing as fuzzy stripes. This structure, which can be describe with a hexagonal $8(\sqrt{3} \times \sqrt{3})$ unit cell, is observed $\sim$ 0.5 h after molecular deposition and is not detectable after approximately 3 h. The STM images show a convolution of submolecular features, rendering impossible their unambiguous disentanglement to molecular topographic features and hence to molecular modeling of

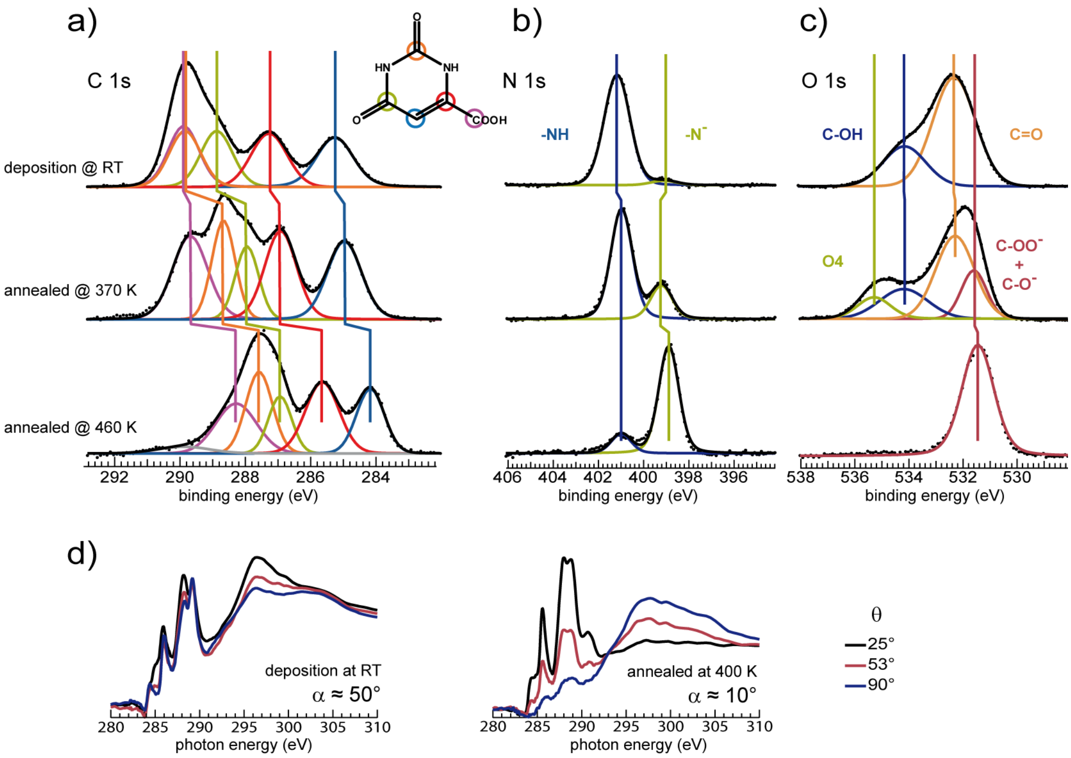

Figure 3.29: Temperature dependence of the orotic acid's chemical state and orientation on Cu(111). a) C 1s, b) N 1s and c) O 1s core level spectra after deposition at room temperature (top), after annealing to 370 K (middle) and 460 K (bottom). d) NEXAFS carbon K-edge spectra acquired at three different angles of photon incidence, θ, after deposition at room temperature (left) and after annealing the sample to 400 K (right).

this structure.

X-ray spectroscopy:

Figure 3.26 (bottom) summarizes the XP core level spectra for a high submonolayer coverage of approximately 0.8 ML of orotic acid as deposited at room temperature in contact with the close packed copper substrate. The C 1s core level spectrum (figure 3.26a, bottom) is similar to the C 1s spectrum for the full monolayer adsorbed on the silver surface. Small shifts of ± 0.1-0.2 eV (Table 3.5) with respect to the C 1s spectrum of orotic acid on Ag(111) indicate small differences in the interaction with the underlying substrate. The N 1s spectrum (figure 3.26b, bottom) shows a dominant signal at a binding energy of 401.2 eV attributed to the protonated nitrogen atoms of the pyrimidine ring, and a small peak at a binding energy of 399.1 eV assigned to deprotonated nitrogen atoms (-N^-). The two signals of the O 1s region (figure 3.26c, bottom) representing the carbonylic

assignment	dep. at RT E_B(eV)	ann. at 370 K E_B(eV)	ann. at 460 K E_B(eV)
C2	287.4	288.8	287.7
C4	290.0	287.0	285.8
C5	285.4	285.1	284.3
C6	289.0	288.1	287.1
C9	290.0	289.8	288.4
-NH	401.2	401.0	401.0
$-N^-$	399.1	399.2	398.9
-C-OH	534.2	534.2	-
-C=O	532.4	532.3	-
$-CO^-$+ $-COO^-$	-	531.6	531.5
O4	-	535.3	-

Table 3.7: Peak assignment of the C 1s, N 1s and the O 1s core level spectra for the as deposited layer and the sample annealed at 370 K and 460 K

(-C=O) and hydroxylic (-C-OH) oxygens shift by +0.2 eV and +0.4 eV with respect to the signals of orotic acid adsorbed on Ag(111) to binding energies of 532.4 eV and 534.2 eV, respectively. This behavior is somewhat surprising, as at 300 K the carboxy group has been reported to deprotonate to carboxylate upon contact with the copper surface [148–150] and uracil undergoes complete deprotonation of the N3 atom (cf. figure 3.9) upon room temperature deposition (subsection 3.2.2). Annealing the sample to 370 K (figure 3.29a-c, middle, table 3.7 summarizes the binding energies of the peaks shown in figure 3.29) results in an increase of the signal corresponding to deprotonated nitrogens while concomitantly the O 1s spectrum shows a new signal at a binding energy of 531.6 eV. As the signal assigned to the carboxy-related carbon in the C 1s spectrum shifts (figure 3.29a, middle) by only 0.2 eV, it is assumed, that a significant part of the carboxy groups stay protonated. A fourth peak (O4) arises at an unusual high binding energy of 535.3 eV, which is explained with a state involving orotic acid oxygen with a high positive partial charge, as common UHV chamber contaminants such as water or carbon monoxide, which often account for signals in this range of binding energies, would desorb from the Cu(111) surface well below 370 K [151, 152]. As the annealing to 370 K affects more the C2 and C6 core levels than the C4 it is postulated that there is a preferential deprotonation of the N1 position at 370 K, as it was observed for uracil. Further annealing of the sample to a temperature of 460 K leads to an almost complete deprotonation of all functional groups (figure 3.29a-c, bottom and table 3.7) including the carboxy group and a strong interaction with the copper surface via the oxygen atoms as supposed by the remarkable shifts of all C 1s signals. A small signal at 290.0 eV accounts for contributions

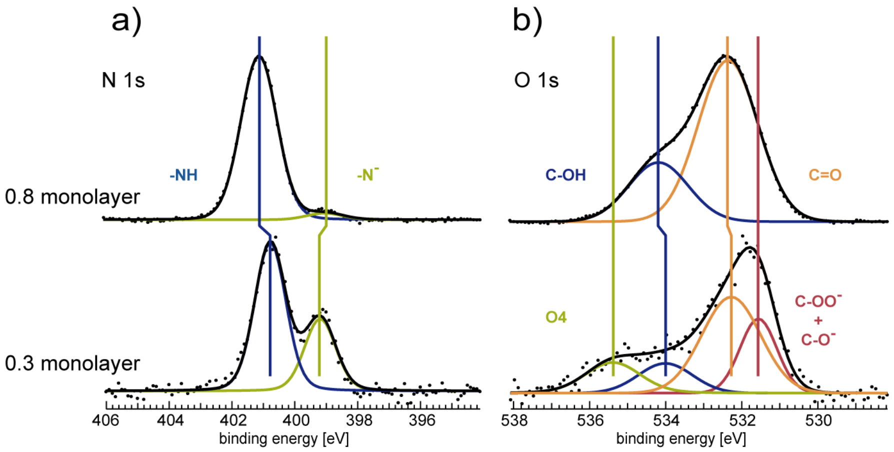

Figure 3.30: XP spectra of the a) N 1s and b) O 1s region, showing the chemical state of as-deposited orotic acid on Cu(111) at room temperature for a coverage of ∼ 0.8 monolayer (top) and a coverage of 0.3 monolayer (bottom) .

assignment	**0.8 ML** **E_B (eV)**	**0.3 ML** **E_B(eV)**
-NH	401.2	400.8
-N$^-$	399.1	399.2
-C-OH	534.2	534.0
-C=O	532.4	532.3
-CO$^-$+ -COO$^-$	-	531.6
O4	-	535.4

Table 3.8: Peak assignment of the N 1s and the O 1s core level spectra for the as deposited layer at coverages of 0.8 and 0.3 monolayers.

of a residue of partly protonated orotic acid species. The disappearance of the carbonyl signal indicates significant charge redistribution within the ring with a relocalization of the charge at the O7 an O8 positions and a complete deprotonation of the carboxy group. In contrary to the existence of the almost intact molecules upon deposition, the temperature dependent deprotonation of the aminic nitrogens is comparable with the behavior of uracil on Cu(111) (subsection 3.2.2). The analysis of the NEXAFS C K-edge spectra angular dependence reveals, that concurrently to the deprotonation, the average orientation of the molecules with respect to the surface changes significantly. While the spectra of the as-deposited layer at room temperature reveals little dependence on the photon incidence angle, thus indicating an average molecular tilt angle of ∼ 50° with respect to the surface, the molecular plane is oriented nearly parallel to the surface plane after annealing the sample to 400 K (figure 3.29c).

The comparison of the XPS data corresponding to a high submonolayer coverage with the one for a smaller coverage of $\sim$ 0.3 ML reveals similarities with the annealing series in terms of deprotonation of the molecules. Besides the peak at a binding energy of 400.8 eV representing the protonated nitrogen atoms, the N 1s spectrum of a $\sim$ 0.3 monolayer coverage of orotic acid on Cu(111) (figure 3.30a, bottom) shows a significant signal at a binding energy of 399.2 eV, which corresponds to the amount of the molecules with deprotonated aminic groups upon deposition at lower coverages. This conclusion is supported by the XPS data of the O 1s region (figure 3.30b, bottom), which shows, besides the signals attributed to carbonyl and hydroxy groups, a significant contribution of the signal at a binding energy of 531.6 eV indicating that a considerable number of carboxy units is deprotonated as well. Similar to the annealed (370 K) sample featuring the full monolayer, also the aforementioned O4 species at high binding energies (535.4 eV) is present under these preparation conditions, leading to the conclusion, that annealing as well as reducing of the coverage leads to the same chemical changes of orotic acid on Cu(111). These results indicate, that deprotonation is dependent on the time after molecular deposition and can be accelerated by heat treatment. High coverages protect the molecules from immediate deprotonation. Taking into account the time frame within which the arabesque structure is observed, this structure might be the result of a specific ratio of differently protonated molecular species.

3.4 Summary and conclusion

By combining STM measurements with the X-ray spectroscopy techniques XPS and NEXAFS, the adsorption behavior and self-assembly of orotic acid as well as the correlation between temperature and coverage and the chemical state could be shown. On the close packed silver surface, we can find two different, long range ordered assemblies formed by intact, flat lying orotic acid units in the lactam form. The structural arrangement as well as the molecular chemical state and the orientation with respect to the silver surface show no dependence on temperature or coverage. Apparently, the molecular dimer illustrates a particularly stable configuration, as both structures include, at least partly, orotic acid dimers. The chiral and nanoporous minority paddle wheel phase additionally has the ability to trap molecules in the central cavities formed by the six-membered ring of molecules. Comparing the results with the self-assembly of uracil on Ag(111), the additional carboxy group differentiating the orotic acid from uracil seems to have a significant effect on the intermolecular interactions which drive the self-assembled structures.

On Cu(111) only a single periodic structure (“arabesque” phase) can be found by STM investigations at 190-300 K for coverages corresponding to approximately 0.5-0.8 ML.

XPS and NEXAFS measurements show, that a monolayer of orotic acid adsorbs mostly intact and considerably tilted with respect to the surface. Temperature treatment triggers gradual deprotonation of all functional units, including the carboxy group and a charge redistribution within the molecular ring. At the same time, the molecules tilt from an upstanding orientation to a flat-lying one. Reduction of the initial coverage results in deprotonation of a significant percentage of both amino an carboxy groups at room temperature, showing a similar chemical state of orotic acid molecules as a high submonolayer coverage after annealing the sample to 370 K. These results indicate, that deprotonation of the functional units takes place in a time frame of minutes to hours and is accelerated by heat treatment, while a high packing density protects the functional units from immediate deprotonation or kinetically hinders the deprotonation process. Assuming so, the arabesque structure can be attributed to a molecular structure resulting from the periodic arrangement of a specific ratio of coexisting molecular species. On the copper substrate, the carboxy substituent presumably interferes with the formation of an ordered overlayer and its presence is also shown to protect the pyrimidine amino group at high packing densities.

These results show the significant effect of the additional carboxy substituent of the uracil derivative orotic acid on the surface-confined self-assembly and even chemical behavior, furthering prospects of distinct tailoring of biofunctionalized surfaces by substituents.

3.5 Bisphenol A on Ag(111) and Cu(111): Self-assembly and stepwise thermal deprotonation

Bisphenol A (BPA, systematic name: 4,4'-(propane-2,2-diyl)diphenol, figure 3.31) is a chemical commonly employed as a monomer in polymerization reactions, e.g. for the production of polycarbonates widely used in products such as optical media, lenses and bottles. The high exposure of humans due to its use in plastics for food and beverage packaging has brought this chemical into the public eye. It has been shown to have hormonal activity and as an artificial estrogen it is linked to infertility [153] and other health hazards [154]. Additionally, BPA is under suspicion of modifying DNA methylation processes [25, 155], a natural procedure to activate and silence certain genes which are playing a pronounced role in DNA error correction. In nature DNA methylation is performed by methyl-transferase proteins but environmental influences such as chemicals have also been reported to trigger or suppress the methylation processes and thus altering the so called epigenetic code. Recent studies show that BPA causes DNA hypomethylation [25, 155], however at present there is a lack of a mechanistic insight of the molecular events and the role of the BPA functional moieties in this process. A first step towards understanding these processes is a detailed understanding of the molecule's reactivity in a well-defined environment as for example provided by a metal single crystal substrate under ultra high vacuum (UHV) conditions. Previous studies of molecules with biological relevance adsorbed on metal surfaces have shown that the intermolecular interactions are very sensitive to changes in the chemical state of the molecules and are manifested by metamorphoses of the molecular self-assembly ([45, 52, 58], see also section 3.1, 3.2 and 3.3). Insight in the reactivity of a molecule's functional groups and the activation certain reactive groups in a precise manner determines very delicate intermolecular interactions which in turn enable certain reaction outcomes. In this context, the stable functionalization of a surface with bisphenol A molecules might offer a way for precisely triggering methylation and demethylation processes of DNA bases and their derivatives. Hitherto the studies of the BPA reactivity have focused on the biological (e.g. [25, 155]), chemical [156, 157] and technological [158–161] properties of BPA as a polymerization monomer and the widespread related polymer BPA polycarbonate.

Here, a comprehensive study on the temperature dependent self-assembly and chemical behavior of bisphenol A adsorbed on Ag(111) and Cu(111) is presented. The silver substrate was chosen due to its weak reactivity towards several organic compounds (see sections 3.2.1 and 3.3.1) including phenol moieties (e.g. [46, 162]). In the temperature range from 180 K to 250 K two different coexisting structures composed of the same molecular dimer were observed. Increasing the sample temperature to 250-340 K, an

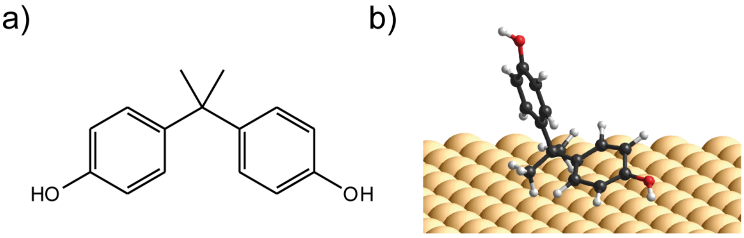

Figure 3.31: Bisphenol A (BPA): a) Molecular structure and b) possible adsorption conformation of the BPA molecule on the surface

additional third structure, consisting of trimers, showed up, the phase transition being reversible.

The copper substrate, which is offering a well-defined atomically flat surface was used as a catalytically active substrate with the ability to anchor molecules on the surface and thus allowing the formation of high temperature phases. With STM, five distinct molecular assemblies with irreversible transformations as a function of the sample annealing temperature were observed. High resolution XPS measurements were employed to shed light to the chemical state of the molecules and to correlate the stability of the hydroxy groups to the STM observations. Angle resolved NEXAFS provided information concerning the orientation of the molecules' aromatic rings towards the surface and, based on these informations, a molecular model for each overlayer structure is proposed

3.5.1 BPA on Ag(111):

STM:

STM investigations of bisphenol A on the Ag(111) surface revealed three different BPA polymorphs of two dimensional crystallization. In a temperature range of 180 K to 250 K (from now on referred to as "dimeric region"), two different structures composed of molecular dimers can be found on the surface (figure 3.32), whereas at sample temperatures between 250 K and 340 K ("trimeric region") an additional third structure (figure 3.33) consisting of trimer units is observed. This structure is coexistent with the dimeric structures but for temperatures above 300 K representing the majority of the molecular lattice. The thermal formation of the trimeric structure is reversible, that is, cooling down a sample below 250 K leads to a dissolution of the trimeric structure leaving only the dimeric structures on the surface. Further annealing of the sample to 340 K and above results in the desorption of the molecules.

Both dimeric structures comprise the same molecular dimer with an intermolecular spacing of $d_1 = 7.5 \pm 0.7$ Å which are tilted by $\pm 23.5°$ with respect to the substrates $\langle 1\bar{1}0 \rangle$

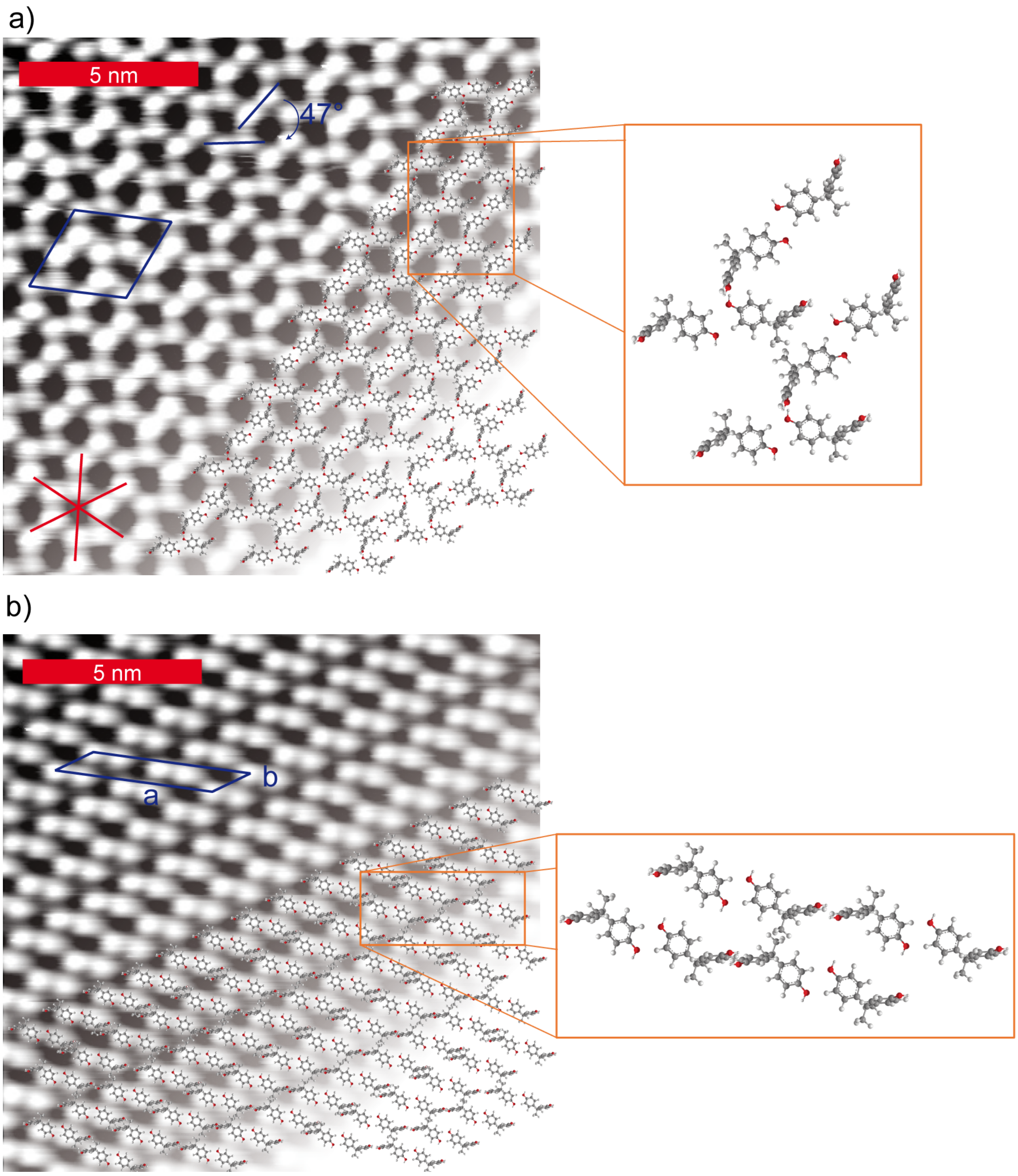

Figure 3.32: STM images and superimposed molecular models of the two different dimeric structures of BPA on Ag(111). a) Arrangement consisting of dimers with two different tilt angles (indicated in blue) and a hexagonal unit cell (tilted dimer arrangement, $I_t = 130\,\mathrm{pA}$, $U_t = 1.25\,\mathrm{V}$, $T_{sample} = 190\,\mathrm{K}$) and b) dimeric arrangement comprising dimers with the same tilt angle and a rhomboidal unit cell (staggered dimer arrangement, $I_t = 120\,\mathrm{pA}$, $U_t = 1.25\,\mathrm{V}$, $T_{sample} = 190\,\mathrm{K}$). The unit cells are indicated in blue, the Ag(111) high symmetry directions are indicated in red in a).

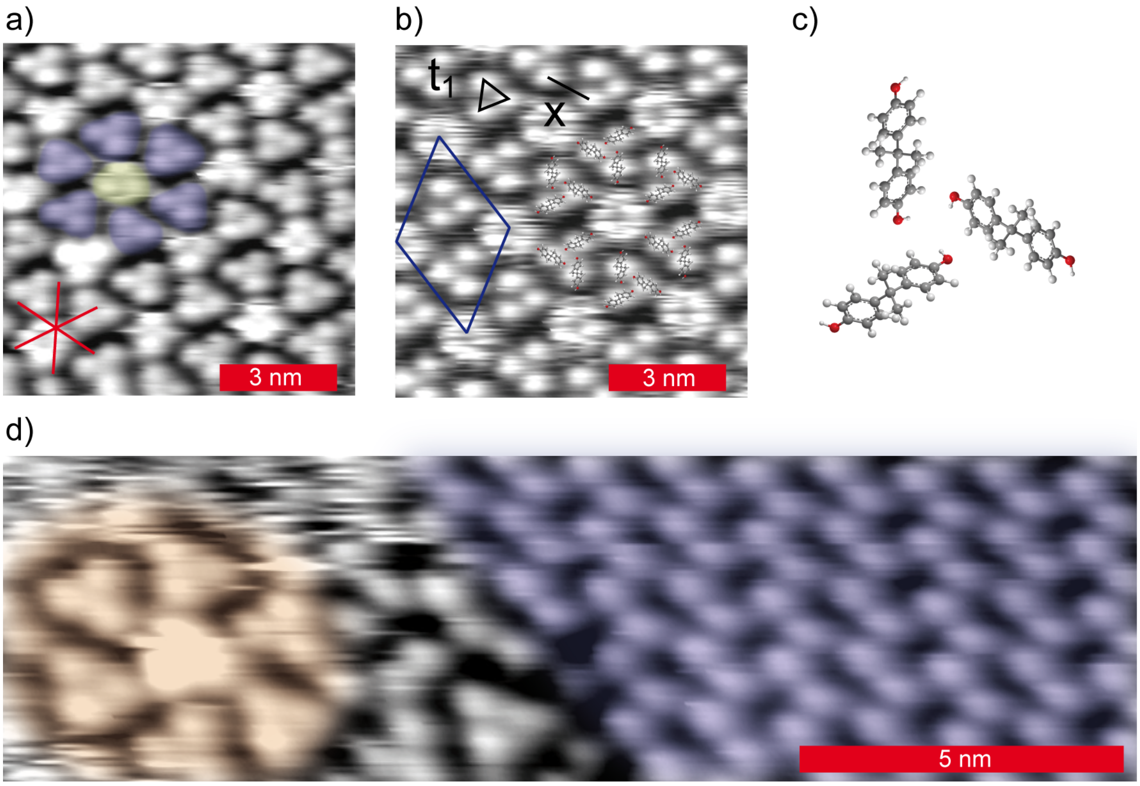

Figure 3.33: STM micrographs of the BPA trimeric structure on Ag(111): a) Trimeric structure at 260 K ($I_t = 140\,\text{pA}$, $U_t = 1.25\,\text{V}$) with the static trimers highlighted in blue and the immobilized, trapped trimer highlighted in green. The Ag(111) high symmetry axes are indicated in red. b) Trimeric structure at 290 K ($I_t = 130\,\text{pA}$, $U_t = 1.25\,\text{V}$) with the trapped trimer rotating. The unit cell is shown in blue, the molecular spacing of the trimer t_1 in black. A molecular model is superimposed to the STM image. c) Magnification of the molecular model of a single trimer. d) STM image of both structures coexisting at 250 K: the trimeric structure is highlighted in orange and the staggered dimeric arrangement is highlighted in blue ($I_t = 140\,\text{pA}$, $U_t = 1.25\,\text{V}$).

directions, resulting in 6 different orientations of the dimer with respect to the underlying substrate. The first structure consists of dimers featuring two different orientations, forming an angle of 47° between them (“tilted dimeric arrangement”, figure 3.32a). The resulting hexagonal unit cell has a side length of $2.64 \pm 0.09\,\text{nm}$ and is tilted by 27° with respect to the substrate’s high symmetry directions. The second structure consists of dimers all of which are aligned in the same direction and have a staggered arrangement. It is characterized by a rhomboidal unit cell with $a = 4.38 \pm 0.20\,\text{nm}$, $b = 1.26 \pm 0.06\,\text{nm}$ and an angle of 33° between them, b running along the the Ag(111) high symmetry directions.

Increasing the sample temperature to temperatures between 250 K and 340 K results in the appearance of the third structure comprising trimeric units. Six trimers are forming a cavity with an additional trapped species (figure 3.33). In a temperature range of approximately 250-260 K, the trapped species is nearly immobilized and can be identified to consist of another BPA trimer (figure 3.33a). At room temperature it appears fuzzy and doughnut-shaped (figure 3.33b), indicating rotational movement constrained by the trimers forming the cavity. The structure can be characterized by a hexagonal unit cell with a side length of 2.88 ± 0.1 nm, the axis of the unit cell is tilted by 18° with respect to the silver $\langle 1\bar{1}0 \rangle$ directions. The stable trimers are characterized by an intermolecular spacing of $t_1 = 8.0 \pm 1.1$ Å, the sides of the trimer being approximately aligned along the Ag(111) high symmetry axes. The diameter of the rotating unit was measured to be approximately 1.2 ± 0.2 nm, a value which matches a rotating trimer. The spacing between individual trimers is significantly larger than the spacing of the trimer t_1, the distance x (see figure 3.33b) has been measured to be 1.4 ± 0.2 nm. Together with the existence of the rotating trimers this might indicate that the static trimers are rather stabilized by marked interaction with the surface, e.g. as a result of preferred adsorption sites, than by long range attractive interactions between neighboring trimers.

X-ray spectroscopy:

In order to get information regarding the chemical state and orientation of the molecules, XPS and NEXAFS measurements were performed. The O 1s spectrum (figure 3.34) of BPA adsorbed on Ag(111) at 300 K and cooled down to 130 K shows one prominent peak at a binding energy of 533.6 eV, attributed to the oxygen of an intact hydroxy group [46]. Warming the sample again to 300 K leads to a shift of the hydroxy-related signal of -0.5 eV to a binding energy of 533.1 eV and the appearance of a second, smaller signal with a binding energy of 530.6 eV and a relative intensity of 18 %, which was assigned to the oxygen of a deprotonated hydroxy group. The shift in the main signal is explained with differences in the local chemical environment of the oxygen atoms, for example a change of conformation and orientation with respect to the surface, of the BPA molecules assembling into the trimeric structure, which is predominant at this temperature. The partial deprotonation of the phenols' hydroxy groups cannot be reversible and is attributed to a surface side reaction not manifested in the reversible BPA polymorphism observed and therefore not addressed in the subsequent structural models proposed.

Angle-resolved NEXAFS spectra (figure 3.35a) are virtually indistinguishable for both temperature regimes. Curve fitting analysis (figure 3.35b) reveals an average tilt angle of the phenol rings of 40° ± 10° with respect to the surface plane. As the absorption energy of the two phenol rings are superimposed to the same signal, the deduced tilt angle must be considered as having contributions from both rings. This allows a broad

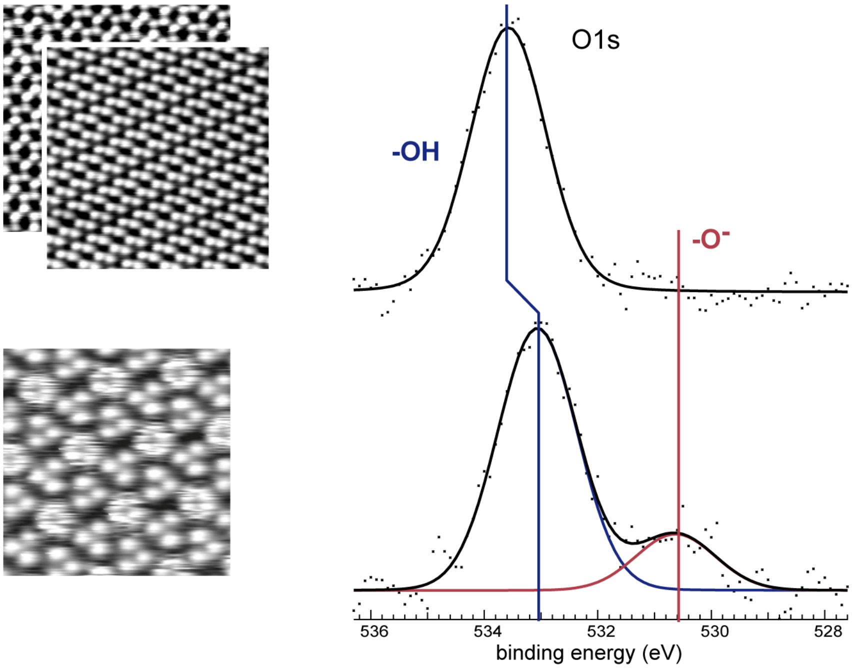

Figure 3.34: High-resolution X-ray photoelectron spectra of the O 1s core level corresponding to the dimeric region (top) and trimeric region (bottom) of BPA adsorbed on Ag(111).

variety of different molecular conformations with tilt angles of the individual phenol groups ranging to combinations of 0° and 80° to 40° and 40°.

Modeling:

The information gained from the STM and X-ray spectroscopy investigation allows the proposal of a molecular model. Neglecting the deprotonated side product, an intact, i.e. fully protonated, BPA molecule forms the basis for all proposed models. Taking the average tilt angle of 40°±10° into account, there are two plausible orientations of the molecule with respect to the surface. One option is a "L-shape" conformation of the molecule with one phenol ring being nearly parallel to the silver surface (phenol has been reported to adsorb nearly parallel to the surface at submonolayer coverage [163]) and the other phenol ring pointing away from the surface with a tilt angle of 70-80° with respect to the surface (cf. figure 3.31b), the second option is a circumflex-like conformation of the two phenol rings, which both tilt by 30-40° with respect to the surface and both hydroxy groups point towards the surface (cf. figure 3.33).

A possible model for the dimers which build up the two different dimeric structures discussed above are two molecules featuring the "L-shaped" configuration. The flat lying phenol rings point towards each other, allowing attractive interactions or even hydrogen

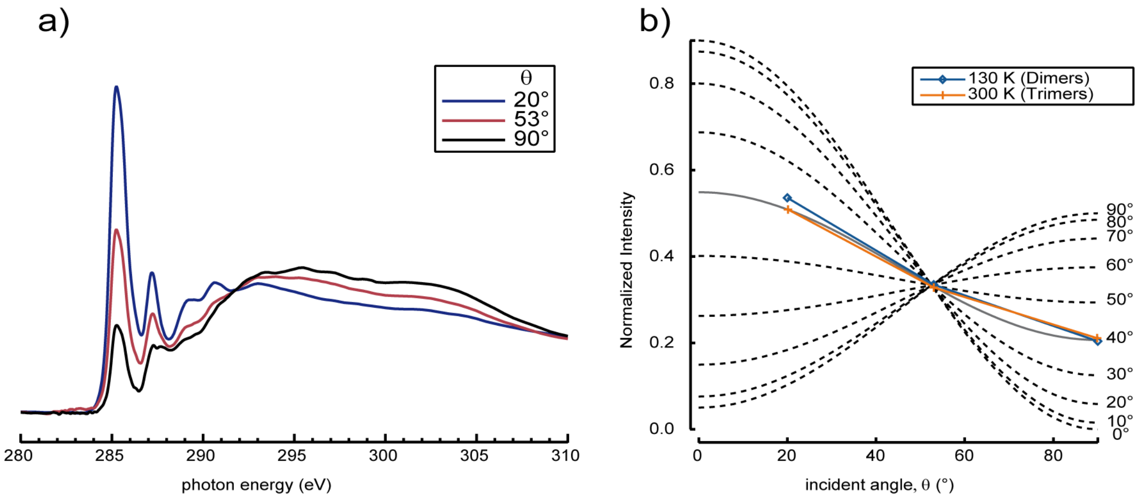

Figure 3.35: a) Normalized experimental C K-edge NEXAFS data at three angles of photon incidence, θ, for the dimeric region at 190 K. b) Curve-fitting analysis of the photon angle dependence of the low energy π^* resonance for sample temperatures of 190 K and 300 K, featuring the dimeric arrangements and the trimeric structure, respectively.

bonding between the phenyl ring's protons and the hydroxy group (figure 3.32, superimposed models). Interaction with neighboring dimers can be achieved by π-stacking and other non covalent interactions (figure 3.32b). XPS data for the trimeric region (250-340 K) suggests a change in the local chemical environment of the hydroxy groups and the intermolecular spacing t_1 within the trimer is significantly lower than measured for the trimeric binding motifs of BPA on Cu, t_2 and t_3. Taking this information into account, a different orientation on BPA, namely the second described option with the circumflex-like conformation, is employed to create a model for the trimer structure (see figure 3.33b-c for superimposed model and magnification of the trimer binding motif). Both hydroxy groups of the molecule are pointing towards the silver surface (consistent with the downward shift of the O 1s OH contribution by 0.5 eV [164]) and interacting with the inward pointing phenol ring of the neighboring molecule.

3.5.2 BPA on Cu(111):

STM:

Upon deposition onto a Cu(111) sample held at $\sim$ 260 K, the BPA molecules assemble into an irregular open porous network (henceforth referred to as "network-phase") consisting of filaments build by BPA dimers and connected by trimers (figure 3.36a). Warming the sample to $\sim$ 290 K (room temperature) results in a structure consisting purely of dimers ("dimer-phase") which assemble into surface chiral mill-like structures consti-

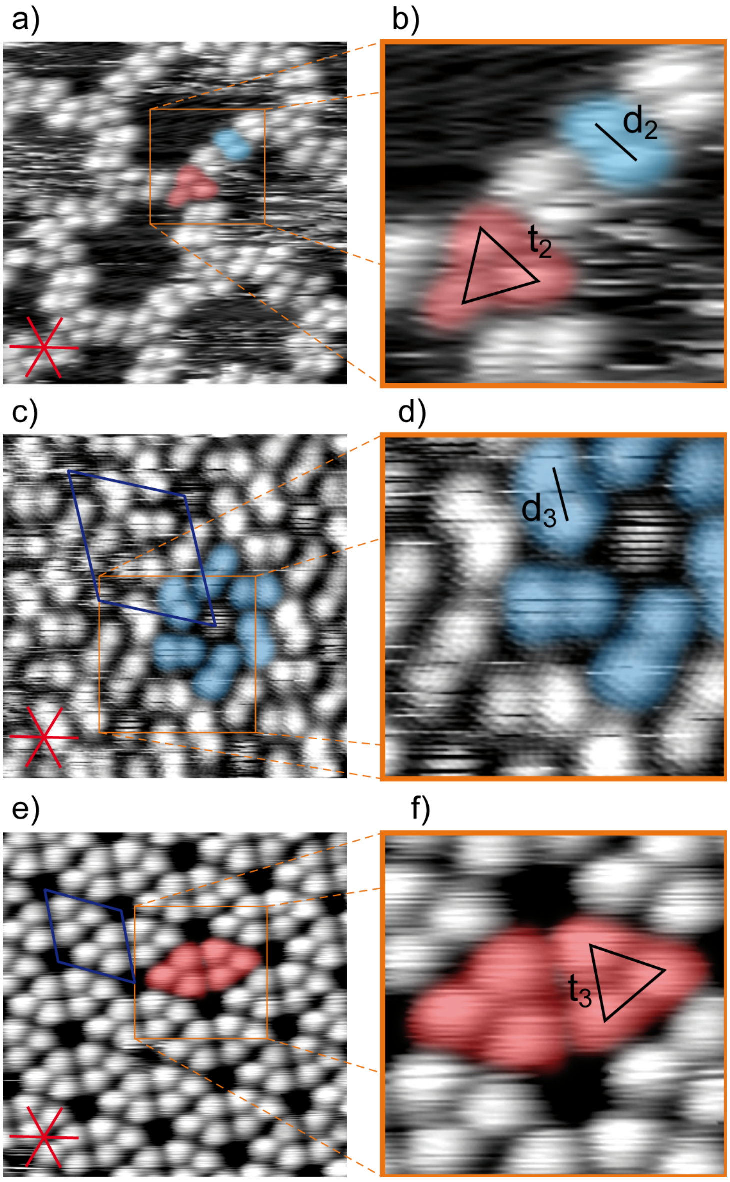

Figure 3.36: STM images of different structures of BPA on Cu(111). The Cu(111) high symmetry axes are indicated in red in images a), c) and e). a) Network-phase, observed upon deposition at a sample temperature of ~ 260 K ($13.2 \times 13.2\,\mathrm{nm}^2$, $I_t = 120\,\mathrm{pA}$, $U_\mathrm{t} = 1.5\,\mathrm{V}$) with the trimer and the dimer motifs highlighted in red and blue respectively. b) Magnification ($4.4 \times 4.4\,\mathrm{nm}^2$) of the area indicated in a) with the intermolecular spacings t_2 and d_2 annotated. c) Dimer-phase observed after warming the network-phase to 290 K ($9.7 \times 9.7\,\mathrm{nm}^2$, $I_t = 80\,\mathrm{pA}$, $U_t = 2.2\,\mathrm{V}$). The *(R)*-mill and the unit cell are indicated in blue. d) Magnification ($4.4 \times 4.4\,\mathrm{nm}^2$) of the area indicated in c) with d_3 marking the spacing of the dimer. e) Trimer-phase observed after warming the dimer-phase to 300-340 K ($11.4 \times 11.4\,\mathrm{nm}^2$, $I_t = 90\,\mathrm{pA}$, $U_t = 2.5\,\mathrm{V}$). Two facing trimers and the unit cell are indicated in red and blue, respectively. (f) Magnification ($4.4 \times 4.4\,\mathrm{nm}^2$) of the area indicated in e) with t_3 marking the molecule to molecule distance with the trimer.

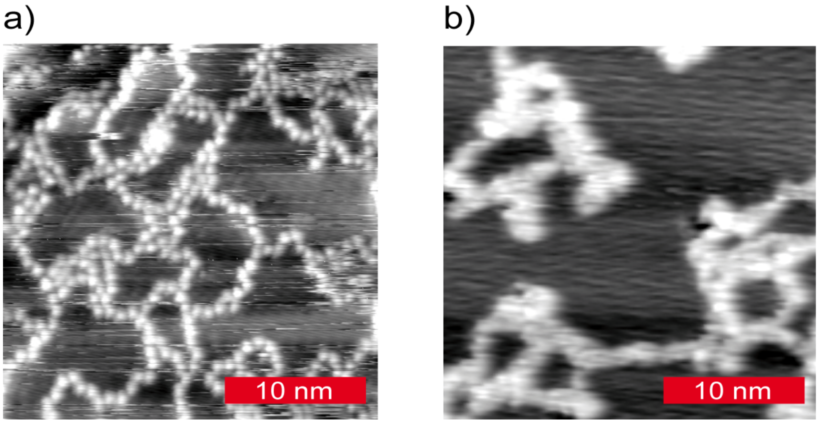

Figure 3.37: STM micrographs of the molecular chain phases formed after annealing to 470 K and 700 K. a) After annealing the sample to 470-570 K (top, $I_t = 120\,\text{pA}$, $U_t = 1.77\,\text{V}$) distinct protrusions can be distinguished in STM images. b) These features were smeared out after annealing to $\sim$ 700 K (bottom, $I_t = 120\,\text{pA}$, $U_t = 1.25\,\text{V}$) and the chains on the surface appear less defined.

tuting a two-dimensional supramolecular network (highlighted in blue in figure 3.36c). Further annealing to temperatures between 300 and 340 K causes the BPA layer to change into a structure build up only from trimers ("trimer-phase", figure 3.36e). The dimer- and trimer-phase featuring a long-range order and extend almost free of defects over large areas of the sample. Annealing the crystal to 470 K, a new structure consisting of chains, formed by identifiable molecular features appears. Figure 3.37a shows a typical STM image of this phase, which is stable up to a temperature of 570 K. For higher annealing temperatures, differences between individual molecular features start to blur, until no protrusions are distinguishable within the chains for $T \geq 700$ K (figure 3.37b).

The network-phase consists of filaments composed by dimers which are connected by trimeric motifs (figure 3.36a). These dimers are characterized by monomers with a spacing of $d_2 = 7.4 \pm 1.1$ Å and pairing along the $\langle 1\bar{1}0 \rangle$ direction of the underlying copper substrate. The trimer molecules have a distance of $t_2 = 9.1 \pm 1.0$ Å with respect to each other with t_2 running along the $\langle 1\bar{2}1 \rangle$ Cu(111) direction (figure 3.36b). The pore size within the molecular network varies greatly between values of 3 nm^2 to 22 nm^2, but 40 % of these pores form a distinct star-like motif with a measured pore size of 15-20 nm^2. These star shaped pores consist of six dimer pairs, connected by trimers (figure 3.38). The differences in the pore size and shape originate in small variations of this assembly, such as an additional or missing dimer or a different orientation of one of the dimer pairs. Within the network pores, streaks indicate diffusing molecules on the surface imaged at 180 K.

The dimer-phase, showing up after warming the sample to 290 K, consists of six dimers

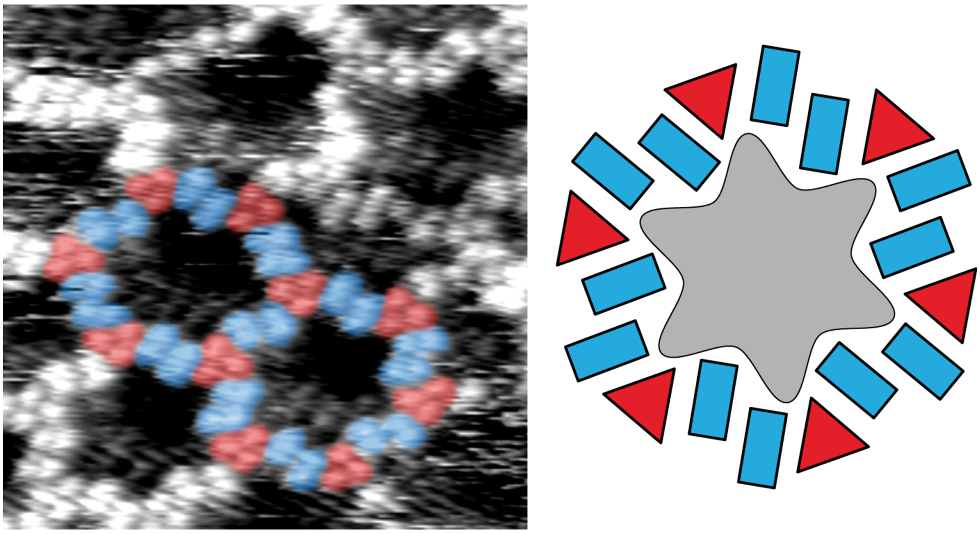

Figure 3.38: Star-shaped pores a) observed in the network-phase (17.6 × 17.6 nm^2, $I_t = 130\,pA$, $U_t = 1.5\,V$) and highlighted in color along with b) a schematic model of this arrangement. The red triangles and blue rectangles represent the trimers and dimers, respectively.

forming a mill structure. In some of the centers of each six dimers of the mill structure one can discern a protrusion of fuzzy appearance representing a trapped molecule, its diffusion constrained by the surrounding dimers. These dimers are also paired along the Cu(111) high symmetry directions and the spacing between the molecules is $d_3 = 6.7 \pm 0.4$ Å, a value that is close to d_1 and d_2 observed for the dimers on the silver surface and of the network-phase. The molecular superstructure can be described by a hexagonal unit cell with a side length of 3.3 ± 0.2 nm, rotated by 8° with respect to the copper $\langle 1\bar{1}0 \rangle$ directions (figure 3.36c). Notably, extended molecular domain of both chiral mills (cf. figure 3.39a) were identified in the STM study with the two dimensional islands consisting solely of either *(R)*- or *(S)*-mills without any chiral defects.

Similar to the dimer-phase, the trimer-phase shows the molecules to assemble in a highly ordered hexagonal arrangement with a unit cell side length of 2.7±0.1 nm and the axes rotated by 14° with respect to the Cu $\langle 1\bar{1}0 \rangle$ directions (figure 3.36e). The spacing of the individual molecules in the trimer is $t_3 = 9.7 \pm 0.5$ Å (figure 3.36f). Due to the rotation of the overlayer unit cell with respect to the substrate, the trimer-phase gives also rise to six symmetrically equivalent domains (figure 3.39b).

Annealing to 470 K results in a random chains structure composed from single molecules (figure 3.37a), in contrast to the described network phase, where the filaments are formed from BPA dimers, with a molecule-molecule distance of 9.6 ± 0.1 Å. This chains structure was observed up to an annealing temperature of 570 K. At this temperature the individual features of the molecular structure start to smear out. Further annealing to 700 K results in no distinct features within the chains which become more contracted (figure 3.37b). Concomitantly, the chain distribution gets more irregular and the apparent height decreases by $\sim$ 0.4 Å. It is noteworthy that, although the dimer-phase and the trimer-phase exhibit significant surface mobility at room temperature, room temperature STM data of the chain structures reveals their high stability, which is typical for strong intermolecular linkage and/or strong molecule substrate interaction.

X-ray spectroscopy:

While the C 1s spectrum of BPA adsorbed on Cu(111) does not change as a function of temperatures up to 520 K (figure 3.40, left), the O 1s spectra are significantly stronger effected by the temperature. The O 1s spectrum for the network phase can be fitted with three peaks (figure 3.40a, right). The signals at binding energies of 532.7 eV and 531.1 eV can be assigned to the oxygen of phenol (Ph-OH) and phenolate (Ph-O^-) groups, respectively. BPA, which can act as a weak acid (pK_A = 9.8 [165]) has a higher probability of hydroxy group deprotonation than for example ethanol (pK_A = 16), because the resulting phenolate species is stabilized via the aromatic ring. A third signal showing up as a high energy shoulder of the O 1s spectrum at a binding energy of 534.0 eV is attributed to H_2O, originating from the residual gases in the vacuum sticking to the Cu(111) at 140 K. The alternative scenario of CO as a possible contaminant can be ruled out based on the cleanness of the C 1s signal [166, 167]. The ratio of the relative intensities of the -OH : -O^- group signals is $\sim$ 1.3 : 1. This ratio indicates that approximately half of the BPA hydroxy groups in the dimer-phase deprotonate upon adsorption at $\sim$ 260 K. This conversion to phenolate is consistent with phenol adsorption on the Cu(110) surface [168].

Warming to 290 K and higher leads to an increase of the phenolate signal at a binding energy of 530.9 eV and a concomitant decrease of the phenol signal intensity at a binding energy of 532.7 eV (figure 3.40, right). The high binding energy shoulder disappears, supporting its earlier assignment to H_2O. The ratio of the intensities of the two signals of this surface amounts to $\sim$ 1 : 3, that is, one out of four hydroxy groups retains its proton. The hydroxy signal has exactly the same binding energy in all three phases, whereas the hydroxylate signal shifts by 0.2 eV to lower binding energies at $\sim$ 290 K, which is the temperature marking the transition from the network-phase to the dimer-phase. This shift is tentatively explained by a difference in the local environment of the deprotonated groups linked with increased intermolecular interactions in the more dense phases. Thermal treatment of the BPA overlayer to 340 K, leaves the XPS signatures virtually unaffected. This indicates that no chemical transformation marks the structural change from the dimer-phase to the trimer-phase, that is these two phases are two di-

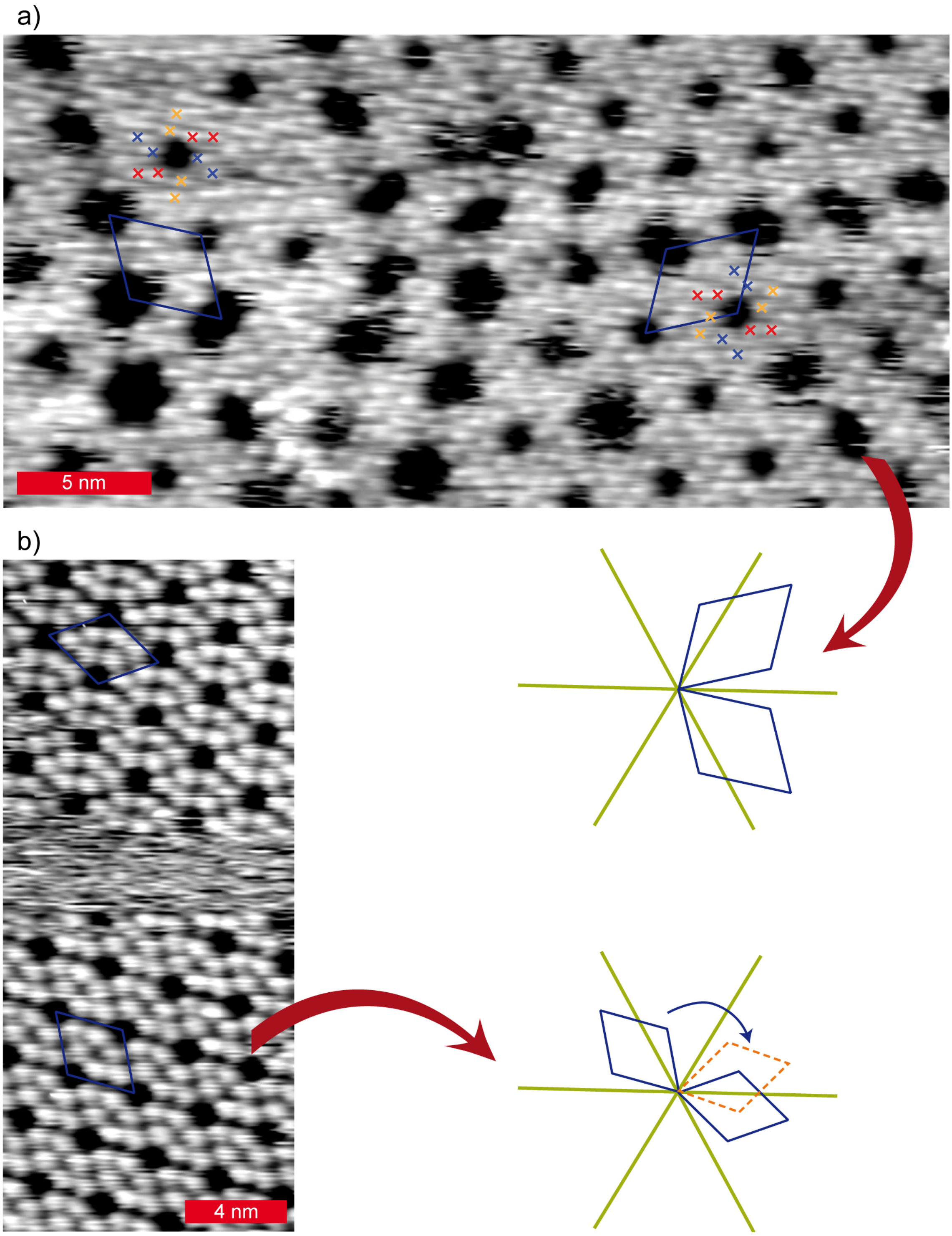

Figure 3.39: STM images of the a) dimer- and b) trimer-phase showing both chiral mirror phases. The green stars show the high symmetry directions of the Cu(111) substrate, the unit cell is drawn in blue. In a) small crosses (in red, blue and yellow) show the orientation of the (R)- and (S)-petaled mills.

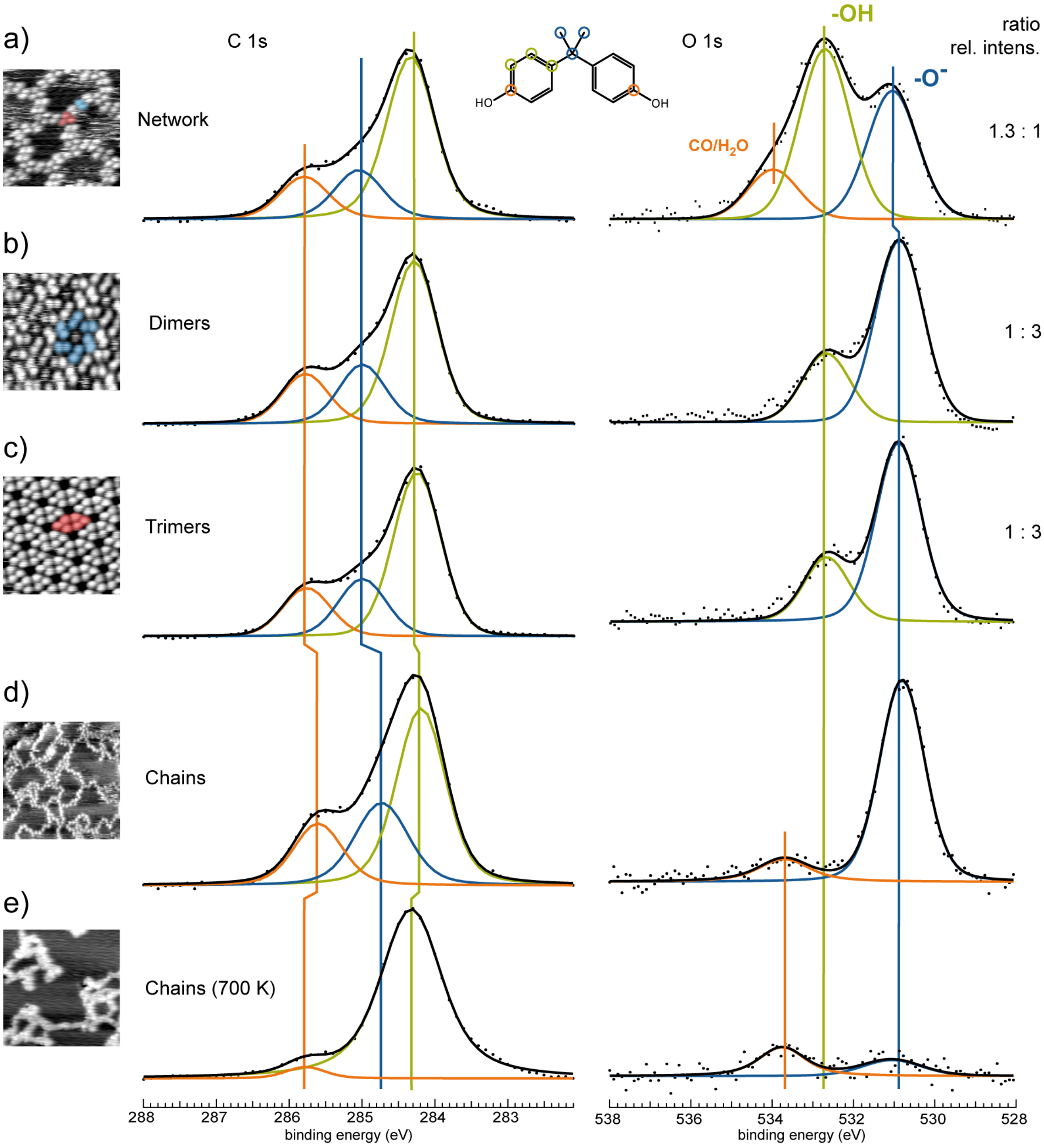

Figure 3.40: Fitted high-resolution X-ray photoelectron spectra of the C 1s (left) and O 1s (right) core level of a) the network-phase, b) dimer-phase c) trimer-phase, d) chain-like phase and e) chain-like phase after annealing to 700 K of a submonolayer BPA adsorbed on the Cu(111) surface. The -OH to -O$^-$ ratios for a-c) are shown on the right.

mensional crystal polymorphs of the same constituents. Considering the higher formation temperature of the trimer-phase, the temperature of ~ 300 K might correspond to the energy that is needed to overcome an activation barrier for the formation of the energetically more stable trimeric arrangement. Another possible explanation would be a local density effect, indicated by the molecular density of the trimer-phase, which is decreased by approximately 25 % with respect to the dimer-phase.

The chains appearing subject to the high temperature (470 K and above) annealing (figure 3.40d, right) no longer retain any protons in the alcohol moieties. The O 1s spectrum after annealing to ~ 520 K, shows only the phenolate contribution at 530.9 eV and a new small signal at 533.8 eV. The latter can not be straight forwardly assigned but based on its binding energy it must originate by oxygen containing moieties decoupled from the metal surface and distinct from phenol/phenolate [169]. It is an evidence of further thermally induced alterations and accordingly its contribution increases with higher temperature annealing. The corresponding carbon signatures in the XP (figure 3.40d, left) and NEXAFS spectra (figure 3.41) are virtually unchanged, supporting that the carbon molecular backbone is mostly intact after this temperature treatment. After annealing to 700 K, the ratio of the O 1s to the C 1s signal decreases by approximately 65 %, indicating significant loss of oxygen and concomitantly the intensity of the signal at 533.8 eV roughly doubles (figure 3.37e). The carbon spectra corroborate remarkable changes in the molecular structure, with loss of the phenolate and methyl signatures. The annealing temperature and the new structure of the chains in the STM images (figure 3.37) points to carbonaceous covalently linked species. For comparison, thermal dissociation of BPA polycarbonate at 730 K results in a variety of aliphatic and aromatic carbon fragments including phenol and substituted phenol moieties [161]. However all of these small fragments would desorb from the surface by the annealing step.

NEXAFS measurements as a function of photon incidence angle (see figure 3.41) indicate an average tilt angle of $30^\circ \pm 10^\circ$ with respect to the copper surface plane for the two phenol moieties. The average tilt angle does not vary as a function of temperature. Similar to the explanation of the NEXAFS spectrum for BPA on Ag(111), contributions from both phenol rings must be taken into account, allowing the tilt angles to range between combinations of 0° and 80° to 30° and 30°.

Modeling:

Combining the information of the STM and the X-ray spectroscopy studies, the following models for the three phases are proposed. The alcohol groups in close proximity to the copper substrate are expected to readily deprotonate at the deposition temperature of 260 K [170, 171]. In the present case, 25-50 % of the phenol groups are still protonated,

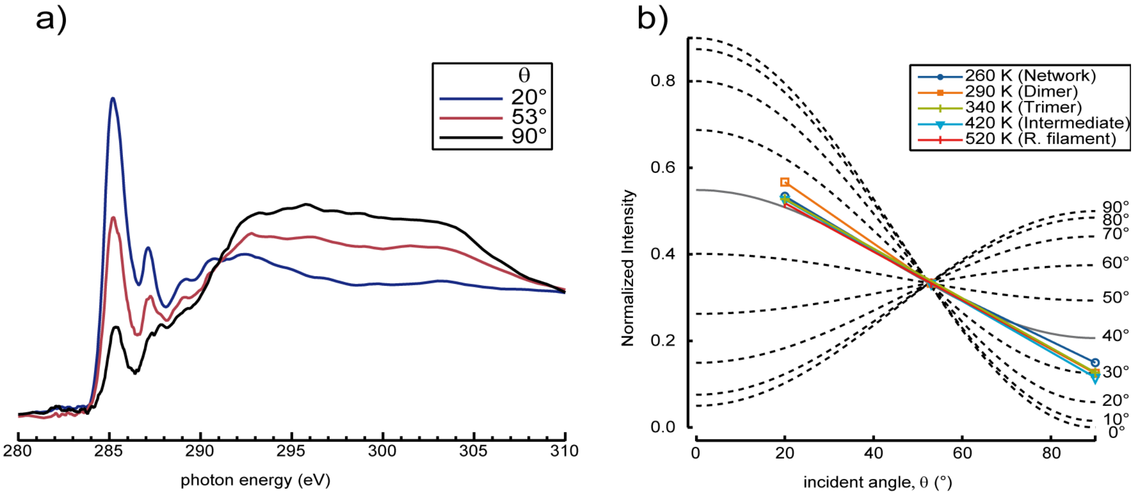

Figure 3.41: a) Normalized experimental C K-edge NEXAFS data at three angles of photon incidence, θ, for the Network phase. b) Curve-fitting analysis of the photon angle dependence of the π^* resonance for 5 different annealing temperatures of the sample.

suggesting that these groups are protected from the metallic surface. Taking the information of the NEXAFS measurements into account, a possible adsorption geometry of the molecule is a configuration with one phenol ring being close to parallel (tilt angle $\sim 15°$) to the surface, which is consistent with tilt angles between 0° and 25° that have been reported for phenol adsorbed on several surfaces such as Cu(110) [168], Pt(111) [172] and Ni(111) [173]. Due to the three dimensional shape of BPA, the other ring points away from the surface with a tilt angle of $\sim 70°$ with respect to the surface (figure 3.31b), similar to the conformation proposed for the dimeric structures on the Ag(111) surface. Phenol adsorbed on Cu(110) [171] forms a dense packed layer of flat lying molecules with an intermolecular distance close to d_2 and d_3, a detail which strengthens the assumption of only one ring of BPA being in close proximity to the surface and therefore governs the surface footprint of the molecule. Based on this molecular conformation, models for all three phases can be proposed in order to match the different assemblies (figure 3.42a-c) based on hydrogen bonding and $\pi - \pi$ stacking. The trimer motif can be build up from three molecules, each rotated by ±120° with respect to the two others. The hydroxy group of the flat lying phenol rings of all BPA molecules are deprotonated due to the contact with the copper surface, allowing intermolecular =CH$\cdots$O$^-$-hydrogen bonding [174] (figure 3.42f). Hydrogen bonds of the C-H$\cdots$O type have been investigated before on protein-protein interactions [175]. The assembly of the dimers can be envisaged via either hydrogen bonding between the flat lying phenolate rings (much alike the trimer motif, figure 3.42d) or via interaction of the π-systems of the upstanding phenol rings

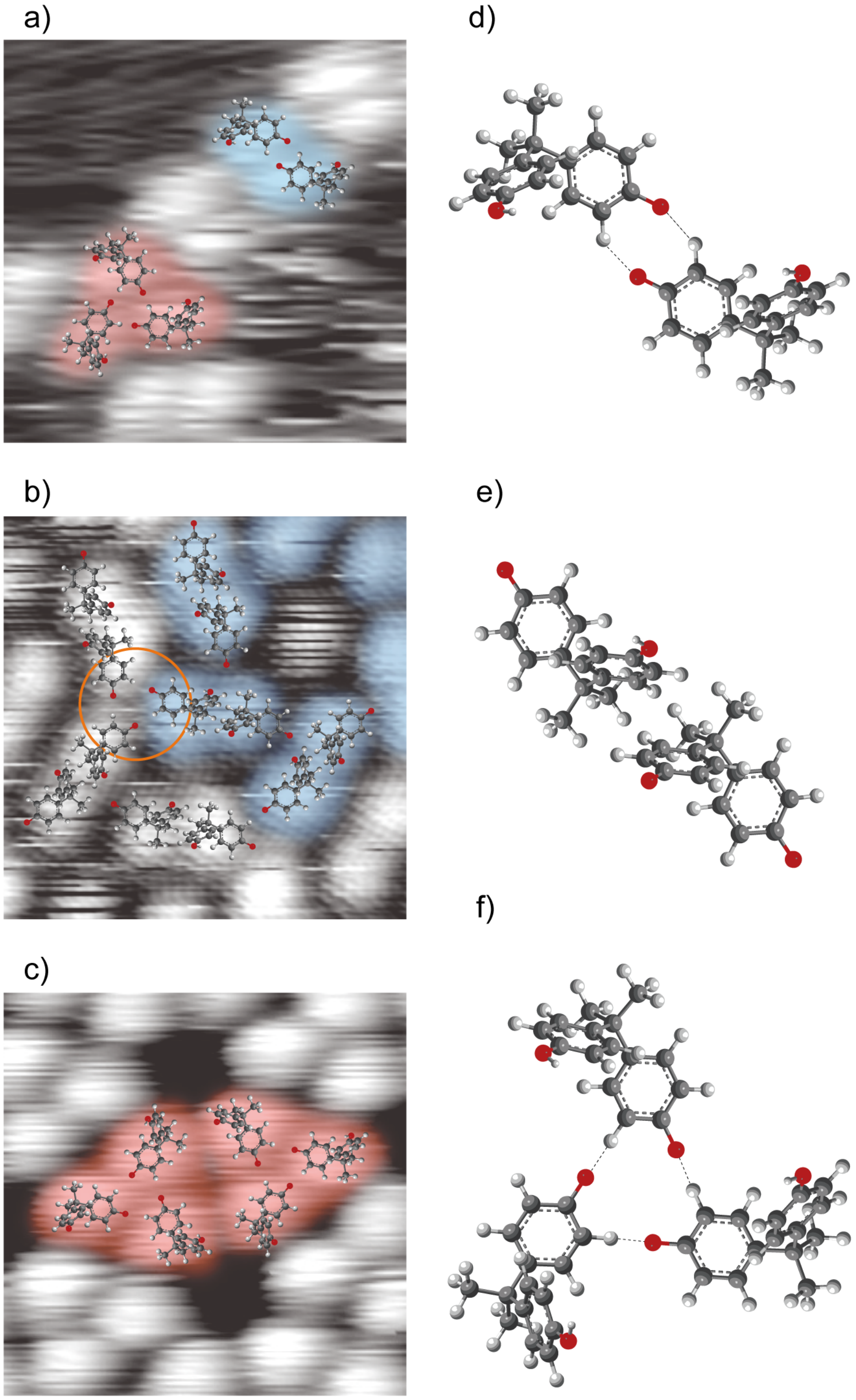

Figure 3.42: Proposed models for BPA structures on Cu(111): a) Network-phase with trimeric and dimeric motifs, b) dimer-phase and c) trimer-phase with molecular models superposed on STM image. d) Adsorption configuration of BPA molecule on the Cu(111) substrate. Models of two dimeric motifs built by d) two $O^{-}\cdots$H-C interactions or e) via $\pi - \pi$ interaction and f) the trimeric motif. The $O^{-}\cdots$H-C bonding is indicated by dotted lines in e) and f).

(figure 3.42e). In the latter case, O-H$\cdots$O$^-$ interaction between the two upstanding hydroxy groups might play an additional role, especially, if one of the hydroxy groups is deprotonated, as it is the case for the dimer-phase. The network-phase consists of trimers and dimers connected via flat lying phenolates. Presumably, the dimers interact, similar to the trimer binding motif, by hydrogen bonding between the flat lying rings which enables a stable dimerization and interaction with neighboring dimers and trimers via their upstanding phenol rings. The assembly of the dimer-phase allows the simultaneous expression of two cooperative interactions, namely O$^-\cdots$H-C hydrogen bonding and $\pi - \pi$ interactions of upstanding phenol-phenolate. The structure can be described as dimers, interacting via the upstanding π-systems with one BPA molecule having two phenolates and the adjacent retaining a phenol moiety in the up-standing ring. The three fold coordination on one side of the dimer motif results in the formation of the trimer motif (highlighted in figure 3.42b). The other side points towards the cavity in the center of the mill, interacting with the next molecule by an additional C-H$\cdots$O$^-$ interaction (figure 3.42b). The close packed assembly of the trimer-phase can be described by the trimer binding motif proposed in figure 3.42f, with the hydroxy groups of all flat lying rings deprotonated and every second upstanding one is protonated. This allows a molecular model in which one out of two neighboring upstanding hydroxy groups is protonated, which might enable interactions similar to a hydrogen bond.

3.5.3 Summary and conclusions:

Summarizing the results, three different molecular arrangements of bisphenol A on Ag(111) and five different phases on Cu(111) depending on the annealing temperature of the molecular overlayer were characterized in this study. On silver, two different arrangements of dimers comprising intact, i.e. fully protonated, molecules were observed in the whole temperature range of 180-340 K. For sample temperatures above 250 K, an additional trimer based structure was reversibly formed on the surface. Six trimers of this structure define a central cavity, in which another, rotating trimer could be observed. XPS measurements revealed a possible change in the local chemical environment for the oxygen atoms indicated by a shift of the O 1s binding energy of -0.5 eV, which was explained with a different adsorption geometry of the BPA molecules. A second peak at lower binding energy was identified as the contribution of a deprotonated hydroxy groups resulting from a surface side reaction. From the combination of these information, it was possible to create a molecular model of all molecular arrangements, with $C_{arom.}$-H$\cdots$OH interactions being the preferred binding motif of dimers and trimers in both adsorption geometries.

The adsorption of BPA on copper exhibits a completely different scenario. The transition between the five different phases characterized on the Cu(111) surface is irreversible. For the network-phase approximately 50 % of the phenol groups are deprotonated. This stepwise deprotonation can be explained by a configuration of the molecule in which part of the phenol groups are protected against deprotonation upon adsorption at 260 K by tilting away from the surface. The phenolate percentage increases to $\sim$ 75% for the dimer-phase and the trimer-phase. Taking into account that the average tilt angle of the two phenols deduced from NEXAFS analysis is 30 ± 10°, models for the three ordered phases can be proposed which are based on a BPA molecule with one phenol ring being nearly parallel to the copper surface and the other one pointing away from the surface. The supramolecular phases are modeled by allowing the formation of hydrogen bonding and π-stacking.

The chemical state with all the phenols tilted towards the surface and exactly half of the upstanding phenols' hydroxy groups being deprotonated, i.e. 75 % of total hydroxy groups, is exhibiting particular stability, as it requires heating to 400 K in order to further deprotonate the BPA molecules. This assumption is strengthened as the deprotonation of BPA does not follow the exponential dependence of the temperature expected from a first order reaction. Chains build up by linked molecular modules are distinguished after heating to 470 K in the STM micrographs whereas the XPS study suggests a complete conversion to phenolate at this temperature. The spectroscopic signatures of the carbon suggest that the BPA component within these chains retains its carbon backbone intact. Further annealing to more than 570 K causes a reshape of the chains towards an ill defined carbonaceous composition.

The weak interaction of BPA with the silver surface allows diffusion of the molecules facilitating different self-assembly scenarios and prevents the molecules from thermal dissociation and deprotonation. The formation of dimers is obviously energetically favored and stabilized by strong intermolecular interactions. In contrary to the scenario on the silver surface, where BPA desorbs at temperatures above 340 K, BPA molecules adsorbed on the Cu(111) substrate show an unusually high temperature surface stability. This surface stability enables the observation of an intriguing series of thermally activated chemical transformations within the molecular layer and hints toward a rich and hard to predict chemistry in biological environments as well. In relation to our initial motivation of the biological role of BPA in DNA alterations, these findings would suggest that a pathway whereupon BPA is preventing access of the methyl-transferase to the relevant DNA/RNA bases should be investigated.

4 Conclusions and Outlook

A systematic multitechnique study of small biologically relevant molecules, namely L- and D-cysteine, uracil, orotic acid and bisphenol A, adsorbed on the close-packed Ag(111) and Cu(111) surfaces was presented in this thesis. The self-assembly of the molecules was structurally resolved by means of STM. Supporting high resolution XPS and angle resolved NEXAFS measurements provided insight into the chemical state of the molecules and their conformation on the surface. At room temperature, uracil, orotic acid and bisphenol A (BPA) adsorb intact on the Ag(111) surface. While STM micrographs of uracil show a single dense packed structure with loose connection to the hexagonal substrate, orotic acid forms two coexisting polymorph structures employing predominantly a dimeric binding motif besides a six-membered ring structure in the so-called "paddle-wheel" structure. The molecular arrangements of BPA on the silver surface show extended polymorphism reflected by three different structures, two employing a dimeric binding motif and a third one, which is reversibly formed for temperatures above 250 K and showing a distinct trimeric arrangement. Generally, the smooth silver surface seems to have a weak influence on the mentioned molecules beyond the two-dimensional confinement, as reflected by the loose connection to the substrate of uracil or the relatively low desorption temperature of BPA at 340 K. Typical functional groups of biomolecules, e.g. hydroxy, carbonyl, carboxy and iminic groups, are chemically unaffected upon room-temperature adsorption. The self-assembly is therefore mainly driven by lateral intermolecular interactions such as hydrogen bonding and features predominantly dimeric and trimeric particularly stable binding motifs.

This is contrasted by the behavior of cysteine, which chemisorbs onto the silver surface by scission of its -S-H bond. Despite the covalent anchoring to the underlying surface, the self-assembly of cysteine is a result of strong zwitterionic hydrogen bonding, the fact that the molecule shows no preferential adsorption site is reflected by a moiré overlayer structure. Upon heat treatment, the ammonium group deprotonates, resulting in an entirely different molecular conformation and superstructure. Uracil, orotic acid and BPA as well are all robustly anchored on the Cu(111) surface. Uracil shows three different periodic adsorption geometries dependent on annealing temperature and surface coverage. Similarly, BPA assembles in five distinct structures as a function of temperature. In both cases the structures could be clearly assigned to different chemical states due to the deprotonation of functional groups and/or adsorption geometries. In contrast, orotic acid exhibits a single periodic structure with a lifetime of minutes, while the protonation grade of the functional groups and the orientation with respect to the surface clearly change with heat treatment and surface coverage. The strong interaction of uracil, BPA and orotic acid with the copper surface as well as the chemisorption of cysteine is crucial for the temperature-induced gradual deprotonation of the different functional groups, allowing to precisely adjust their chemical state by heat treatment. The deprotonation steps are closely linked to completely different molecular arrangements. Interestingly, a high packing density seems to force cysteine as well as orotic acid into an orientation which prevents at least part of the molecules from (immediate) deprotonation, an additional parameter which could be exploited when fine tuning the chemical state of a molecule.

The detailed knowledge of the properties of the systems investigated in this thesis and the precise adjustability of their chemical state facilitates the tailored biofunctionalization of certain metal surfaces. The functionality of larger biologic molecules such as proteins, DNA sequences or even cells depend strongly on their conformation, as described in the introduction. The strong polarization forces of metal substrates, even of noble metals such as silver, might cause denaturation of these systems in contact with the metal. Nevertheless metal surfaces provide well suited substrates for sensor arrays and many other applications. This problem could be overcome by using a spacer layer, which on the one hand interacts strong enough with both the substrate and the biologic entity to immobilize it on the surface but on the other hand prevents it from the influence of the metal substrate [5]. Small biomolecules, such as the ones that were investigated here, could act as such spacer molecules. The knowledge of their self-assembly patterns on substrates and how to tailor their chemical state as well as their interaction with other biomolecules would allow a very precise functionalization of metal substrates with larger biomolecules which can be anchored on the spacer layer.

The adjustability of the chemical state, which reflects the reactivity of a molecule, might also play a role in future applications for catalyzed reactions employing surface modified catalysts. While the chirality of the molecular overlayer and the individual molecules can influence the enantioselectivity of a reaction, the reactivity of the adsorbates might determine the exact reaction products by specifically activating or deactivating certain functional groups.

5 Acknowledgments

First of all, I would like to thank Prof. Johannes Barth for giving me the possibility to work at E20 in this interesting and diversified project and for his great supervision during the whole period of time. Many thanks also to Dr. Joachim Reichert for supervision, many discussions, for guidance and a lot of help, whenever I needed it. I am extremely thankful to Dr. Anthoula Papageorgiou. Anthoula, thanks for spending such a lot of time with me, for discussion, criticism, for laughing together, simply for all your help and friendship!

I would like to thank the whole team of the Aarhus-STM group, Dr. Matthias Marschall for introducing me to this STM, but also to Julian Lloyd, Stephan Saller, Seung Cheol Oh and Dr. Özge Sağlam not only for the good scientific support but also the very pleasant atmosphere in the lab.

Furthermore, I would like to thank the synchrotron team, namely Dr. Florian Klappenberger, Dr. Francesco Allegretti and Katharina Diller for introducing me into the secrets of synchrotron XPS and NEXAFS, making the beamtimes a pleasant and interesting experience and keeping me awake during long nightshifts.

I am very grateful to Dr. Ari P. Seitsonen from Universität of Zürich, who performed the DFT calculations of uracil on Cu(111), which helped a lot to understand the behavior of this molecule on the surface. Also many thanks to Dr. Alexei Nefedov and Prof. Christoph Wöll from Karlsruhe Institute of Technology for access to the HE-SGM beamline at Bessy II.

I am very thankful for the constant support of Viktoria Blaschek, Kamila Wilson, Max Glanz, Karl Eberle, Karl Kölbl and Reinhold Schneider, to whom I could come with every technical or administrational problem and always got promt help.

It is a pleasure to thank the people from my office, Saranyan Vijayaraghavan and Dr. David Écija Fernández for the nice atmosphere, for good discussions and the great time, we had together. A very special and personal thank goes to the E20 ladies and the "lunch connection" and the friends who shared holidays, conference experiences and free time with me. In this regard, I would like to name especially Nenad Kepčija, Sushobhan Joshi, Andreas Kim, Katharina Diller, Anthoula Papageorgiou, Julian Lloyd, Max Glanz, Karl Eberle, Alissa Wiengarten, Tobias Kaposi, Sebastian Jakob and the great Claudia Majer for easy times, constant supplement of chocolate, jokes and good advices.

Of course, I want to thank also everyone else at E20 for making these last years such a great experience!

Finally, I am deeply grateful to my great family. To Wolfgang and Sabine Fischer, my parents, for their love and for helping me to get where I am today, who always believed in me and supported me in everything I did. To Florian Fischer, my brother, for being my very best friend and my grandparents for all their love. And last but not least to Michael Mosch, my boyfriend and the best partner I could think of. Thank you for your love, patience, support and for always encouraging me in my decisions. *Danke, ihr seid die beste Familie, die man sich wünschen kann!*

This work was supported by the ERC Advanced Grant MolArt (no. 247299).

6 List of Publications

[1] Papageorgiou, A. C., Fischer, S., Reichert, J., Diller, K., Kleppenberger, F., Allegretti, F., Seitsonen, A. P. and Barth, J. V. (2012) Chemical transformations drive complex self-assembly of uracil on close-packed coinage metal surfaces. *ACS Nano 6,* 2477-2486.

[2] Fischer, S., Papageorgiou, A. C., Marschall, M., Reichert, J., Diller, K., Klappenberger, F., Allegretti, F., Nefedov, A., Wöll, C. and Barth, J. V. (2012) L-Cysteine on Ag(111): A ombined STM and X-ray spectroscopy study of anchorage and deprotonation. *J. Phys. Chem. C 116,* 20356-20362.

[3] Zhang, Y.-Q., Kepčija, N., Kleinschrodt, M., Diller, K., Fischer, S., Papageorgiou, A. C., Allegretti, F., Björk, J., Klyatskaya, S., Klappenberger, F., Ruben, M. and Barth, J. B. (2012) Homo-coupling of terminal alkynes on a noble metal surface. *Nat. Commun. 3,* 1286-1293.

[4] Bischoff, F., Seufert, K., Auwärter, W., Joshi, S., Vijayaraghavan, S., Écija, D., Diller, K., Papageorgiou, A. C., Fischer, S., Allegretti, F., Duncan, D. A., Klappenberger, F., Blobner, F., Han, R. and Barth, J. V. (2013) How surface bonding and repulsive interactions cause phase transformations: ordering of a prototype macrocyclic compound on Ag(111). *ACS Nano 7,* 3139-3149.

[5] Écija, D., Urgel, J. I., Papageorgiou, A. C., Joshi, S., Auwärter, W., Seitsonen, A. P., Klyatskaya, S., Ruben, M., Fischer, S., Vijayaraghavan, S., Reichert, J. and Barth, J. V. (2013) Five-vertex Archimedean surface tessellation by lanthanide-directed molecular self-assembly *Proc. Natl. Acad. Sci. U. S. A. 110,* 6678-6681.

[6] Diller, K., Klappenberger, F., Allegretti, F., Papageorgiou, A. C., Fischer, S., Wiengarten, A., Joshi, S., Seufert, K., Écija, D., Auwärter, W. and Barth, J. V. (2013) Investigating the molecule-substrate interaction of prototypic tetrapyrrole compounds: Adsorption and self-metalation of porphine on Cu(111) *J. Chem. Phys. 138,* 154710.

[7] Papageorgiou, A. C., Fischer, S., Oh, S. C., Saller, S., Sağlam, Ö., Reichert, J., Wiengarten, A., Seufert, K., Vijayaraghavan, S., Auwärter, W., Allegretti, F., Acres, R. G.,

Prince, K. C., Diller, K., Klappenberger, F. and Barth, J. B. (2013) Self-terminating protocol for an interfacial complexation reaction in vacuo by metal-organic chemical vapor deposition. *ACS Nano 7*, 4520-4526.

[8] Fischer, S., Papageorgiou, A. C., Lloyd, J., Oh, S. C., Diller, K., Allegretti, F., Klappenberger, F., Reichert, J. and Barth, J. V. (2013) Stepwise thermal deprotonation of bisphenol A on Cu(111): A STM and X-ray spectroscopy study. *ACS Nano, submitted.*

Bibliography

[1] Radivojević, M., Rehren, T., Pernicka, E., Šljivar, D., Brauns, M., and Borić, D. (2010) On the origins of extractive metallurgy: new evidence from Europe. *J. Archaeol. Sci. 37*, 2775–2787.

[2] Bick, A. *Die Steinzeit*; Theiss: Stuttgart, 2006.

[3] Henzler, M., and Göpel, W. *Oberflächenphysik des Festkörpers*; B. G. Teubner: Stuttgart, 1991.

[4] Blüchel, K. G. *Bionik*; Wilhelm Goldmann Verlag: München, 2006.

[5] Kasemo, B. (2002) Biological surface science. *Surf. Sci. 500*, 656–677.

[6] Kasemo, B., and Gold, J. (1999) Implant surfaces and interface processes. *Adv. Dent. Res. 13*, 8–20.

[7] Ratner, B. D. (1996) The engineering of biomaterials exhibiting recognition and specificity. *J. Mol. Recognit. 9*, 617–625.

[8] Göpel, W. (1998) Bioelectronics and nanotechnologies. *Biosens. Bioelectron. 13*, 723–728.

[9] Collings, A. F., and Caruso, F. (1997) Biosensors: recent advances. *Rep. Prog. Phys. 60*, 1397–1445.

[10] Wan, Y., Su, Y., Zhu, X., Liu, G., and Fan, C. (2013) Development of electrochemical immunosensors towards point of care diagnostics. *Biosens. Bioelectron. 47*, 1–11.

[11] Nitzan, A., and Ratner, M. A. (2003) Electron transport in molecular wire junctions. *Science 300*, 1384–1389.

[12] Gerster, D., Reichert, J., Bi, H., Barth, J. V., Kaniber, S. M., Holleitner, A. W., Visoly-Fisher, I., Sergani, S., and Carmeli, I. (2012) Photocurrent of a single photosynthetic protein. *Nat. Nanotechnol. 7*, 673–676.

[13] Barlow, S. M., and Raval, R. (2003) Complex organic molecules at metal surfaces: bonding, organisation and chirality. *Surf. Sci. Rep. 50*, 201–341.

[14] Lalander, C. H., Zheng, Y., Dhuey, S., Cabrini, S., and Bach, U. (2010) DNA-directed self-assembly of gold nanoparticles onto nanopatterned surfaces: controlled placement of individual nanoparticles into regular arrays. *ACS Nano 4*, 6153–6161.

[15] Zheng, Y., Lalander, C. H., Thai, T., Dhuey, S., Cabrini, S., and Bach, U. (2011) Gutenberg-style printing of self-assembled nanoparticle arrays: electrostatic nanoparticle immobilization and DNA-mediated transfer. *Angew. Chem., Int. Ed. Engl. 50*, 4398–4402.

[16] Engel, A., Gaub, H. E., and Müller, D. J. (1999) Atomic force microscopy: a forceful way with single molecules. *Curr. Biol. 9*, R133–R136.

[17] Hansma, H. G., Kim, K. J., Laney, D. E., Garcia, R. A., Argaman, M., Allen, M. J., and Parsons, S. M. (1997) Properties of biomolecules measured from atomic force microscope images: a review. *J. Struct. Biol. 119*, 99–108.

[18] Binnig, G., and Rohrer, H. (1982) Scanning tunneling microscopy. *Helv. Phys. Acta 55*, 726–735.

[19] Binnig, G., and Rohrer, H. (1983) Scanning tunneling microscopy. *Surf. Sci. 126*, 236–244.

[20] Binnig, G., and Rohrer, H. (1986) Scanning tunneling microscopy - from birth to adolescence. *Physics* 389–409.

[21] Schneeweiss, M. A., and Kolb, D. M. (2000) Das Rastertunnelmikroskop in der Elektrochemie. *Chem. Unserer Zeit 34*, 72–83.

[22] Kühne, D., Klappenberger, F., Krenner, W., Klyatskaya, S., Ruben, M., and Barth, J. V. (2010) Rotational and constitutional dynamics of caged supramolecules. *Proc. Natl. Acad. Sci. U.S.A. 107*, 21332–21336.

[23] Écija, D., Vijayaraghavan, S., Auwärter, W., Joshi, S., Seufert, K., Aurisicchio, C., Bonifazi, D., and Barth, J. V. (2012) Two-dimensional short-range disordered crystalline networks from flexible molecular modules. *ACS Nano 6*, 4258–4265.

[24] McArthur, S. L. (2006) Applications of XPS in bioengineering. *Surf. Interface Anal. 38*, 1380–1385.

[25] Dolinoy, D. C., Huang, D., and Jirtle, R. L. (2007) Maternal nutrient supplementation counteracts bisphenol A-induced DNA hypomethylation in early development. *Proc. Natl. Acad. Sci. U.S.A. 104*, 13056–13061.

[26] Atkins, P. W. *Physikalische Chemie*; Wiley-VCH: Weinheim, 2001.

[27] Chen, C. J. *Introduction to Scanning Tunneling Microscopy*; Oxford University Press: Oxford, 1993.

[28] Bardeen, J. (1961) Tunnelling from a many-particle point of view. *Phys. Rev. Lett. 6*, 57–59.

[29] Tersoff, J., and Hamann, D. R. (1985) Theory of the scanning tunneling microscope. *Phys. Rev. B 31*, 805–813.

[30] Besenbacher, F., Lægsgaard, E., and Stensgaard, I. (2005) Fast-scanning STM studies. *Mater. Today 8*, 26–30.

[31] Lægsgaard, E., Österlund, L., Thostrup, P., Rasmussen, P. B., Stensgaard, I., and Besenbacher, F. (2001) A high-pressure scanning tunneling microscope. *Rev. Sci. Instrum. 72*, 3537–3542.

[32] Horcas, I., Fernández, R., Gómez-Rodríguez, J. M., Colchero, J., Gómez-Herrero, J., and Baro, A. M. (2007) WSXM: a software for scanning probe microscopy and a tool for nanotechnology. *Rev. Sci. Instrum. 78*, 013705.

[33] Hähner, G. (2006) Near edge X-ray absorption fine structure spectroscopy as a tool to probe electronic and structural properties of thin organic films and liquids. *Chem. Soc. Rev. 35*, 1244–1255.

[34] Feldmann, L., and Mayer, J. *Fundamentals of Surface and Thin Film Analysis*; Elsevier Science Publishing Co., Inc.: New York, 1986.

[35] Hüfner, S. *Photoelectron spectroscopy*; Springer-Verlag: Berlin, 2010.

[36] Banwell, C. E., and McCash, E. In *Molekülspektroskopie*; Kreiner, W. A., Ed.; Oldenburg Wissenschaftsverlag: München, 1999.

[37] Stöhr, J. *NEXAFS spectroscopy*; Springer-Verlag: Berlin, Heidelberg, 1992.

[38] Bearden, J. A., and Burr, A. F. (1967) Reevaluation of X-ray atomic energy levels. *Rev. Mod. Phys. 39*, 125–142.

[39] Fuggle, J. C., and Mårtensson, N. (1980) Core-level binding energies in metals. *J. Electron Spectrosc. Rel. Phenom. 21*, 275–281.

[40] Shirley, D. A. (1972) High-resolution X-ray photoemission spectrum of the valence bands of gold. *Phys. Rev. B 5*, 4709–4714.

[41] Kühnle, A., Linderoth, T. R., Hammer, B., and Besenbacher, F. (2002) Chiral recognition in dimerization of adsorbed cysteine observed by scanning tunnelling microscopy. *Nature 415*, 891–893.

[42] Kühnle, A., Linderoth, T. R., and Besenbacher, F. (2003) Self-assembly of monodispersed, chiral nanoclusters of cysteine on the Au(110)-(1×2) surface. *J. Am. Chem. Soc. 125*, 14680–14681.

[43] Kühnle, A., Linderoth, T. R., and Besenbacher, F. (2006) Enantiospecific adsorption of cysteine at chiral kink sites on Au(110)-(1×2). *J. Am. Chem. Soc. 128*, 1076–1077.

[44] Reichert, J., Schiffrin, A., Auwärter, W., Weber-Bargioni, A., Marschall, M., Dell'Angela, M., Cvetko, D., Bavdek, G., Cossaro, A., Morgante, A., and Barth, J. V. (2010) L-Tyrosine on Ag(111): universality of the amino acid 2D zwitterionic bonding scheme? *ACS Nano 4*, 1218–1226.

[45] Schiffrin, A., Reichert, J., Pennec, Y., Auwärter, W., Weber-Bargioni, A., Marschall, M., Dell'Angela, M., Cvetko, D., Bavdek, G., Cossaro, A., Morgante, A., and Barth, J. V. (2009) Self-assembly of L-methionine on Cu(111): steering chiral organization by substrate reactivity and thermal activation. *J. Phys. Chem. C 113*, 12101–12108.

[46] Schiffrin, A., Riemann, A., Auwärter, W., Pennec, Y., Weber-Bargioni, A., Cvetko, D., Cossaro, A., Morgante, A., and Barth, J. V. (2007) Zwitterionic self-assembly of L-methionine nanogratings on the Ag(111) surface. *Proc. Natl. Acad. Sci. U.S.A. 104*, 5279–5284.

[47] Nyberg, M., Hasselström, J., Karis, O., Wassdahl, N., Weinelt, M., Nilsson, A., and Pettersson, L. G. M. (2000) The electronic structure and surface chemistry of glycine adsorbed on Cu(110). *J. Chem. Phys. 112*, 5420–5427.

[48] Schreiber, F. (2000) Structure and growth of self-assembling monolayers. *Prog. Surf. Sci. 65*, 151–256.

[49] Vallée, A., Humblot, V., and Pradier, C.-M. (2010) Peptide interactions with metal and oxide surfaces. *Acc. Chem. Res. 43*, 1297–1306.

[50] Baas, T., Gamble, L., Hauch, K. D., Castner, D. G., and Sasaki, T. (2002) Characterization of a cysteine-containing peptide tether immobilized onto a gold surface. *Langmuir 18*, 4898–4902.

[51] Chi, Q., Zhang, J., Nielsen, J. U., Friis, E. P., Chorkendorff, I., Canters, G. W., Andersen, J. E. T., and Ulstrup, J. (2000) Molecular monolayers and interfacial electron transfer of *pseudomonas aeruginosa* azurin on Au(111). *J. Am. Chem. Soc. 122*, 4047–4055.

[52] Kühnle, A., Linderoth, T. R., Schunack, M., and Besenbacher, F. (2006) L-Cysteine adsorption structures on Au(111) investigated by scanning tunneling microscopy under ultrahigh vacuum conditions. *Langmuir 22*, 2156–2160.

[53] Cavalleri, O., Gonella, G., Terreni, S., Vignolo, M., Floreano, L., Morgante, A., Canepa, M., and Rolandi, R. (2004) High resolution X-ray photoelectron spectroscopy of L-cysteine self-assembled films. *Phys. Chem. Chem. Phys. 6*, 4042–4046.

[54] Gonella, G., Terreni, S., Cvetko, D., Cossaro, A., Mattera, L., Cavalleri, O., Rolandi, R., Morgante, A., Floreano, L., and Canepa, M. (2005) Ultrahigh vacuum deposition of L-cysteine on Au(110) studied by high-resolution X-ray photoemission: from early stages of adsorption to molecular organization. *J. Phys. Chem. B 109*, 18003–18009.

[55] Uvdal, K., Bodö, P., and Liedberg, B. (1992) L-Cysteine adsorbed on gold and copper: an X-ray photoelectron spectroscopy study. *J. Colloid Interface Sci. 149*, 162–173.

[56] Cossaro, A., Terreni, S., Cavalleri, O., Prato, M., Cvetko, D., Morgante, A., Floreano, L., and Canepa, M. (2006) Electronic and geometric characterization of the L-cysteine paired-row phase on Au(110). *Langmuir 22*, 11193–11198.

[57] Mateo-Martí, E., Rogero, C., Gonzalez, C., Sobrado, J. M., de Andrés, P. L., and Martin-Gago, J. A. (2010) Interplay between fast diffusion and molecular interaction in the formation of self-assembled nanostructures of *S*-cysteine on Au(111). *Langmuir 26*, 4113–4118.

[58] Kühnle, A. (2009) Self-assembly of organic molecules at metal surfaces. *Curr. Opin. Colloid Interface Sci. 14*, 157–168.

[59] Canepa, M., Lavagnino, L., Pasquali, L., Moroni, R., Bisio, F., De Renzi, V., Terreni, S., and Mattera, L. (2009) Growth dynamics of L-cysteine SAMs on single-crystal gold surfaces: a metastable deexcitation spectroscopy study. *J. Phys.: Condens. Matter 21*, 264005.

[60] LeParc, R., Smith, C. I., Cuquerella, M. C., Williams, R. L., Fernig, D. G., Edwards, C., Martin, D. S., and Weightman, P. (2006) Reflection anisotropy spectroscopy study of the adsorption of sulfur-containing amino acids at the Au(110)/electrolyte interface. *Langmuir 22*, 3413–3420.

[61] Nazmutdinov, R. R., Zhang, J., Zinkicheva, T. T., Manyurov, I. R., and Ulstrup, J. (2006) Adsorption and in situ scanning tunneling microscopy of cysteine on Au(111): Structure, energy, and tunneling contrasts. *Langmuir 22*, 7556–7567.

[62] Xu, Q.-M., Wan, L.-J., Wang, C., Bai, C.-L., Wang, Z.-Y., and Nozawa, T. (2001) New structure of L-cysteine self-assembled monolayer on Au(111): studies by in situ scanning tunneling microscopy. *Langmuir 17*, 6203–6206.

[63] Zhang, J., Chi, Q., Nielsen, J. U., Friis, E. P., Andersen, J. E. T., and Ulstrup, J. (2000) Two-dimensional cysteine and cystine cluster networks on Au(111) disclosed by voltammetry and in situ scanning tunneling microscopy. *Langmuir 16*, 7229–7237.

[64] Dakkouri, A. S., Kolb, D. M., Edelstein-Shima, R., and Mandler, D. (1996) Scanning tunneling microscopy study of L-cysteine on Au(111). *Langmuir 12*, 2849–2852.

[65] Santos, E., Avalle, L. B., Scurtu, R., and Jones, H. (2007) L-Cysteine films on Ag(111) investigated by electrochemical and nonlinear optical methods. *Chem. Phys. 342*, 236–244.

[66] Thomsen, L., Wharmby, M. T., Riley, D. P., Held, G., and Gladys, M. J. (2009) The adsorption and stability of sulfur containing amino acids on Cu{531}. *Surf. Sci. 603*, 1253–1261.

[67] Di Felice, R., and Selloni, A. (2004) Adsorption modes of cysteine on Au(111): thiolate, amino-thiolate, disulfide. *J. Chem. Phys. 120*, 4906–4914.

[68] Di Felice, R., Selloni, A., and Molinari, E. (2003) DFT study of cysteine adsorption on Au(111). *J. Phys. Chem. B 107*, 1151–1156.

[69] Luque, N. B., Vélez, P., Pötting, K., and Santos, E. (2012) Ab initio studies of the electronic structure of L-cysteine adsorbed on Ag(111). *Langmuir 28*, 8084–8099.

[70] Dodero, G., De Michieli, L., Cavalleri, O., Rolandi, R., Oliveri, L., Daccà, A., and Parodi, R. (2000) L-Cysteine chemisorption on gold: an XPS and STM study. *Colloids Surf., A 175*, 121–128.

[71] Fischer, S., Papageorgiou, A. C., Marschall, M., Reichert, J., Diller, K., Klappenberger, F., Allegretti, F., Nefedov, A., Wöll, C., and Barth, J. V. (2012) L-Cysteine on Ag(111): a combined STM and X-ray spectroscopy study of anchorage and deprotonation. *J. Phys. Chem. C 116*, 20356–20362.

[72] Fenter, P., Eisenberger, P., Li, J., Camillone III, N., Bernasek, S., Scoles, G., Ramanarayanan, T. A., and Liang, K. S. (1991) Structure of $CH_3(CH_2)_{17}SH$ self-assembled on the Ag(111) surface: an incommensurate monolayer. *Langmuir 7*, 2013–2016.

[73] Xu, Q., Ma, H., Yip, H., and Jen, A. K.-Y. (2008) Controlled assembly of large π-conjugated aromatic thiols on Au(111). *Nanotechnology 19*, 135605.

[74] Sellers, H., Ulman, A., Shnidman, Y., and Eilers, J. E. (1993) Structure and binding of alkanethiolates on gold and silver surfaces: implications for self-assembled monolayers. *J. Am. Chem. Soc. 115*, 9389–9401.

[75] Ataman, E., Isvoranu, C., Knudsen, J., Schulte, K., Andersen, J. N., and Schnadt, J. (2011) Adsorption of L-cysteine on rutile TiO_2(110). *Surf. Sci. 605*, 179–186.

[76] Ataman, E., Isvoranu, C., Andersen, J. N., Schnadt, J., and Schulte, K. (2011) Unconventional zwitterionic state of L-cysteine. *J. Phys. Chem. Lett. 2*, 1677–1681.

[77] Allegretti, F., Polcik, M., and Woodruff, D. P. (2007) Quantitative determination of the local structure of thymine on Cu(110) using scanned-energy mode photoelectron diffraction. *Surf. Sci. 601*, 3611–3622.

[78] Kaznacheyev, K., Osanna, A., Jacobsen, C., Plashkevych, O., Vahtras, O., Ågren, H., Carravetta, V., and Hitchcock, A. P. (2002) Innershell absorption spectroscopy of amino acids. *J. Phys. Chem. A 106*, 3153–3168.

[79] Zubavichus, Y., Shaporenko, A., Grunze, M., and Zharnikov, M. (2005) Innershell absorption spectroscopy of amino acids at all relevant absorption edges. *J. Phys. Chem. A 109*, 6998–7000.

[80] Hasselström, J., Karis, O., Weinelt, M., Wassdahl, N., Nilsson, A., Nyberg, M., Pettersson, L. G. M., Samant, M. G., and Stöhr, J. (1998) The adsorption structure of glycine adsorbed on Cu(110); comparison with formate and acetate/Cu(110). *Surf. Sci. 407*, 221–236.

[81] Shin, T., Kim, K.-N., Lee, C.-W., Shin, S. K., and Kang, H. (2003) Self-assembled monolayer of L-cysteine on Au(111): hydrogen exchange between zwitterionic L-cysteine and physisorbed water. *J. Phys. Chem. B 107*, 11674–11681.

[82] De Renzi, V., Lavagnino, L., Corradini, V., Biagi, R., Canepa, M., and del Pennino, U. (2008) Very low energy vibrational modes as a fingerprint of H-bond network formation : L-cysteine on Au(111). *J. Phys. Chem. C 112*, 14439–14445.

[83] Humblot, V., Méthivier, C., Raval, R., and Pradier, C.-M. (2007) Amino acid and peptides on Cu(110) surfaces: Chemical and structural analyses of L-lysine. *Surf. Sci. 601*, 4189–4194.

[84] Zhao, X., Yan, H., Tu, X., Zhao, R. G., and Yang, W. S. (2003) Spillover-induced chemisorption of amino acid on silver surfaces. *Langmuir 19*, 5542–5545.

[85] Jones, T. E., Baddeley, C. J., Gerbi, A., Savio, L., Rocca, M., and Vattuone, L. (2005) Molecular ordering and adsorbate induced faceting in the Ag{110}-*(S)*-glutamic acid system. *Langmuir 21*, 9468–9475.

[86] Sayago, D. I., Polcik, M., Nisbet, G., Lamont, C. L. A., and Woodruff, D. P. (2005) Local structure determination of a chiral adsorbate: alanine on Cu(110). *Surf. Sci. 590*, 76–87.

[87] Nirenberg, M. W., and Matthaei, J. H. (1961) The dependence of cell-free protein synthesis in E. coli upon naturally occurring or synthetic polyribonucleotides. *Proc. Natl. Acad. Sci. U.S.A. 47*, 1588–1602.

[88] Sowerby, S. J., Cohn, C. A., Heckl, W. M., and Holm, N. G. (2001) Differential adsorption of nucleic acid bases: Relevance to the origin of life. *Proc. Natl. Acad. Sci. U.S.A. 98*, 820–822.

[89] Klappenberger, F., Kühne, D., Krenner, W., Silanes, I., Arnau, A., García de Abajo, F. J., Klyatskaya, S., Ruben, M., and Barth, J. V. (2009) Dichotomous array of chiral quantum corrals by a self-assembled nanoporous kagomé network. *Nano Lett. 9*, 3509–3514.

[90] Schiffrin, A., Reichert, J., Auwärter, W., Jahnz, G., Pennec, Y., Weber-Bargioni, A., Stepanyuk, V. S., Niebergall, L., Bruno, P., and Barth, J. V. (2008) Self-aligning atomic strings in surface-supported biomolecular gratings. *Phys. Rev. B 78*, 035424.

[91] Sowerby, S. J., Holm, N. G., and Petersen, G. B. (2001) Origins of life: a route to nanotechnology. *BioSystems 61*, 69–78.

[92] Mann, S. (2008) Life as a nanoscale phenomenon. *Angew. Chem., Int. Ed. Engl. 47*, 5306–5320.

[93] Chen, Q., and Richardson, N. V. (2003) Enantiomeric interactions between nucleic acid bases and amino acids on solid surfaces. *Nat. Mater. 2*, 324–328.

[94] Gardener, J. A., Shvarova, O. Y., Briggs, G. A. D., and Castell, M. R. (2010) Intricate hydrogen-bonded networks: binary and ternary combinations of uracil, PTCDI, and melamine. *J. Phys. Chem. C 114*, 5859–5866.

[95] Palma, C.-A., Björk, J., Bonini, M., Dyer, M. S., Llanes-Pallas, A., Bonifazi, D., Persson, M., and Samorì, P. (2009) Tailoring bicomponent supramolecular nanoporous networks: phase segregation, polymorphism, and glasses at the solid-liquid interface. *J. Am. Chem. Soc. 131*, 13062–13071.

[96] Llanes-Pallas, A., Matena, M., Jung, T., Prato, M., Stöhr, M., and Bonifazi, D. (2008) Trimodular engineering of linear supramolecular miniatures on Ag(111) surfaces controlled by complementary triple hydrogen bonds. *Angew. Chem., Int. Ed. Engl. 47*, 7726–7730.

[97] Barth, J. V. (2009) Fresh perspectives for surface coordination chemistry. *Surf. Sci. 603*, 1533–1541.

[98] Xu, W., Wang, J.-G., Yu, M., Lægsgaard, E., Stensgaard, I., Linderoth, T. R., Hammer, B., Wang, C., and Besenbacher, F. (2010) Guanine- and potassium-based two-dimensional coordination network self-assembled on Au(111). *J. Am. Chem. Soc. 132*, 15927–15929.

[99] Purohit, C. S., and Verma, S. (2007) Patterned deposition of a mixed-coordination adenine-silver helicate, containing a π-stacked metallacycle, on a graphite surface. *J. Am. Chem. Soc. 129*, 3488–3489.

[100] Sowerby, S. J., and Petersen, G. B. (1997) Scanning tunneling microscopy of uracil monolayers self-assembled at the solid | liquid interface. *J. Electroanal. Chem. 433*, 85–90.

[101] Sowerby, S., Edelwirth, M., and Heckl, W. M. (1998) Molecular mechanics simulation of uracil adlayers on molybdenum disulfide and graphite surfaces. *Appl. Phys. A: Mater. Sci. Process. 66*, S649–S653.

[102] Mamdouh, W., Kelly, R. E. A., Dong, M., Kantorovich, L. N., and Besenbacher, F. (2008) Two-dimensional supramolecular nanopatterns formed by the coadsorption of guanine and uracil at the liquid/solid interface. *J. Am. Chem. Soc. 130*, 695–702.

[103] Nakagawa, T., Tanaka, H., and Kawai, T. (1997) Two-dimensional self-assembly of uracil molecules on Cu(111) surfaces: a low-temperature STM study. *Surf. Sci. 370*, L144–L148.

[104] Lopez, A., Chen, Q., and Richardson, N. V. (2002) Combined STM, HREELS and *ab initio* study of the adsorption of uracil on Si(100)-2×1. *Surf. Interface Anal. 33*, 441–446.

[105] Duncan, D. A., Unterberger, W., Kreikemeyer-Lorenzo, D., and Woodruff, D. P. (2011) Uracil on Cu(110): a quantitative structure determination by energy-scanned photoelectron diffraction. *J. Chem. Phys. 135*, 014704.

[106] Dretschkow, T., and Wandlowski, T. (1998) *In-situ* scanning tunneling microscopy study of uracil on Au(100). *Electrochim. Acta 43*, 2991–3006.

[107] Dretschkow, T., Dakkouri, A. S., and Wandlowski, T. (1997) In-situ scanning tunneling microscopy study of uracil on Au(111) and Au(100). *Langmuir 13*, 2843–2856.

[108] Irrera, S., and de Leeuw, N. H. (2011) A density functional theory study of the adsorption of uracil on the Au(100) surface. *Proc. R. Soc. A 467*, 1959–1969.

[109] Cavallini, M., Aloisi, G., Bracali, M., and Guidelli, R. (1998) An in situ STM investigation of uracil on Ag(111). *J. Electroanal. Chem. 444*, 75–81.

[110] Irrera, S., Roldan, A., Portalone, G., and De Leeuw, N. H. (2013) The role of hydrogen bonding and proton transfer in the formation of uracil networks on the gold(100) surface: a density functional theory approach. *J. Phys. Chem. C 117*, 3949–3957.

[111] Kelly, R. E. A., and Kantorovich, L. N. (2006) Homopairing possibilities of the DNA base thymine and the RNA base uracil: an ab initio density functional theory study. *J. Phys. Chem. B 110*, 2249–2255.

[112] Kelly, R. E. A., and Kantorovich, L. N. (2005) Hexagonal adenine networks constructed from their homopairings. *Surf. Sci. 589*, 139–152.

[113] Haug, A., Schweizer, S., Latteyer, F., Casu, M. B., Peisert, H., Ochsenfeld, C., and Chassé, T. (2008) Thin-film properties of DNA and RNA bases: a combined experimental and theoretical study. *ChemPhysChem 9*, 740–747.

[114] Feyer, V., Plekan, O., Richter, R., Coreno, M., Vall-llosera, G., Prince, K. C., Trofimov, A. B., Zaytseva, I. L., Moskovskaya, T. E., Gromov, E. V., and Schirmer, J.

(2009) Tautomerism in cytosine and uracil: an experimental and theoretical core level spectroscopic study. *J. Phys. Chem. A 113*, 5736–5742.

[115] Chiang, T.-C., Kaindl, G., and Mandel, T. (1986) Layer-resolved shifts of photoemission and Auger spectra from physisorbed rare-gas multilayers. *Phys. Rev. B 33*, 695–711.

[116] Zubavichus, Y., Shaporenko, A., Korolkov, V., Grunze, M., and Zharnikov, M. (2008) X-ray absorption spectroscopy of the nucleotide bases at the carbon, nitrogen, and oxygen K-edges. *J. Phys. Chem. B 112*, 13711–13716.

[117] Feyer, V., Plekan, O., Richter, R., Coreno, M., de Simone, M., Prince, K. C., Trofimov, A. B., Zaytseva, I. L., and Schirmer, J. (2010) Tautomerism in cytosine and uracil: a theoretical and experimental X-ray absorption and resonant Auger study. *J. Phys. Chem. A 114*, 10270–10276.

[118] Otero, R., Schöck, M., Molina, L. M., Lægsgaard, E., Stensgaard, I., Hammer, B., and Besenbacher, F. (2005) Guanine quartet networks stabilized by cooperative hydrogen bonds. *Angew. Chem., Int. Ed. Engl. 44*, 2270–2275.

[119] Yu, M., Wang, J., Mura, M., Meng, Q.-Q., Xu, W., Gersen, H., Lægsgaard, E., Stensgaard, I., Kelly, R. E. A., Kjems, J., Linderoth, T. R., Kantorovich, L. N., and Besenbacher, F. (2011) Homochiral xanthine quintet networks self-assembled on Au(111) surfaces. *ACS Nano 5*, 6651–6660.

[120] Thureau, P., Ancian, B., Viel, S., and Thévand, A. (2006) Determining chemical exchange rates of the uracil labile protons by NMR diffusion experiments. *Chem. Comm.* 200–202.

[121] Kurinovich, M. A., and Lee, J. K. (2000) The acidity of uracil from the gas phase to solution: the coalescence of the N1 and N3 sites and implications for biological glycosylation. *J. Am. Chem. Soc. 122*, 6258–6262.

[122] Lin, N., Dmitriev, A., Weckesser, J., Barth, J. V., and Kern, K. (2002) Real-time single-molecule imaging of the formation and dynamics of coordination compounds. *Angew. Chem., Int. Ed. Engl. 41*, 4779–4783.

[123] Barth, J. V., Weckesser, J., Lin, N., Dmitriev, A., and Kern, K. (2003) Supramolecular architectures and nanostructures at metal surfaces. *Appl. Phys. A: Mater. Sci. Process. 76*, 645–652.

[124] Tait, S. L., Langner, A., Lin, N., Stepanow, S., Rajadurai, C., Ruben, M., and Kern, K. (2007) One-dimensional self-assembled molecular chains on Cu(100): interplay between surface-assisted coordination chemistry and substrate commensurability. *J. Phys. Chem. C 111*, 10982–10987.

[125] Klappenberger, F., Weber-Bargioni, A., Auwärter, W., Marschall, M., Schiffrin, A., and Barth, J. V. (2008) Temperature dependence of conformation, chemical state, and metal-directed assembly of tetrapyridyl-porphyrin on Cu(111). *J. Chem. Phys. 129*, 214702.

[126] Eichberger, M., Marschall, M., Reichert, J., Weber-Bargioni, A., Auwärter, W., Wang, R. L. C., Kreuzer, H. J., Pennec, Y., Schiffrin, A., and Barth, J. V. (2008) Dimerization boosts one-dimensional mobility of conformationally adapted porphyrins on a hexagonal surface atomic lattice. *Nano Lett. 8*, 4608–4613.

[127] Lin, N., Payer, D., Dmitriev, A., Strunskus, T., Wöll, C., Barth, J. V., and Kern, K. (2005) Two-dimensional adatom gas bestowing dynamic heterogeneity on surfaces. *Angew. Chem., Int. Ed. Engl. 44*, 1488–1491.

[128] Chen, Q., and Richardson, N. V. (2003) Surface facetting induced by adsorbates. *Prog. Surf. Sci. 73*, 59–77.

[129] Papageorgiou, A. C., Fischer, S., Reichert, J., Diller, K., Blobner, F., Klappenberger, F., Allegretti, F., Seitsonen, A. P., and Barth, J. V. (2012) Chemical transformations drive complex self-assembly of uracil on close-packed coinage metal surfaces. *ACS Nano 6*, 2477–2486.

[130] McNutt, A., Haq, S., and Raval, R. (2002) High temperature phase of the DNA base thymine on Cu(110): a resonance delocalised bonding system. *Surf. Sci. 502-503*, 185–192.

[131] Kornberg, A., Liebermann, I., and Simms, E. S. (1955) Enzymatic synthesis and properties of 5-phosphoribosylpyrophosphate. *J. Biol. Chem. 215*, 389–402.

[132] Hilal, R., Zaky, Z. M., and Elroby, S. A. K. (2004) Electronic structure of orotic acid I. Geometry, conformational preference and tautomerism. *J. Mol. Struct.: THEOCHEM 685*, 35–42.

[133] Barth, J. V., Weckesser, J., Trimarchi, G., Vladimirova, M., De Vita, A., Cai, C., Brune, H., Günter, P., and Kern, K. (2002) Stereochemical effects in supramolecular self-assembly at surfaces: 1-D versus 2-D enantiomorphic ordering for PVBA and PEBA on Ag(111). *J. Am. Chem. Soc. 124*, 7991–8000.

[134] Limbach, H.-H., and Manz, J. (1998) Hydrogen transfer: Experiment and theory. *Ber. Bunsen-Ges. 102*, 289–291.

[135] Sarikaya, M., Tamerler, C., Jen, A. K.-Y., Schulten, K., and Baneyx, F. (2003) Molecular biomimetics: nanotechnology through biology. *Nat. Mater. 2*, 577–585.

[136] Preuss, M., Schmidt, W., and Bechstedt, F. (2005) Coulombic amino group-metal bonding: adsorption of adenine on Cu(110). *Phys. Rev. Lett. 94*, 236102.

[137] Lambert, J.-F. (2008) Adsorption and polymerization of amino acids on mineral surfaces: a review. *Origins Life Evol. Biopheres 38*, 211–242.

[138] Mertig, M., Colombi Ciacchi, L., Seidel, R., Pompe, W., and De Vita, A. (2002) DNA as a selective metallization template. *Nano Lett. 2*, 841–844.

[139] Ferretti, S., Paynter, S., Russell, D. A., Sapsford, K. E., and Richardson, D. J. (2000) Self-assembled monolayers: a versatile tool for the formulation of bio-surfaces. *TrAC, Trends Anal. Chem. 19*, 530–540.

[140] Xiao, S.-J., Brunner, S., and Wieland, M. (2004) Reactions of surface amines with heterobifunctional cross-linkers bearing both succinimidyl ester and maleimide for grafting biomolecules. *J. Phys. Chem. B 108*, 16508–16517.

[141] Smith, E. A., Wanat, M. J., Cheng, Y., Barreira, S. V. P., Frutos, A. G., and Corn, R. M. (2001) Formation, spectroscopic characterization, and application of sulfhydryl-terminated alkanethiol monolayers for the chemical attachment of DNA onto gold surfaces. *Langmuir 17*, 2502–2507.

[142] Chen, Q., Frankel, D. J., and Richardson, N. V. (2002) Chemisorption induced chirality: glycine on Cu{110}. *Surf. Sci. 497*, 37–46.

[143] Barlow, S. M., Louafi, S., Le Roux, D., Williams, J., Muryn, C., Haq, S., and Raval, R. (2004) Supramolecular assembly of strongly chemisorbed size- and shape-defined chiral clusters: S- and R-alanine on Cu(110). *Langmuir 20*, 7171–7176.

[144] Furukawa, M., Tanaka, H., and Kawai, T. (2001) The role of dimer formation in the self-assemblies of DNA base molecules on Cu(111) surfaces: A scanning tunneling microscope study. *J. Chem. Phys. 115*, 3419–3423.

[145] Löwdin, P.-O. (1963) Proton tunneling in DNA and its biological implications. *Rev. Mod. Phys. 35*, 724–732.

[146] Elroby, S. A. K. (2007) Electronic structure of orotic acid II: Acidity, basicity, and interaction with water. *J. Mol. Struct.: THEOCHEM 803*, 67–72.

[147] Tierney, H. L., Murphy, C. J., Jewell, A. D., Baber, A. E., Iski, E. V., Khodaverdian, H. Y., McGuire, A. F., Klebanov, N., and Sykes, E. C. H. (2011) Experimental demonstration of a single-molecule electric motor. *Nat. Nanotechnol. 6*, 625–629.

[148] Stepanow, S., Strunskus, T., Lingenfelder, M., Dmitriev, A., Spillmann, H., Lin, N., Barth, J. V., Wöll, C., and Kern, K. (2004) Deprotonation-driven phase transformations in terephthalic acid self-assembly on Cu(100). *J. Phys. Chem. B 108*, 19392–19397.

[149] Dmitriev, A., Lin, N., Weckesser, J., Barth, J. V., and Kern, K. (2002) Supramolecular assemblies of trimesic acid on a Cu(100) surface. *J. Phys. Chem. B 106*, 6907–6912.

[150] Perry, C. C., Haq, S., Frederick, B. G., and Richardson, N. V. (1998) Face specificity and the role of metal adatoms in molecular reorientation at surfaces. *Surf. Sci. 409*, 512–520.

[151] Kessler, J., and Thieme, F. (1977) Chemisorption of CO on differently prepared Cu(111) surfaces. *Surf. Sci. 67*, 405–415.

[152] Hinch, B. J., and Dubois, L. H. (1992) Stable and metastable phases of water adsorbed on Cu(111). *J. Chem. Phys. 96*, 3262–3268.

[153] Meeker, J. D., Ehrlich, S., Toth, T. L., Wright, D. L., Calafat, A. M., Trisini, A. T., Ye, X., and Hauser, R. (2010) Semen quality and sperm DNA damage in relation to urinary bisphenol A among men from an infertility clinic. *Reprod. Toxicol. 30*, 532–539.

[154] Tharp, A. P., Maffini, M. V., Hunt, P. A., VandeVoort, C. A., Sonnenschein, C., and Soto, A. M. (2012) Bisphenol A alters the development of the rhesus monkey mammary gland. *Proc. Natl. Acad. Sci. U.S.A. 109*, 8190–8195.

[155] Bromer, J. G., Zhou, Y., Taylor, M. B., Doherty, L., and Taylor, H. S. (2010) Bisphenol-A exposure *in utero* leads to epigenetic alterations in the developmental programming of uterine estrogen response. *FASEB J. 24*, 2273–2280.

[156] Irvin, J. A., Neef, C. J., Kane, K. M., Cassidy, P. E., Tullos, G., and St. Clair, A. K. (1992) Polyethers derived from bisphenols and highly fluorinated aromatics. *J. Polym. Sci., Part A: Polym. Chem. 30*, 1675–1679.

[157] Uyama, H., Maruichi, N., Tonami, H., and Kobayashi, S. (2002) Peroxidase-catalyzed oxidative polymerization of bisphenols. *Biomacromolecules 3*, 187–193.

[158] Muir, B. W., McArthur, S. L., Thissen, H., Simon, G. P., Griesser, H. J., and Castner, D. G. (2006) Effects of oxygen plasma treatment on the surface of bisphenol A polycarbonate: a study using SIMS, principal component analysis, ellipsometry, XPS and AFM nanoindentation. *Surf. Interface Anal. 38*, 1186–1197.

[159] Mercier, J. P., Aklonis, J. J., Litt, M., and Tobolsky, A. V. (1965) Viscoelastic behavior of the polycarbonate of bisphenol A. *J. Appl. Polym. Sci. 9*, 447–459.

[160] Rivaton, A. (1995) Recent advances in bisphenol-A polycarbonate photodegradation. *Polym. Degrad. Stabil. 49*, 163–179.

[161] McNeill, I. C., and Rincon, A. (1991) Degradation studies of some polyesters and polycarbonates-8. Bisphenol A polycarbonate. *Polym. Degrad. Stabil. 31*, 163–180.

[162] Lee, J., Ryu, S., and Kim, S. K. (2001) The adsorption and photochemistry of phenol on Ag(111). *Surf. Sci. 481*, 163–171.

[163] Solomon, J. L., Madix, R. J., and Stöhr, J. (1991) Orientation and absolute coverage of benzene, aniline, and phenol on Ag(110) determined by NEXAFS and XPS. *Surf. Sci. 255*, 12–30.

[164] Tait, S. L., Wang, Y., Costantini, G., Lin, N., Baraldi, A., Esch, F., Petaccia, L., Lizzit, S., and Kern, K. (2008) Metal-organic coordination interactions in Fe-terephthalic acid networks on Cu(100). *J. Am. Chem. Soc. 130*, 2108–2113.

[165] del Olmo, M., Zafra, A., Gonzalez-Casado, A., and Vilchez, J. L. (1998) The use of beta-cyclodextrin inclusion complexes for the analysis of bisphenol A residues in water by spectrofluorimetry. *Intern. J. Environ. Anal. Chem. 69*, 99–110.

[166] Norton, P. R., Tapping, R. L., and Goodale, J. W. (1978) High resolution photoemission study of the physisorption and chemisorption of CO on copper and gold. *Surf. Sci. 72*, 33–44.

[167] Spitzer, A., and Lüth, H. (1985) An XPS study of the water adsorption on Cu(110). *Surf. Sci. 160*, 353–361.

[168] Richardson, N. V., and Hofmann, P. (1983) A spectroscopic investigation of the adsorption of phenol on Cu{110}. *Vacuum 33*, 793–796.

[169] Beamson, G., and Briggs, D. *High Resolution XPS of Organic Polymers: The Scienta ESCA300 Database*; Wiley: New York, 1992.

[170] Bowker, M., and Madix, R. J. (1982) XPS, UPS and thermal desorption studies of alcohol adsorption on Cu(110). *Surf. Sci. 116*, 549–572.

[171] Guo, X.-C., and Madix, R. J. (1995) Monolayer structure of phenoxy species on Cu(110): an STM study. *Surf. Sci. 341*, L1065–L1071.

[172] Ihm, H., and White, J. M. (2000) Stepwise dissociation of thermally activated phenol on Pt(111). *J. Phys. Chem. B 104*, 6202–6211.

[173] Myers, A. K., and Benziger, J. B. (1989) Effect of substituent groups on the interaction of benzene with Ni(111). *Langmuir 5*, 1270–1288.

[174] Arunan, E., Desiraju, G. R., Klein, R. A., Sadlej, J., Scheiner, S., Alkorta, I., Clary, D. C., Carbtree, R. H., Dannenberg, J. J., Hobza, P., Kjaergaard, H. G., Legon, A. C., Mennucci, B., and Nesbitt, D. J. (2011) Definition of the hydrogen bond (IUPAC Recommendations 2011). *Pure Appl. Chem. 83*, 1637–1641.

[175] Jiang, L., and Lai, L. (2002) CH$\cdots$O hydrogen bonds at protein-protein interfaces. *J. Biol. Chem. 277*, 37732–37740.